ABSTRACT

Title of Document: BENZOCYCLOBUTENE-BASED ELECTRIC MICROMACHINES SUPPORTED ON MICROBALL BEARINGS: DESIGN, FABRICATION, AND CHARACTERIZATION

Alireza Modafe, Ph.D., 2007

Directed By: Professor Reza Ghodssi, Department of Electrical and Computer Engineering

This dissertation summarizes the research activities that led to the development of the first microball-bearing-supported linear electrostatic micromotor with benzocyclobutene (BCB) low-k polymer insulating layers. The primary application of this device is long-range, high-speed linear micropositioning. The future generations of this device include rotary electrostatic micromotors and microgenerators.

The development of the first generation of microball-bearing-supported micromachines, including device theory, design, and modeling, material characterization, process development, device fabrication, and device test and characterization is presented. The first generation of these devices is based on a 6-phase, bottom-drive, linear, variable-capacitance micromotor (B-LVCM). The design of the electrical and mechanical components of the micromotor, lumped-circuit modeling of the device and electromechanical characteristics, including variable capacitance, force, power, and speed are presented. Electrical characterization of

BCB polymers, characterization of BCB chemical mechanical planarization (CMP), development of embedded BCB in silicon (EBiS) process, and integration of device components using microfabrication techniques are also presented.

The micromotor consists of a silicon stator, a silicon slider, and four stainless-steel microballs. The aligning force profile of the micromotor was extracted from simulated and measured capacitances of all phases. An average total aligning force of 0.27 mN with a maximum of 0.41 mN, assuming a 100 V peak-to-peak square-wave voltage, was measured. The operation of the micromotor was verified by applying square-wave voltages and characterizing the slider motion. An average slider speed of 7.32 mm/s when excited by a 40 Hz, 120 V square-wave voltage was reached without losing the synchronization.

This research has a pivotal impact in the field of power microelectromechanical systems (MEMS). It establishes the foundation for the development of more reliable, efficient electrostatic micromachines with variety of applications such as micropropulsion, high-speed micropumping, microfluid delivery, and microsystem power generation.

BENZOCYCLOBUTENE-BASED ELECTRIC MICROMACHINES SUPPORTED ON MICROBALL BEARINGS: DESIGN, FABRICATION, AND CHARACTERIZATION

By

Alireza Modafe

Dissertation submitted to the Faculty of the Graduate School of the
University of Maryland, College Park, in partial fulfillment
of the requirements for the degree of
Doctor of Philosophy
2007

Advisory Committee:
Professor Reza Ghodssi, Chair
Professor Isaak D. Mayergoyz
Professor Agis A. Iliadis
Professor Gary Rubloff
Professor Amr Baz

© Copyright by
Alireza Modafe
2007

Dedication

To *Roya*, my beloved wife, partner, and friend

for her encouragement, patience, sacrifice, and unconditional love,

to *my parents*

who devoted the best of their lives to my success and my dreams,

and

to *Ryan*, my little son, my hope, and my future.

Acknowledgements

In the course of my study at the University of Maryland (UMD) I had the chance to get to know many wonderful people. Without their help, advice, or dedication, this dissertation would have not been created.

First and foremost, I sincerely thank my advisor Professor Reza Ghodssi for giving me the opportunity to be part of an exciting research project at the MEMS Sensors and Actuators Lab (MSAL). I especially want to thank Professor Ghodssi for his guidance and continuous support even before I met him, and for his understanding, patience, and tolerance during the difficult times that I have been through.

I also want to thank the committee members of my dissertation defense, Professor Isaak Mayergoyz, Professor Agis Iliadis, Professor Gary Rubloff, and Professor Amr Baz. I enjoyed their challenging questions and great discussions.

My special thanks go to my friend and co-worker, Dr. Nima Ghalichechian for his invaluable help in many aspects of this research and taking it to the next level. Mr. David Lin established some of the infrastructures of this project in his work on dynamic characterization of microball bearings and I thank him for introducing me to the fundamentals of microball bearings. Mr. Benjamin Kleber, Mr. Alex Frey, Mr. Borna Ghavam, and Mr. Robert Hergert did their undergraduate research projects at MSAL and contributed quite a bit to this project. I am also grateful to Professor Xiaobo Tan from Michigan State University for his work on characterization and modeling of microball bearings during his post doctoral research at UMD. He expanded the research activities of this project and created a great opportunity for me

to get involved in collaborative research. Professor Jeffrey H. Lang from Massachusetts Institute of Technology (MIT) was kind enough to help me with ideas on variable-capacitance motors. I am especially grateful to Mr. Thomas. C. Loughran and Mr. Alexander Ballew from UMD clean room facilities for training me on clean room procedures and equipment and helping me with device fabrication. I also thank the funding organizations and agencies, National Science Foundation (NSF), Army Research Lab (ARL), and Small Smart Systems Center (SSSC). Without their financial and logistical support, this work would have never made this far.

I want to close the acknowledgments with expressing my deepest gratitude to the most special person in my life. My wife, Roya has been the greatest inspiration and motivation for me. Without her encouragement, patience, and sacrifice, none of this would have been possible. I thank her from bottom of my heart.

Table of Contents

Dedication ii
Acknowledgements iii
Table of Contents v
List of Tables vii
List of Figures ix
Chapter 1: Introduction and Background 1
1.1. Motivation and Objectives 2
1.2. Electric Micromachines 4
1.2.1. Electrostatic vs. Magnetic Micromachines 4
1.2.2. Review of Previous Research on Electrostatic Micromachines 9
1.3. Dielectric Films in Microelectromechanical Systems 14
1.3.1. Review of Dielectric Films for Electrostatic Micromachines 14
1.3.2. Spin-on Low-Dielectric-Constant Benzocyclobutene Polymers 19
1.4. Bearing Mechanisms in Micromachines 23
1.5. Dissertation Overview 24
1.6. Contributions 26
Chapter 2: Device Design and Modeling 27
2.1. Variable-Capacitance Machines in Motor Mode 28
2.1.1. Principle of Operation 28
2.1.2. Energy Conversion Cycle 32
2.2. Variable-Capacitance Machines in Generator Mode 38
2.2.1. Principle of Operation 38
2.2.2. Energy Conversion Cycle 39
2.3. Electromechanical Characteristics of Variable-Capacitance Machines 42
2.3.1. Force and Power 44
2.3.2. Mechanical Speed and Synchronous Operation 46
2.4. Electromechanical Modeling using Lumped-Circuit Elements 49
2.5. Polyphase Variable-Capacitance Motors 56
2.5.1. Single-Phase vs. Polyphase 56
2.5.2. Three-Phase vs. Six-Phase 57
2.6. Microball Bearing Technology in Silicon 59
2.7. A Six-Phase Bottom-Drive Linear Variable-Capacitance Micromotor 64
Chapter 3: Material Characterization, Process Development, and Device Fabrication 70
3.1. Electrical Characterization of Benzocyclobutene Polymers 71
3.1.1. Test Structures 74
3.1.2. Environmental Test Setup 80
3.1.3. Measurement of Dielectric Constant 82
3.1.4. Measurement of Current-Voltage Characteristics 98

3.2. Chemical Mechanical Planarization of Benzocyclobutene Polymers 105
3.2.1. Principles of Chemical Mechanical Characterization 105
3.2.2. Characterization of Chemical Mechanical Planarization 109
3.3. Overview of Fabrication Process 116
3.4. Embedded Benzocyclobutene in Silicon Process 116
3.4.1. EBiS Fabrication Process 119
3.4.2. Process Development and Characterization 125
3.5. Fabrication of Microball Bearings 127
3.5.1. Fabrication of Linear Microball Bearings 128
3.5.2. Fabrication of Rotary Microball Bearings 130
3.6. Stator Fabrication 131
3.7. Slider Fabrication 137
Chapter 4: Device Test and Characterization 140
4.1. Static Measurements: Capacitance and Force 141
4.2. Dynamic Measurements: Position and Speed 145
Chapter 5: Conclusion and Future Work 151
5.1. Summary of the Research Activities 151
5.2. Contributions 152
5.3. Future Work 153
Bibliography 155

List of Tables

Chapter 1

Table 1.1. Types of electrostatic machines

Table 1.2. Viscosity and Film Thickness of Different Lines of Cyclotene

Table 1.3. Processing Features of Cyclotene

Table 1.4. Physical Properties of BCB Polymer and Silicon Dioxide (at 25 °C unless otherwise noted)

Chapter 2

Table 2.1. Parameters Values of the VCM modeled with State Equations (2.51) to (2.54) with the solution shown in Figure 2.12

Table 2.2. Specifications of the Microball used in our application based on American Ball Manufacturing Association (AMBA) standard

Table 2.3. Three different designs of the B-LVCM

Table 2.4. Estimated force and speed of the B-LVCM

Chapter 3

Table 3.1. Physical Properties of Pyrex 7740 (at 25 °C unless otherwise noted)

Table 3.2. CMP Control and Output Parameters

Table 3.3. Specifications of CMP Slurries

Table 3.4. CMP Recipes

Table 3.5. Specifications of Soft-cured BCB Film before and after CMP with MSW2000A Slurry and Recipes I and II

Table 3.6. CMP of BCB Polymer Cured at Different Temperatures using ILD1300 Slurry and Recipe I

Table 3.7. Photolithography Levels for Fabrication of the Stator and the Slider

Table 3.8. Unit processes used in fabrication of the B-LVCM

Chapter 4

Table 4.1. Estimated and measured average speed for device $D2_{SHORT}$

List of Figures

Chapter 1

Figure 1.1. Breakdown voltage and electric field in air at atmospheric pressure as predicted by Paschen's Law.

Figure 1.2. The limit of energy density in electrostatic and magnetic machines vs. air gap size.

Figure 1.3. Schematic cross-section (left) and optical micrograph (right) of the first electrostatic micromotor developed at UC Berkeley. A human hair is shown next to the micromotor on the optical micrograph for comparison [61].

Figure 1.4. Cross-section view of the stator in a typical polyphase electric micromachine showing the dielectric insulating layers and the associated parasitic elements. (Dimensions are not to scale.)

Figure 1.5. Simulation of the minimum capacitance per electrode vs. the insulating layer thickness in a six-phase variable-capacitance micromachine: (a) Problem definition and simulation model, and (b) data for. silicon dioxide and BCB.

Figure 1.6. Chemical structures of (a) BCB and (b) DVS-bis-BCB monomers.

Chapter 2

Figure 2.1. Principle of operation of a simple variable-capacitance motor (VCM). T_A and T_N are aligning and normal torques, respectively. Note that at the moment shown in the figure the stator blades are being excited.

Figure 2.2. The triangle **ABC** is the characteristic space and the path **ABCA** is the no-load energy conversion cycle of a typical VCM. The square-wave excitation voltage and an approximation of the variable capacitance, which are in-phase during the no-load operation, are also shown.

Figure 2.3. The triangle **ABC** is the characteristic space of a typical VCM. The path **ADBEA** is the energy conversion cycle of the VCM when under load. The square-wave excitation voltage and a linear approximation of the variable capacitance, which are out of phase during the load operation, are also shown.

Figure 2.4. The triangle **ABC** is the characteristic space and the path **ABCA** is the no-load energy conversion cycle of a typical charge-controlled VCG. The output voltage and an approximation of the variable capacitance, which are in-phase during the no-load operation, are also shown.

Figure 2.5. The triangle **ABC** is the characteristic space of a typical VCG. The path **ADBEA** is the energy conversion cycle of the VCG when under load. The square-wave output voltage and a linear approximation of the variable capacitance, which are out of phase during the load operation, are also shown.

Figure 2.6. Multiport variable capacitor as an energy conversion element between electrical and mechanical energy domains. The capacitor translates electrical entities (voltage and current) to mechanical entities (force and velocity) generally in three independent directions, and vice versa. The conversion function can be energy (W_t) or co-energy (W_t^*) depending on the mode of operation (charge control or voltage control). Note that a "dot" represents the time derivative.

Figure 2.7. The average power of a VCM as a function of the power angle.

Figure 2.8. Instantaneous and average power of a VCM. In (a) the voltage leads the capacitance ($0 < \delta < \pi/2$) and the average power is negative. The net operation of the VCM is in motor mode. In (b) the voltage lags the capacitance ($\pi/2 < \delta < \pi$) and the average power is positive. The net operation of the VCM is in generator mode.

Figure 2.9. Cross section of an active pole/electrode pair in a VCM showing the lumped-circuit elements associated with the components of the device. C_M is a variable capacitor formed between the rotor pole and the stator active electrode. All other elements are parasitic capacitances and resistances.

Figure 2.10. An electromechanical model for a six-phase linear VCM. The multiport variable capacitor translates voltage/current of the phases in the electrical energy domain to force/velocity of in x, y, and z directions in the mechanical energy domain. The elements in the electrical energy domain are those shown in Figure 2.9. In the mechanical energy domain, M_R is

the rotor mass, and k_R and k_B are the spring constants of the rotor substrate and the bearings, respectively. F_f is the friction force applied to the rotor and is a function of the normal force (F_Z) and the mass of the rotor.

Figure 2.11. A simplified electromechanical model for a single-phase, single-pole VCM.

Figure 2.12. Step response of a VCM for rotor position, velocity, and force.

Figure 2.13. An equivalent circuit for a six-phase VCM. If phases D, E, and F are complementary to phases A, B, and C, every point on the rotor ground plane will be at zero potential due to the symmetry.

Figure 2.14. Schematic cross-section view of three different designs for linear microball bearings: (a) v-groove design, (b) anisotropically-etched trench design, and isotropically-etched trench design. The v-grooves has a sidewall angle of 54.735°, which is the angle between (100) and (111) crystallographic planes in silicon achieved by anisotropic wet etching. The dimensions are designed to have a 10 μm air gap. The contact points are shown with red arrows. The dimensions are to scale.

Figure 2.15. Cross-section view of v-groove microball bearings showing geometrical design parameters

Figure 2.16. Schematic 3D view of linear microball bearings with two parallel v-grooves on stator and slider.

Figure 2.17. Schematic top view of two designs for linear microball bearings: (a) continuous trench and (b) split trench.

Figure 2.18. Schematic 3D view of rotary microball bearings circular v-grooves or trenches on stator and slider.

Figure 2.19. (a) Schematic 3D view of the 6-phase, bottom-drive, linear, variable-capacitance micromotor (B-LVCM), and (b) principle of operation and square-wave excitation.

Figure 2.20. A schematic top view of the B-LVCM stator. Dimensions are to scale based on device $D2_{SHORT}$ design.

Figure 2.21. A schematic top view of the B-LVCM slider. Dimensions are to scale based on device $D2_{SHORT}$ design.

Chapter 3

Figure 3.1. Schematic views of an IDC test structure, (a) top view and (b) cross-section view. Dimensions are not to scale.

Figure 3.2. Process flow for fabrication of IDC test structures showing at what steps capacitance and current-voltage tests are performed.

Figure 3.3. Optical micrographs of fabricated IDCs with (a), (b) 2-μm finger width/spacing, and (c) 3-μm finger width/spacing.

Figure 3.4. The custom-made humidity-stress setup.

Figure 3.5. (a) The electrical test setup and (b) the electrical test chamber.

Figure 3.6. Block diagram of the electrical test setup.

Figure 3.7. Schematic cross section of an IDC showing the dielectric layers, fingers, and boundary conditions. The electric potential between two adjacent fingers is assumed to be 1 V. Due to the symmetric structure of an ideal

IDC, the solution is a periodic function with the period of *p*, therefore, the Laplace Equation is solved analytically and numerically in the shaded area. (*W*: finger width, *p*: finger pitch).

Figure 3.8. Two-dimensional (2D) finite-element numerical simulation of the capacitance vs. pitch in a 500-finger IDC with 1-mm long fingers, showing the effect of BCB top layer thickness. The simulation is performed based on the IDC design of Figure 2.1 and boundary conditions of Figure 2.7. The blue graph represents the (almost) ideal case assuming a very thick (100 μm) BCB layer on top and the red graph is for the IDC design assuming 9.5 μm of BCB and 90.5 μm of air on top. As the graphs show, the capacitance of the 8-μm pitch IDC deviates from the ideal case by only 0.02 % while as the pitch increases beyond the BCB top layer thickness, the deviation blows up drastically. Note that the increase in capacitance at smaller pitches is due to the non-zero finger thickness (0.004 μm in this simulation).

Figure 3.9. Capacitance measurement on several IDCs with different pitch sizes before (0 μm) and after (3.3 μm, 4.2 μm, 7.1 μm) deposition of the second BCB layer: (a) 1-mm long fingers and (b) 10-mm long fingers. The capacitance becomes independent of the BCB thickness as the thickness increases beyond the pitch.

Figure 3.10. Estimation for the capacitance of 500-finger IDCs based on the FEA simulation of a single pitch. For IDCs with very thin fingers the capacitance is almost independent of the IDC pitch and finger width as

far as the ratio remains constant. As the thickness increases, the capacitance of large-pitch IDCs is less sensitive. The finger length was 1 mm in this simulation.

Figure 3.11. Schematic cross section of an IDC with thick fingers.

Figure 3.12. 2-dimensional finite-element numerical simulation of the extracted dielectric constant vs. pitch in a 500-finger IDC with 1-mm long fingers, showing the effect of BCB top layer finite thickness. The finger thickness was assumed to be 0.004 μm in this simulation. Both uncompensated and compensated data has been plotted to show the effect of finger thickness.

Figure 3.13. 2-dimensional finite-element numerical simulation of the extracted dielectric constant vs. pitch in a 500-finger IDC with 1-mm long fingers, showing the effect of BCB top layer finite thickness. The finger thickness was assumed to be 0.32 μm, which is the measured finger thickness in the fabricated IDCs.

Figure 3.14. A simplified schematic of the auto balancing bridge circuit to measure impedance. A sinusoidal signal is applied to the high (H_C, H_P) terminals and the currents passing through Z_X and R are balanced so that a voltage of zero is maintained at the low (L_C, L_P) terminals. The actual circuit in practical instruments is much more sophisticated.

Figure 3.15. Four-terminal configuration for capacitance measurement.

Figure 3.16. IDC Capacitance values measured in test steps I and II for 1-mm-long IDCs at 0.0 % relative humidity and room temperature.

Figure 3.17. Dielectric constant of BCB before and after finger thickness compensation extracted from equations (3.6) and (3.11), respectively.

Figure 3.18. IDC Capacitance values before and after a humidity stress of 85 %RH at 85 °C for 2 hours.

Figure 3.19. General form of two exponential functions used to describe the I-V characteristic of some solids (AU: arbitrary unit)

Figure 3.20. Circuit for measurement of I-V characteristic of BCB films. The voltage is applied to the device under test (DUT) using a high voltage (HV) power supply. The voltage is measured by a digital multimeter (V), and the current is measured by a picoammeter (PA). The internal current limit of the HV power supply limits the current in case of breakdown.

Figure 3.21. I-V characteristics of 1-mm-long IDCs before and after humidity stress with exponential curve fitting based on equations (3.12) and (3.13) for 2-μm and 3-μm finger width/spacing. R^2 is the coefficient of determination.

Figure 3.22. Strasbaugh 6EC CMP tool. The main unit, including polishing area, control panels, and touch-screen computer is shown.

Figure 3.23. The polishing area of the Strasbaugh 6EC CMP tool. Polishing platen and pad, wafer carrier, polishing arm, and slurry dispenser can be seen. This tool has a 4” wafer chuck inside the wafer carrier.

Figure 3.24. AFM scans of BCB polymer surface cured at 210 ºC showing the effect of CMP with MSW2000A slurry: (a) before CMP, (b) after CMP with recipe I, and (c) after CMP with recipe II.

Figure 3.25. AFM scans of BCB polymer surface showing the effect of CMP using recipe I with ILD1300 slurry: (a) cured at 255 °C, (b) cured at 188 °C, and (c) uncured. Quantitative data is shown in Table 3.6.

Figure 3.26. A schematic of a silicon wafer with several planarized embedded BCB in silicon (EBiS) islands

Figure 3.27. Major fabrication steps of EBiS process: (a) DRIE of silicon to form islands, (b) spin-casting and patterning the first layer of photosensitive BCB polymer, (c) planarizing the BCB islands with CMP, and (d) repeat steps b and c for the second layer of photosensitive BCB polymer with partial-curing to fill and planarize the EBiS island.

Figure 3.28. Optical micrographs of two identical 2 mm × 2 mm EBiS islands on two samples before and after CMP with ILD1300 slurry and recipe I: (a) uncured, and (b) cured at 210 °C (standard soft cure).

Figure 3.29. Optical profiles of BCB ridges around three identical EBiS islands on three samples before and after CMP with ILD1300 slurry and recipe I: (a) uncured, (b) cured at 200 °C, and (c) cured at 210 °C (standard soft cure).

Figure 3.30. Scanning electron micrographs (SEMs) showing the cross section of a 5 mm × 10 mm, 12-μm deep EBiS island after deposition of two BCB layers and planarization. Thin layers of chromium (Cr) and gold (Au) were sputtered on the wafer to help with taking the SEM and to test the adhesion of metal layers.

Figure 3.31. Average island depression in different steps of EBiS process for four test wafers.

Figure 3.32. Average BCB ridge heights in different steps of EBiS process for four test wafers.

Figure 3.33. Average total step height reduction (SHR) in different steps of EBiS process for four test wafers.

Figure 3.34. Optical micrograph of a silicon v-groove etched in 45 wt% KOH solution at 82 °C for 3 hours. The etch rate of (100) plane was 0.8 μm/min and the etch rate of (111) plane was 1.0 μm/hr. The v-groove has a width of 287μm and a depth of 146 μm.

Figure 3.35. Optical micrograph of a DRIE-fabricated trench and a microball. The width of the trench is 290 μm and its depth is 130 μm.

Figure 3.36. Scanning electron micrograph (SEM) of a gray-scale-fabricated rotary v-groove with a sidewall angle of about 35°.

Figure 3.37. Major steps in fabrication of the stator after the completion of the EBiS process: (a) silicon wafer with EBiS islands (first BCB layer), (b) the interconnects and pads (first metal layer), (c) ILD and vias (second BCB layer), (d) the electrodes (second metal layer) and passivation (third BCB layer), (e) photoresist pattern of microball housings (trenches), (f) etched trenches.

Figure 3.38. Optical micrographs of the stator after lift-off of the first metal layer: (a) interconnects and pads on top of the EBiS island and (b) metal pattern on the silicon substrate.

Figure 3.39. Optical micrographs of the stator after spin-casting and developing the BCB ILD layer before the cure step: (a) with a thickness of 2 μm to 3 μm, voids form in the BCB film at the edge of metal structure and (b) with a thickness of 4 μm to 5 μm, voids disappear.

Figure 3.40. Optical micrographs of the stator active area, which consists of three BCB layers and two metal layers: (a) interconnects connect every other six electrodes with each other through vias and (b) an 80 μm × 80 μm via.

Figure 3.41. An optical micrograph of the cross section of the stator active area across the electrodes.

Figure 3.42. A schematic 3D view of a completed stator.

Figure 3.43. Optical micrographs of the completed stators. The microballs are marked by arrows. (a) D_{1SHORT}, (b) D_{2SHORT}, and (c) D_{3SHORT}.

Figure 3.44. Optical micrographs of a completed slider of device D_{2SHORT}. The microballs are marked by arrows: (a) Active area and trenches of in the slider die, (b) size of the slider die compared to a penny, and (c) a microball.

Chapter 4

Figure 4.1. Simulated and measured B-LVCM capacitance (one phase) for device $D2_{SHORT}$. The simulated profile is curve-fitted to a sine-squared function very well.

Figure 4.2. Simulated and extracted (from capacitance data) B-LVCM aligning force for device $D2_{SHORT}$ when excited with a 100-V DC voltage. The force was calculated from sine-squared curve fits to the simulated and measured capacitance data of Figure 4.1.

Figure 4.3. Simulated and measured capacitance of all B-LVCM six phases for device $D2_{LONG}$.

Figure 4.4. Simulated and extracted total aligning force and their average values for device $D2_{LONG}$ when excited with a 100-V P-P voltage. The force is calculated from curve fits to the simulated and measured capacitance data of Figure 4.3.

Figure 4.5. Block diagram of the experimental setup for driving the B-LVCM and characterization of the slider motion.

Figure 4.6. The experimental test setup for driving the B-LVCM and characterization of the slider motion: (a) The camera looking at a B-LVCM under test and (b) the device under test is held down on the device holder with copper tapes. The probe needles apply the six phases of the voltage.

Figure 4.7. Measured slider position vs. time for device $D2_{SHORT}$ when excited with a 3-phase, 10 Hz, 100-V P-P, square-wave voltage (direction was changed at 2 Hz).

Figure 4.8. Measured slider position vs. time for device $D2_{SHORT}$ when excited with a 3-phase, 10 Hz, 100-V P-P, square-wave voltage (direction was changed at 2 Hz) after cleaning the stator and the slider. A more stable motion is observed.

Figure 4.9. Measured slider position vs. time for device $D2_{SHORT}$ when excited with a 3-phase, 20 Hz, 100-V P-P, square-wave voltage (direction was changed at 2 Hz).

Figure 4.10. Measured slider position vs. time for device $D2_{SHORT}$ when excited with a 3-phase, 30 Hz, 100-V P-P, square-wave voltage (direction was changed at 2 Hz).

Figure 4.11. Measured slider position vs. time for device $D2_{SHORT}$ when excited with a 6-phase, 20 Hz, 120-V P-P, square-wave voltage (direction was changed at 1.5 Hz).

Chapter 1: Introduction and Background

Electric micromachines are microelectromechanical systems (MEMS) that are used for conversion of power between electrical and mechanical domains on a microscale. These devices, including micromotors and microgenerators, can potentially provide a substantial amount of mechanical or electrical power (up to a few Watts) over an unlimited or large range of motion. They have a high power density because of their small weight and volume, they can be batch fabricated and integrated with microelectronic circuits using microfabrication processes, and they are inexpensive compared to their macroscale counterparts.

In most portable electronic systems, such as notebook computers, cell phones, etc., the largest single components are usually the power conversion devices, e.g. batteries, motors, fans, and pumps. Since the early days of MEMS, miniaturization of electric machines has attracted the attention of researchers as the primary solution to further reduce the size and cost of portable electronic systems. It is desirable to integrate electric motors and power generators, mechanical pumps and valves, chemical reactors and combustors, and even engines on a single chip to achieve high power density for applications with tight power requirements. In light of scientific and technological advances in microfabrication in the last two decades, electric micromachines are now becoming a promising technology to replace the bulky sources of electrical and mechanical power in a variety of microsystem applications: microscale electrical power generation [1, 2], micropropulsion systems such as micro

air vehicles (MAVs) [3-5], microrobotics and micromechatronics [6], medical instruments and microsurgery [7-9], micropumps for fluid transport [10], storage devices [11], micropositioning systems [12-14], optical switches [15], and diffraction grating scanners [16].

Efficiency, reliability, and manufacturing cost are three critical factors to consider when choosing a technology for a product. Despite the great number of research activities, the technology of electric micromachines is still far from practical applications in industrial and commercial products. Further research is required to develop new ideas, methods, and tools for realization of cost-effective, efficient, reliable electric micromachines.

1.1. Motivation and Objectives

The main objective of this research is to develop a long-range, high-speed, linear, electrostatic micromotor and key enabling technologies to realize efficient, reliable power MEMS devices. The micromotor is designed based on the concept of the bottom-drive, variable-capacitance motor with a thick, low-dielectric-constant (low-k), benzocyclobutene (BCB)-based polymer insulating layer and a microball-bearing support mechanism. The micromotor is the first demonstration of a power microelectromechanical device, which integrates microball bearings and BCB-based polymers in a microfabricated structure. Using an appropriate position sensing and control mechanism, the micromotor could be used as a precision micropositioner with a large travel range. The developed technologies are also applicable to rotary micromachines, such as micropumps and microgenerators.

Improvement of efficiency and reliability are the main motivations behind this research. Generally speaking, high efficiency can be achieved by eliminating or reducing the sources of electrical and mechanical loss and reliability can be achieved by understanding possible mechanisms of failure and using robust design, components, and materials to prevent these failures. Electrical loss and bearing friction loss are two major sources of loss in micromachines that degrade the efficiency. Furthermore, electrical breakdown, friction, wear, and mechanical instability of moving parts (e.g. rotor) are main issues in reliability and robustness of micromachines. Two novel technologies applicable to MEMS electrostatic micromachines have been developed to help with reducing electrical loss, friction, and wear, and stabilizing the mechanical components. In order to implement and demonstrate these new technologies, they have been integrated in a linear, electrostatic micromotor.

Microball bearing technology in silicon is the first key enabling technology in this research. As an alternative to previously developed flange [17], center-pin [17, 18], and gas-lubricated [19] bearings, microball bearings provides a robust, stable, and reliable support for moving parts such as rotor in micromachines. Potentially, a uniform air gap and fairly low friction can be accomplished with simple microfabricated structures. Different designs of microball bearings are considered to be integrated in a linear electrostatic micromotor. The linear micromotor not only demonstrates the application of microball bearings in micromachines, but also helps us to develop an accurate dynamic model and design methodology for microball-bearing-supported micromachines by allowing in situ operation of the bearings.

BCB-based MEMS technology is the second key technology that enables the development of electrostatic micromachines with minimal electrical energy loss in the stator. BCB polymer is an alternative dielectric material to plasma-enhanced chemical-vapor-deposited (PECVD) silicon dioxide, which has a higher dielectric constant and lower thickness limitation due to high residual stress. A BCB insulating layer exhibits much lower parasitic capacitance leading to a significant decrease in the switching loss, which is one of the major sources of electrical loss. It also exhibits lower residual stress leading to less wafer bow and improved uniformity of the motor air gap. Electrical and mechanical characterization of BCB polymers as insulating dielectric materials enables application of these polymers in electrostatic micromachines. In addition, demonstration of low electrical loss and high efficiency in electrostatic micromachines using thick, low-k BCB polymers is among objectives of this research.

1.2. Electric Micromachines

1.2.1. Electrostatic vs. Magnetic Micromachines

The electrostatic forces are by nature much larger than the magnetic forces in absence of magnetic materials. By simply applying Coulomb's and Ampere's Laws to the fundamental sources of electric and magnetic fields (charge and current, respectively), we can find that the electrostatic force between two 1×10^{-6} C point charges separated by 1 m in vacuum is around 9×10^{-3} N, while the magnetic force between two wires carrying currents of 1×10^{-6} A separated by 1 m in vacuum is only 2×10^{-19} N. Although it seems that electrostatic actuation has an advantage over the

magnetic actuation, the macroscale world of electric machinery is dominated by magnetic machines. Almost all electric motors and generators in industry and commercial applications are based on the exchange of energy between mechanical components and magnetic field. The reason lies in the fact that using magnetic materials in the construction of magnetic machines significantly increases the energy storage capacity of the machine. The force (or torque) produced by an electric machine is closely related to its capacity to store the electromagnetic energy. In other words, a machine produces a force (or torque) of electric nature if the stored energy in the air gap (capacitance in case of electrostatic machines and inductance in case of magnetic machines) has spatial variations. It can be shown that the surface force density (which causes the motion) applied to the rotor in an electric machine is equal to the air gap stored energy density [20]. Therefore, the air gap energy density will be used as a figure of merit to compare the performance of electrostatic and magnetic machines.

The magnetic energy density in the gap of a magnetic machine is $w_m = B^2/2\mu_0$, where B is the magnitude of the magnetic flux density in the gap and $\mu_0 = 4\pi\times10^{-7}$ H/m is the permeability of free space [21]. Therefore, the energy density is limited by the maximum achievable magnetic flux density, which occurs at the saturation of the magnetic material. As an example, M-5 steel, a typical grain-oriented electrical steel used as a ferromagnetic material is heavily saturated at a flux density of about 1.7 T [22]. Some motors, such as switched reluctance machines can operate saturated, therefore, a rough estimate for the maximum flux density can be 2 T [23]. However, the actual maximum flux density is less due to practical limitations

such as space required for winding conductors. This leads to a practical maximum flux density of about 1 T [23], which means a maximum energy density of 400 kJ/m^3 and a surface force density of 400 kPa is achievable in the air gap of a magnetic machine. This is essentially independent of the gap size.

The electrostatic energy density in the gap of an electrostatic machine is $w_e = \varepsilon_0 E^2 / 2$, where E is the magnitude of the electric field in the gap and ε_0=8.854×10^{-12} F/m is the permittivity of free space [23]. The maximum achievable electric field in vacuum is limited by field emission (Fowler-Nordheim tunneling), which occurs at electric fields in the range of 3×10^9 V/m to 6×10^9 V/m [24]. Assuming a maximum electric field of 1×10^9 V/m, the maximum energy density in the gap of an electrostatic machine in vacuum is 4.5 MJ/m^3 and the maximum surface force density is 4.5 MPa, which are one order of magnitude larger than those of magnetic machines. However, vacuum gap machines are not practical since the gap has to be sealed off from the atmosphere. The maximum achievable electric field in presence of an insulator such as air in the gap is limited by electrical breakdown, which is well below the field emission point. A typical value for the maximum electric field in air for large gaps and atmospheric pressure is on the order of 3×10^6 V/m. This leads to a maximum energy density of 40 J/m^3 and a surface force density of 40 Pa in an electrostatic machine, four orders of magnitude smaller than those of a magnetic machine, explaining why macroscale electrostatic machines do not have real applications.

Contrary to the magnetic energy density, the electrostatic energy density is a function of the gap size. The breakdown field in a gas is governed by an empirical

relation known as Paschen's Law discovered by Paschen in 1889 and can be written as [25]:

$$E_B = 100 \frac{Bp}{\ln\left[\frac{Apd}{\ln(1/\gamma)}\right]} \tag{1.1}$$

where E_B is the electric field (in V/m) at breakdown, p is the gas pressure (in Torr), d is the gap size (in cm), and A, B, and γ are constants depending on the gas type and electrode material. For an air gap at atmospheric pressure (p = 760 Torr), (1.1) can be written as [25]:

$$E_B = \frac{2.8 \times 10^7}{7.8 + \ln d} \tag{1.2}$$

which shows a dramatic increase in the breakdown electric field as the gap size decreases. Note that (1.2) has a singularity around d = 4 μm and is not valid for smaller gaps, where breakdown is dominated by field emission. Although the experimental data does not exhibit such a singularity, a drastic increase in the breakdown electric field for small gaps is observed. The breakdown electric field and the breakdown voltage ($E_B d$, assuming a uniform field) are plotted vs. gap size in Figure 1.1. The maximum achievable electrostatic and magnetic energy densities are plotted vs. gap size in Figure 1.2, showing that in the microscale regime the energy densities of electrostatic and magnetic machines are comparable.

In addition to the energy density and surface force density argument, there are technological factors that are in favor of electrostatic micromachines rather than magnetic micromachines. There has been an increasing trend in research on magnetic materials and magnetic actuators in recent years [10, 26-34], however, the

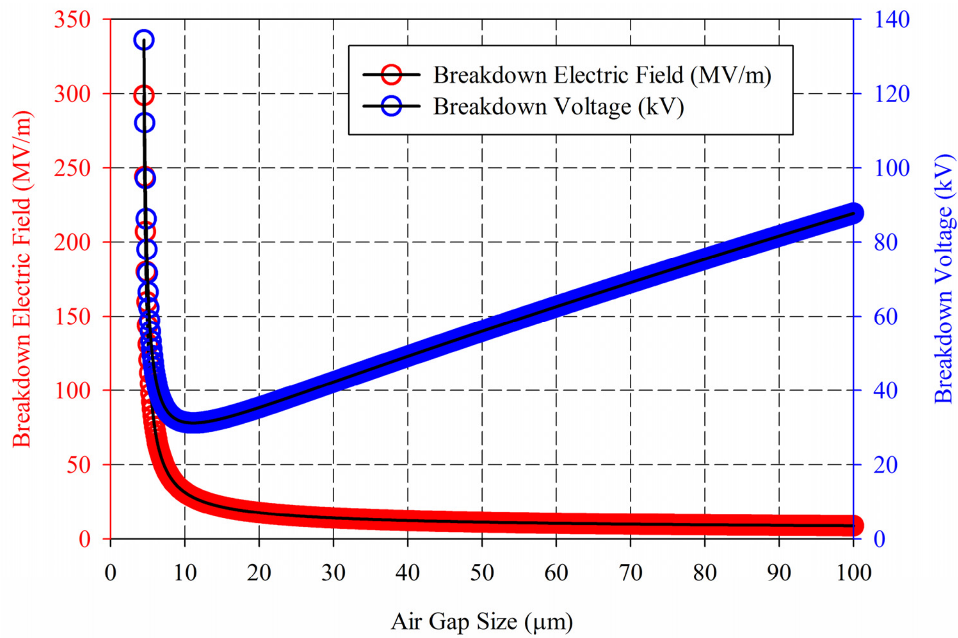

Figure 1.1. Breakdown voltage and electric field in air at atmospheric pressure as predicted by Paschen's Law.

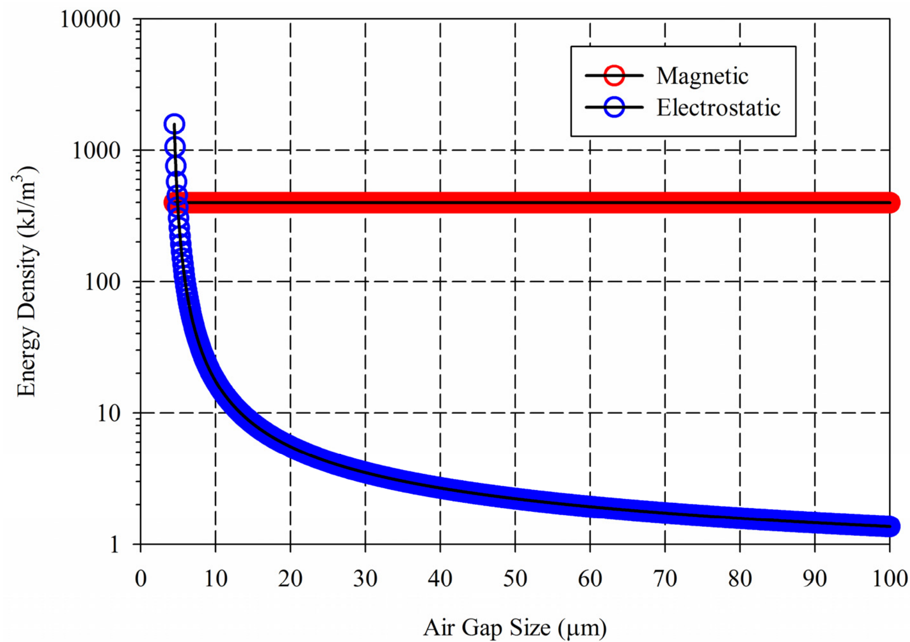

Figure 1.2. The limit of energy density in electrostatic and magnetic machines vs. air gap size.

compatibility of these materials with MEMS and microelectronic fabrication processes is still a challenging issue. In addition, the saturation limit in these newly developed materials is far lower than 1 T, leading to a much smaller energy density. Furthermore, in most magnetic micromachines, the magnetic field is produced by current flowing in microfabricated conductors with resistivities higher than macroscale counterparts. In this case, the energy density is limited by thermal considerations rather than saturation [23].

Based on the above arguments, we chose an electrostatic micromachine for demonstration of new technologies and system integration because it allows us to avoid the complexities and pitfalls associated with magnetic micromachines. However, the microball bearing technology in silicon used in this research can be utilized in a variety of applications including electrostatic and magnetic micromachines.

1.2.2. Review of Previous Research on Electrostatic Micromachines

Electrostatic motors – probably for the first time – were built by Andrew Gordon and Benjamin Franklin in the 1750s, 100 years before magnetic motors. The first variable-capacitance motor was built by Karl Zipernowsky in 1889 [35]. Despite this long history, macroscale electrostatic machines are not favored in practical applications, but surprisingly there have been extensive research activities on analysis, design, and prototyping these machines [36-39], providing the concepts and design expertise for microscale electrostatic machines. Advances in MEMS technology in the last two decades, adopted from integrated circuit (IC) fabrication technology, made the development of electrostatic micromachines a reality. A great

number of publications on design and fabrication of different types of electrostatic micromachines can be found in the literature. Most research activities have been focused on micromotors rather than microgenerators. However, electrostatic micromotors can theoretically operate in generator mode too. One of the main challenges in realization of micromachines is the electrical energy loss, which drastically decreases the efficiency (this is more critical in case of microgenerators). An approach to minimize this loss is to reduce the parasitic capacitance of the machine using a thick, low-dielectric-constant insulating layer and is discussed in Chapter 3.

In most electrostatic micromachines, the stator structures are similar, consisting of a series of planar conducting electrodes insulated from the substrate. The major distinguishing feature in different types of electrostatic micromachines is the rotor structure, which defines the induced charge distribution [40]. In addition, for almost any electrostatic machine (except the corona discharge), there exists a magnetic dual [41], which is well studied in electric machine theory. Table 1.1 shows most types of electrostatic micromachines, along with their mechanism of charge separation and magnetic duals. It should be noted that there are other types of micromachines based on elastodynamic actuation not listed in Table 1.1, including but not limited to piezoelectric [42, 43] and ultrasonic [44] machines. These are not included because the rotor thrust is produced by frictional forces rather than electrostatic forces. Elastodynamic micromotors generally have the highest torque but the lowest speed, and suffer from wear.

Table 1.1. Types of electrostatic machines

Electrostatic Machine	**Charge Distribution Mechanism**	**Magnetic Dual**
Variable Capacitance	Pole Saliency	Variable Reluctance
Electrostatic Induction	Charge Relaxation	Magnetic Induction
Permanent Electret	Embedded Fixed Charge	Permanent Magnet
Corona Discharge	Microionization	N/A
Dielectric Hysteresis	Hysteresis in Polarization	Magnetic Hysteresis

Corona discharge micromotors [45] are based on the ionization of air in a high electric field concentrated at a sharp tip. The accelerated ions apply a thrust to the rotor leading to motion. Macroscale corona motors need thousands of volts to operate. MEMS technology has enabled the development of low-voltage corona micromotors by providing the fabrication technology of extremely sharp tip arrays located at very small distance from electrodes. However, due to the likelihood of arc breakdown and erosion of emitting tips, corona micromotors are not very common.

Permanent electret micromotors and microgenerators [45, 46] have also been investigated. These machines exploit dielectric materials such as silicon dioxide on the rotor that can be permanently charged to generate a permanent electric field. The major drawbacks of these types of micromachines are the instability of permanent electrets and the need for high-voltage equipment to charge them.

Most of the research activities in the area of electrostatic micromachines have been on variable-capacitance and electrostatic-induction micromachines. These machines have similar structures and designs with minor differences in the rotor design, which leads to different principle of operation.

The electrostatic-induction machine is asynchronous. In this machine, the rotor consists of a poor conducting film insulated from the substrate. The induced

charges on the rotor conduct through this film to follow (in motor mode) or to lead (in generator mode) the potential traveling wave of the stator. Since the film is a poor conductor, there will be a phase difference between the potential waves of the stator and rotor. As a result, a tangential electric field builds up that applies a force (or torque) to the rotor. The operation, design, modeling, fabrication, and test of macroscale electrostatic induction machines have been investigated in [36, 47-49]. The design and modeling of electrostatic induction micromachines have been studied in [40, 50], and the fabrication details and test of these micromachines can be found in [40, 50, 51]. The main advantage of the electrostatic induction machine over the variable-capacitance machine is that the induction machine is asynchronous, making the excitation and control easier [52]. However, in general the time constant of the rotor film determines the mode of operation, whether the machine is running asynchronously or synchronously [53]. In addition, the output power and efficiency of the machine, even in asynchronous mode, is very sensitive to the time constant of the rotor film. This is a disadvantage considering that precise control of the conductivity of the rotor film is a big challenge.

Variable-capacitance machines are synchronous. The operation principle and basic design of the variable-capacitance machines has been described in [36, 39] and will be discussed in detail in Chapter 2. The design and modeling of variable-capacitance micromotors started in the late 1980s [36, 54-56]. The fabrication technology of these micromachines was primarily developed at MIT and UC Berkeley in late 1980s and early 1990s [17, 18, 57, 58]. These efforts led to successful fabrication of the first functional electrostatic micromotor based on

polysilicon surface micromachining technology [59, 60]. Rules and principles of the design and fabrication of polysilicon, surface-micromachined, variable-capacitance micromotors were formulated in [61-63]. Dynamics and test of these machines have been studied in [61, 64]. These early micromotors operated using a side-drive mechanism with center-pin or flange bearings and suffered from two major drawbacks: small torque, and high friction and wear. The active area in these side-drive micromotors was limited to the rim of the rotor, producing a small torque in the range of several pNm. The bearing mechanism was fairly primitive with sliding motion, leading to high friction and wear. The rotor speed in the Berkeley micromotor was reported to be as low as 500 rpm due to high friction [65]. The MIT micromotor was reported to operate at 15000 rpm (the mechanical speed was not experimentally verified, but the device was actually operated at an excitation frequency of 1000 kHz, which was corresponding to a rotor speed of 15000 rpm.) [63]. The motors stopped working after one week due to bearing wear [66]. Figure 1.3 shows a schematic cross-section view and an optical micrograph of the first electrostatic micromotor fabricated at Berkeley Sensors and Actuators Center, UC Berkeley [59].

Modern micromotors, such as the one developed in this research, rely on bottom-drive mechanisms to increase the motor active area. This approach in combination with novel bearing technologies and new dielectric materials can produce micromachines with high torque, speed, and reliability.

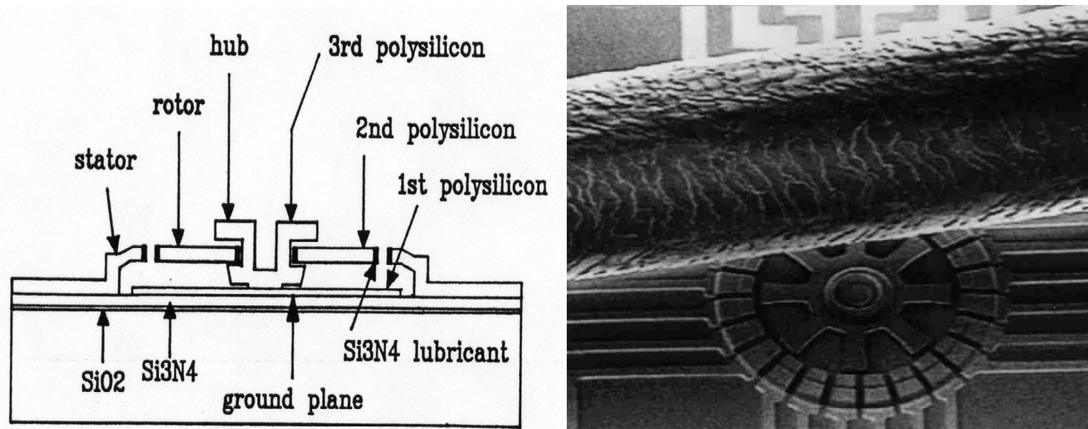

Figure 1.3. Schematic cross-section (left) and optical micrograph (right) of the first electrostatic micromotor developed at UC Berkeley. A human hair is shown next to the micromotor on the optical micrograph for comparison [61].

1.3. Dielectric Films in Microelectromechanical Systems

1.3.1. Review of Dielectric Films for Electrostatic Micromachines

In most electrostatic micromachines, a dielectric film is used to insulate the electrically active components from the substrate. It also serves as the interlevel dielectric (ILD) in multilevel metallization, usually on the electrical stator to insulate metal lines from each other. Figure 1.4 illustrates a schematic cross section of a stator in a typical micromachine showing dielectric layers and related parasitic elements. The physical properties of the dielectric film have a major impact on the electrical efficiency and reliability.

The very early micromachines were side-drive, variable-capacitance micromotors fabricated with polysilicon surface micromachining technology [17, 18, 57, 59, 67]. In these devices, the electrical insulating layer mainly consisted of 1- to 2-μm-thick films of thermal silicon dioxide or liquid-phase chemical-vapor-deposited (LPCVD) silicon nitride, exhibiting large stress (in the range of hundreds of MPa to a

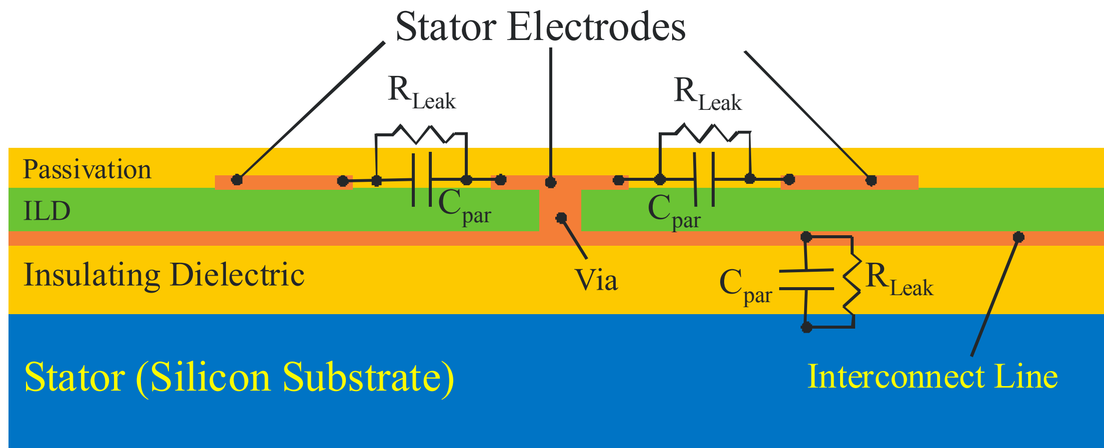

Figure 1.4. Cross-section view of the stator in a typical polyphase electric micromachine showing the dielectric insulating layers and the associated parasitic elements. (Dimensions are not to scale.)

few GPa) and high dielectric constant (k>4), with several mechanical and electrical reliability issues. The development of the first micromotors [59] was a successful demonstration of energy conversion on a microscale, however, the level of power, efficiency, and reliability achieved was not satisfactory for the power demands in microsystems.

The demand for high power and efficiency in electrostatic micromachines has pushed the required thickness of the electrical insulating layer to tens of micrometers to meet the voltage and energy loss requirements. It has also initiated many research activities on the use of tetraethylorthosilicate (TEOS)-based and silane-based PECVD silicon dioxide to develop crack-free, low-stress, thick insulating layers [68-72]. The major issues in the development of thick PECVD silicon dioxide films were wafer bow and cracks developed during annealing process as a result of excessive residual stress. A 10 μm-thick PECVD silicon dioxide film can induce a large wafer bow of 230 μm and the film starts to crack when the thickness goes beyond 15 μm [69].

Thick buried oxide in silicon (TBOS) [69] was developed as an integrated fabrication technology to develop crack-free films and to reduce the wafer bow by 50 % in the electrical stator of a high-voltage micromotor. However, the reduced wafer bow was still large and the crack-free film thickness could not exceed 26 μm. Furthermore, the dielectric constant of PECVD silicon dioxide is relatively high (k=3.9-4). These challenges open plenty of room to introduce new fabrication technologies and new materials as possible replacements for thick silicon dioxide films in electrostatic micromachines.

A dielectric material must have certain properties to (i) minimize the electrical energy loss, hence, maximize the electrical efficiency, (ii) maximize the power conversion capacity, and (iii) maximize the device reliability. These features include good electrical properties such as low dielectric constant, high dielectric strength, high volume resistivity, and low dissipation factor, as well as good mechanical properties such as low residual stress. In addition, an ideal dielectric material must possess good process capabilities such as a wide range of film thickness, high degree of planarization, low process temperature, and good thermal stability at high temperatures. However, none of the existing dielectric materials has all these features. A trade-off is therefore necessary based on the given application and its target requirements.

Most electric micromachines operate under high alternating-current (AC) voltages with some limitations in electrical efficiency and reliability. High-voltage operation is basically limited by electrical breakdown, which is likely to occur in the dielectric insulating layers and the air gap. The electrical efficiency and power

conversion capacity are limited by the amount of stored reactive power in the capacitive loads as well as the dielectric loss in the insulating layers. These behaviors are directly related to the electrical properties of the dielectric films used in the device. The parasitic capacitances between the electrical components and the substrate, and also between the adjacent excitation phases, contribute to the switching electrical loss due to the nonzero resistance of the interconnect lines. The switching loss occurs during the charging/discharging. The dielectric loss in the insulating layers contributes to power dissipation and electrical energy loss. The dielectric loss has two components: the loss associated with leakage currents in the dielectric due to electron and ion drift currents, and the loss associated with displacement currents due to space charge polarization and dielectric dipole motion, the latter being more important at high frequencies.

Two key components to maximize the reliability and to minimize the electrical energy loss associated with the insulating dielectric layer are the thickness and the dielectric constant. Figure 1.5 shows the result of a finite-element simulation on how the parasitic capacitance between the stator electrodes and substrate of a six-phase electric micromachine changes with the thickness of the insulating layer. The effect of dielectric thickness on device efficiency was also investigated in previously reported work on an electric induction machine, showing a 25% increase in system efficiency if the thickness of the stator dielectric layer was doubled [73]. The parasitic capacitances are also directly proportional to the dielectric constant of the insulating layers. Therefore, it is desirable to have a thick, low-k dielectric film for the insulating layer. However, realization of thick films in microfabrication encounters

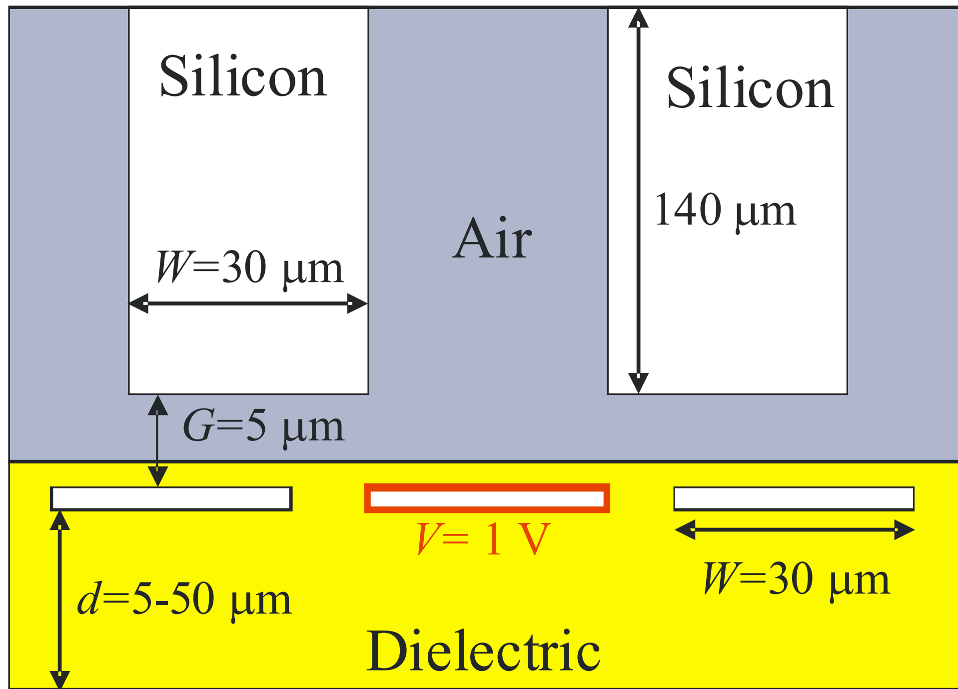

(a)

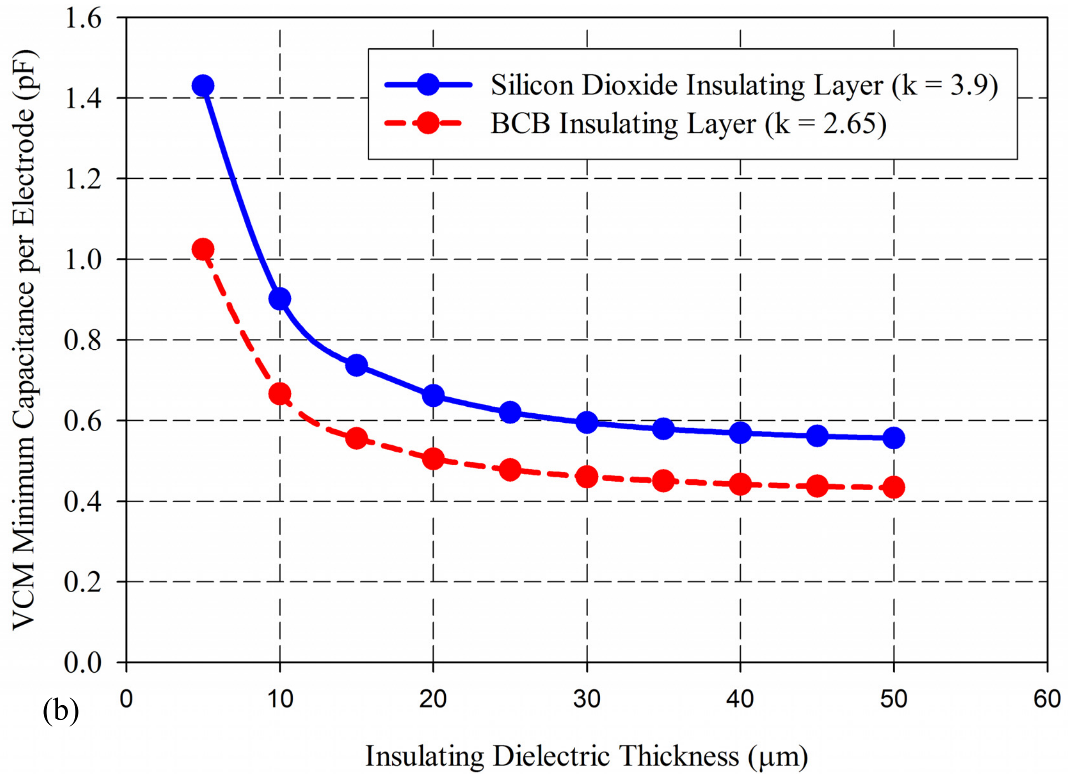

(b)

Figure 1.5. Simulation of the minimum capacitance per electrode vs. the insulating layer thickness in a six-phase variable-capacitance micromachine: (a) Problem definition and simulation model, and (b) data for. silicon dioxide and BCB.

challenging mechanical issues, i.e. a substantial amount of residual stress that can lead to large wafer bow and film cracks. Furthermore, application of low-k materials faces additional challenges such as thermal instability at high temperatures and moisture uptake during device lifetime that degrades breakdown strength and leakage current.

1.3.2. Spin-on Low-Dielectric-Constant Benzocyclobutene Polymers

Low-k polymers based on benzocyclobutene (BCB) [74, 75] are among the promising alternatives to PECVD silicon dioxide for a variety of applications. These polymers are commercially available from the Dow Chemical Company under the registered trademark called Cyclotene. Cyclotene is a family of thermosetting polymer materials prepared from 1,3-divinyl-1,1,3,3-tetramethyldisiloxane-bisbenzocyclobutene (DVS-bis-BCB) monomer [76, 77]. The chemical structures of BCB and DVS-bis-BCB are shown in Figure 1.6. In this text we refer to Cyclotene as BCB unless otherwise noted.

BCB is available in two categories: dry-etch and photosensitive, both in the form of spin-on solutions. The dry-etch BCB comes in different viscosities to obtain cured films with thicknesses in the range of 1 μm to 26 μm and contains B-staged (i.e. partially cross-linked) DVS-bis-BCB monomer in mesitylene solvent. The

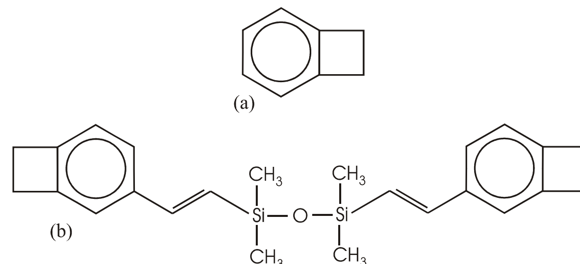

Figure 1.6. Chemical structures of (a) BCB and (b) DVS-bis-BCB monomers.

photosensitive BCB is also supplied in different viscosities to obtain cured films with thicknesses in the range of 2.5 μm to 14 μm and contains a photoactive component in addition to the B-staged monomer and the solvent. The photosensitive BCB is negative acting during photolithography and sensitive to a broad range of ultra violet (UV) wavelength including G-line and I-line. Table 1.2 shows the available lines of BCB and the film thickness ranges. Thinner films can be achieved by diluting the solution with mesitylene, while thicker films can be obtained by spin-casting the solution in multiple layers. Table 1.3 summarizes some of the general processing features of BCB. Table 1.4 shows some of the electrical and mechanical properties of BCB based on the previously reported works and the manufacturer's data sheets. Typical properties of silicon dioxide are shown for comparison.

BCB was primarily developed as an ILD and passivation coating in microelectronic interconnects and packaging for application in multichip modules (MCM) [78-81]. BCB features simplified processing, low dielectric constant, high degree of planarization and gap filling, low moisture absorption, and low-temperature cure. Another key feature of BCB is that a wide range of film thickness is achievable

Table 1.2. Viscosity and Film Thickness of Different Lines of Cyclotene

Solution		**Viscosity (cSt @ 25 °C)**	**Thickness of Cured Film (μm)**
Dry-etch	3022-35	14	1.0 - 2.4
	3022-46	52	2.4 - 5.8
	3022-57	259	5.7 - 15.6
	3022-63	870	9.5 - 26.0
	XU-71918.30	8.9	1.0 - 1.5
Photosensitive	4022-35	195	2.5 - 5.0
	4024-40	350	3.0 - 7.5
	4026-46	1100	7.0 - 14.0

Table 1.3. Processing Features of Cyclotene

Process	**Method**	**Details**
Surface Treatment	Adhesion Promoter	AP3000
Deposition	Spin-coat	1000-5000 rpm
Soft Cure	Furnace	N_2, 1h @ 210 °C
Hard Cure	Furnace	N_2, 1h @ 250 °C
Etching	Plasma	O_2/CF_4 or O_2/SF_6

(up to tens of micrometers). These characteristics were found to be useful in many other microelectronic applications, such as damascene copper interconnects [82], flip-chip solder bumping [83, 84], flat panel displays and charged-coupled devices, optical waveguides [85-87], RF high-Q inductors [88, 89], stress buffer and passivation layers [90], and microsensors [91]. The application of BCB in MEMS has been mainly limited to packaging and adhesive bonding [92-95]. More recently, fabrication of a BCB diaphragm for an infrared thermopile detector has been reported [96, 97]. One of the main challenges in application of BCB film in MEMS is its integration with conventional MEMS fabrication processes, such as bulk micromachining.

Some of the outstanding features of BCB, such as low dielectric constant and large film thickness, are well suited for electrostatic micromachinery applications. Numerical simulations show that if a 10 μm thick PECVD silicon dioxide film is replaced with a 25 μm BCB film in the stator of a six-phase electrostatic micromachine, the parasitic capacitive loading of the insulating dielectric film decreases over 40 % due to the possible increased thickness and reduced dielectric constant (see Figure 1.5). This is a remarkable improvement for the electrical efficiency of the machine, not to mention the fabrication difficulties involved in developing a 10 μm thick PECVD silicon dioxide film.

Table 1.4. Physical Properties of BCB Polymer based on the manufacturer's data sheet and Silicon Dioxide (at 25 °C unless otherwise noted)

	Physical Properties	Unit	Silicon Dioxide	BCB Polymer
Electrical	Dielectric Constant		3.9	2.65
	Dissipation Factor		0.0002	0.0008 – 0.002 (1 MHz –10 GHz)
	Dielectric Strength	V/m	$6 – 9 \times 10^{8}$	3×10^{8}
	Volume Resistivity	Ω.m	1×10^{16}	1×10^{21}
Mechanical	Density	Kg/m^3	2190	1050
	Tensile Strength	MPa	69 – 276	85 ± 9 (dry-etch) 87 ± 9 (photo.)
	Tensile Modulus	GPa	73	2.0 ± 0.2 (dry-etch) 2.9 ± 0.2 (photo.)
	Tensile Elongation	%		8 ± 2.5 (at break)
	Poisson Ratio		0.17	0.34
	Residual Stress on Si	MPa	100 – 300 (comp.)	28 ± 2 (tensile)
Thermal	Thermal Conductivity	W/m.K	1.4	0.29
	Specific Heat	J/kg.K	1400	2180
	CTE	ppm/°C	0.5	52 (at 25 – 300 °C)
	Transition Temperature	°C	1710 (melting)	350 (glass temp.)
	Thermal Weight Loss	%/hr		1.6 (at 350 °C)
Optical	Index of Refraction		1.46	1.54 (at 1300 –1550 nm)
Miscellaneous	Moisture Uptake	%		0.13 (dry-etch, 81 %RH) 0.14 (photo., 84 % RH)
	Shrinkage	%		< 5
	Planarization	%		> 90

There are two major concerns in using BCB films for high-power MEMS applications. One concern is the thermal stability of the polymer at operating temperatures commonly used in high-power devices. As Table 1.4 shows, the glass transition temperature (T_g) of BCB is close to 350 °C. Application of BCB in

micromachines operating at temperatures exceeding 350 °C is possible by using either a cooling mechanism or a specific design, which thermally isolates the BCB films from high-temperature spots. However, there are a variety of applications that operate at temperatures well bellow the glass transition of BCB. The second concern regarding BCB is whether the small moisture uptake in the BCB film degrades the electrical and mechanical properties that might affect the design and the performance of the electric micromachine. Therefore, it is important to characterize the main properties of the dielectric film for the target application. Furthermore, it is essential to investigate the effect of moisture on these properties. These issues will be addressed in Chapter 3.

1.4. Bearing Mechanisms in Micromachines

Bearings are one of the major mechanical components in machinery applications. Considering the role of bearings in providing a support mechanism for moving parts and reducing friction and wear, they have a pivotal impact on performance and reliability. Bearing technologies in macroscale machines are well advanced, while it is still in developing stages in micromachines.

Since the advent of the first micromotor in the late 1980s [59], several different bearings and support structures were demonstrated for use in micromachines based on two categories: contact-type and noncontact-type. Early contact-type bearings, such as flange and center-pin bearings with sliding bushings support in the polysilicon surface-micromachined micromotors, suffered drastically from friction and wear due to the sliding nature of the motion [98, 99]. The friction and wear issues were less serious in wobble [100] and conical [101] micromotors, however, with a

downfall in terms of rotation speed. Different types of MEMS-based roller bearings such as stainless-steel ball bearings [102, 103] and fiber-optic roller bearings [104] were also been investigated in previous research showing superior performance compared to other contact-type bearings. Noncontact-type bearings with more complicated support mechanisms such as electrostatic levitation [105], magnetic levitation [30], and gas-lubricated [50, 106] schemes have also been investigated. They show much less friction and almost no wear compared to contact-type bearings, with two major drawbacks: fabrication complexity and rotor instability.

Among the contact-type bearings, ball bearings seem promising for many future micromachinery applications because (i) the bearing mechanism is relatively simple, (ii) the rolling motion of the balls exhibits much less friction than other contact-type bearings, and (iii) the balls provide a stable, robust mechanical support for the rotor. Linear microball bearings may be used in applications such as precision, long-range micropositioners for optical alignment or storage devices. Rotary microball bearings have applications in high-power microturbomachines such as micromotors, micropumps, microcoolers, microcompressors, and microgenerators.

1.5. Dissertation Overview

This dissertation consists of 5 chapters including this chapter. Chapter 2 is dedicated to the design and modeling. It provides a fundamental understanding of the principle of operation of the variable-capacitance micromachines both in motor and generator modes. The electrical and mechanical characteristics and the energy conversion cycles of these machines are also discussed. The basic and detailed designs of a bottom-drive, linear, variable-capacitance micromotor (B-LVCM) are

presented. The stator and slider designs including the microball bearings and active areas are provided. An estimation of the motor capacitance, force and speed in steady-state condition, and power and efficiency are also presented. The electromechanical modeling of the B-LVCM using lumped-circuit elements and finite-element analysis (FEA) is discussed and the electromechanical behavior of the device, including force and speed in both transient and steady-state conditions are predicted.

Chapter 3 discusses the detailed fabrication processes used to develop the micromotor. The stator and slider fabrication and system integration are also discussed. This chapter also covers the material and process characterization, describes the BCB-based MEMS technology that is developed in this research to address the electrical loss in electrostatic micromachines, and introduces the theoretical and experimental techniques used for electrical characterization of BCB polymers. An integrated fabrication method called *embedded BCB in silicon (EBiS)*, which was used in the development of isolated BCB regions for the fabrication of the micromotor, is described. Chemical mechanical planarization (CMP) of BCB polymers, which is the key process in EBiS is characterized.

Chapter 4 provides the methods and results of testing and characterization of the device. The experimental setup used for testing and characterization are also described. A comparison between experimental results and model prediction are presented.

Chapter 5 provides concluding remarks and a summary of the research. Main lines of future work are also suggested.

1.6. Contributions

The major contributions of this dissertation are novelty in design and fabrication of a linear electrostatic micromotor and the integration of two novel technologies in a microfabricated device. The fabrication of the device consists of several unit processes, which have been designed, developed, characterized, and integrated into a consistent, repeatable process flow. The developed device is the first operational micromachine supported on microball bearings integrated with the electrical stator. It is also the first MEMS device that uses BCB polymers as an alternative to silicon dioxide for isolation of electrically active components.

The bottom-drive design of the micromotor allows the exploitation of a large active area, leading to generation of a large force. The variable-capacitance mechanism of the motor simplifies the structure and fabrication of the slider. The EBiS process provides excellent electrical isolation with the advantage of low electrical loss and mechanical robustness. The microball bearings reduce the friction and wear with increased reliability and robustness.

The methods and technologies developed in this dissertation can be used as a design and fabrication platform for a variety of microelectromechanical (MEM) devices and systems. Micropumps and Microgenerators are two prime examples of future applications of this research.

Chapter 2: Device Design and Modeling

A variable-capacitance machine is basically a variable capacitor that acts as a transducer interfacing the electrical and mechanical domains and exchanging energy between the two domains. The energy exchange is done through the variation of the machine capacitance with the position of the moving part (i.e. the rotor). Based on the direction of the energy flow, the machine operates in the motor or generator mode.

Variable-capacitance motors (VCMs) are among the few earliest microelectromechanical devices that were successfully fabricated in the late 1980s. These early devices were planar electrostatic micromotors built with surface micromachining technology [57, 63, 65]. Due to the limitations of microfabrication technology at the time, these motors exploited a side-drive mechanism with a radial gap, leading to extremely small mechanical torque and output power. In addition, lack of thick dielectric films and high-performance bearings, and the limitations in integration of electrical and mechanical components all contributed to problems such as high power loss and low reliability.

Despite the fact that VCMs are not well-suited for macroscale applications, the theory of the VCM is very well developed. In the microscale domain, however, the implications of Paschen's Law leads to potential useful applications for VCMs (see Section 1.2.1). The major advances of microfabrication technology since the advent of the first microfabricated motor have made the implementation of high-performance VCMs feasible. However, there are still major challenges to be addressed when it comes to efficiency, power density, and reliability.

One of the main features of the VCM compared to other types of electrostatic machines is the simple structure of its rotor. As a result, it provides two major advantages over alternative devices: better accuracy in controlling the fabrication tolerances and higher reliability of the fabricated device. The VCM can provide an output power, torque/force, and energy efficiency comparable to (if not exceeding) those of most other types of electrostatic micromotors.

In this chapter, we review the important characteristics of variable-capacitance machines with an emphasis on motors. Our focus is mainly on planar, axial gap, bottom-drive VCMs although the implications can be applied to VCMs in general. It should also be mentioned that the basic principles apply to both rotary and linear VCMs. The design and modeling of the linear micromotor with linear microball bearings are also covered in this chapter.

2.1. Variable-Capacitance Machines in Motor Mode

2.1.1. Principle of Operation

When a variable-capacitance machine operates in the motor mode, the energy flows from the electrical to the mechanical domain. This is achieved by changing the applied voltage or charge, leading to a change in the rotor position, and consequently, a change in the machine capacitance toward an equilibrium state of the system. Part of the input electrical energy will be converted to the output mechanical energy and the rest will be stored in the capacitor.

A VCM is a synchronous motor similar to its magnetic dual counterpart, the variable-reluctance motor (VRM). While a VRM is driven by current and stores the energy in the magnetic field, a VCM is driven by voltage and stores the energy in the

electric field. The synchronous operation of the VCM will be discussed later in this chapter.

In a VCM, the stator consists of a set of conducting electrodes and the rotor is a piece of conductor with a salient pole structure. The stator and the rotor are separated from each other by an air gap. The variable capacitor of the VCM is formed by the stator electrodes and the rotor poles. The capacitance of the motor varies with the position of the rotor due to the saliency of the pole structure. This variable capacitor is the key element for electromechanical energy conversion.

The principle of operation of a basic form of VCM, a single-phase, two-pole motor is illustrated in Figure 2.1 [36]. The stator and the rotor are two isolated pieces of metal, each consists of two blades. The stator blades (electrodes) are excited by a square-wave voltage shown in the figure. For motor operation, the stator and rotor blades must be initially misaligned, otherwise the rotor will not move. When a voltage is applied to the electrodes, since the rotor is a conductor and charge carriers can freely move on its surface, the electrostatic charges are induced on the surface of the rotor blades (poles). In other words, the motor capacitor is charged and the electrical energy is stored in the capacitor. The structure of the poles plays a major role in defining the distribution pattern of the charges on the rotor surface. In other words, the poles create (relatively) isolated islands on the rotor where most of the surface charge will concentrate. If the poles are initially misaligned to the active electrodes, an electrostatic force is built up due to the presence of the electric field and the concentration of the surface charges on the pole. This force, being applied to the rotor, can be decomposed to an aligning force (shear force) and a normal force.

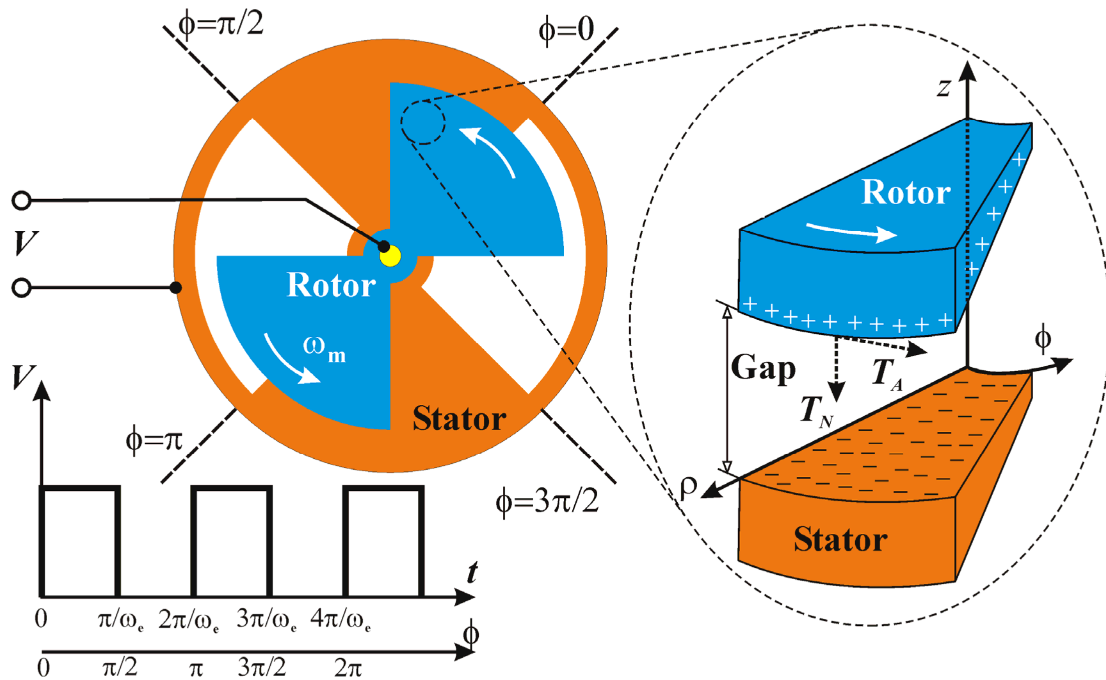

Figure 2.1. Principle of operation of a simple variable-capacitance motor (VCM). T_A and T_N are aligning and normal torques, respectively. Note that at the moment shown in the figure the stator blades are being excited.

Since dealing with torque is much easier in rotary motors, the aligning and normal torques are shown in Figure 2.1. The desired motion of the rotor is in the azimuthal direction in a plane parallel to the stator plane; therefore, the motion of the rotor in the normal and radial directions is restricted by means of a center-pin bearing (see Section 1.4). Provided that the aligning force can overcome the resisting forces, such as friction, viscous drag, etc., the rotor moves to align the poles with the electrodes. The direction of the rotor motion depends on its initial position. Therefore, there is no actual control over the direction of rotor motion in a single-phase VCM.

From Figure 2.1, it is understood that for a continuous rotation of the rotor, it has to be synchronized with the excitation frequency. This means that for every excitation frequency (as long as it is not beyond the frequency limitation of the system), there is a unique rotation speed, or *synchronous* speed. In fact, for a single

rotation of the rotor of the VCM shown in Figure 2.1, there are two periods of the excitation voltage. It will be shown later in this chapter that the aligning force produced by a VCM is proportional to the square of the excitation voltage and to the spatial gradient of the motor capacitance. Similar proportionality exists for the normal force. In addition, by a first-order approximation, the aligning force is inversely proportional to the gap (G) while the normal force is inversely proportional to the square of the gap (G^2). This generally leads to a much larger normal force compared to the aligning force. Although the normal force does not directly impact the rotor motion, it contributes to resisting forces, such as friction.

It should also be noted that in a VRM, the magnetic dual of the VCM, the poles always appear in pairs (due to the nature of the magnetic field), and for the machine to be functional, the stator and the rotor have to have the same number of poles [107]. This is not the case in a VCM, where the poles do not have to be in pairs and the stator and the rotor can have different number of poles. However, to keep the duality between VRM and VCM equations, we should consider the number of VCM poles to be twice what it actually is. The actual number of poles depends on both the stator and the rotor and is equal to the number of capacitance variation cycles (of one phase) per one revolution of the rotor. For example, the simple VCM of Figure 2.1 goes through a minimum and a maximum capacitance twice in each revolution of the rotor; therefore, it is a two-pole motor. However, when using the electromechanical equations, e.g. synchronous speed, it acts as a four-pole VRM.

2.1.2. Energy Conversion Cycle

The energy conversion cycle is a graphical way to describe the mechanism of transduction in electric machines and helps to understand the operation of motors and generators. For electrostatic machines, the energy conversion cycle is defined in charge-voltage (*q*-*v*) plane, which represents the characteristic space of capacitors. The electrical energy exchange between a system characterized in a *q*-*v* plane and the outside world is defined by:

$$E = \int_{Q_1}^{Q_2} v dq \tag{2.1}$$

and the electrical co-energy is defined by:

$$E^* = \int_{V_1}^{V_2} q dv. \tag{2.2}$$

where (Q_1, V_1) and (Q_2, V_2) are initial and final operating points, respectively.

The co-energy does not have a physical meaning and is just a mathematical function that simplifies the integration in case the *q*-*v* characteristic function is in the form of $q=\mathbf{Q}(v)$ instead of $v=\mathbf{V}(q)$. The energy in this case can be calculated as:

$$E = \left(Q_2 V_2 - Q_1 V_1\right) - E^* \tag{2.3}$$

It is important to note that equations (2.1) to (2.3) represent the exchange of the electrical energy with the outside world. The exchange of the mechanical energy can be taken into account by considering the conservation of the total energy.

In simple cases such as linear capacitor, the co-energy method does not simplify the calculations since the energy can be calculated as easily. By convention, we consider the electrical energy is delivered to the system if $E>0$, which is the case when $Q_1<Q_2$. Conversely, the electrical energy is generated by the system if $E<0$,

which is the case when $Q_1>Q_2$. This means that as a result of an energy conversion cycle, if the net electrical energy is positive ($E_{net}>0$), the machine is operating in the motor mode, and if the net electrical energy is negative ($E_{net}<0$), the machine is operating in the generator mode. In case of an ideal (lossless) motor, E_{net} is equal to the net mechanical work done by the machine, and in case of an ideal (lossless) generator, E_{net} is equal to the net mechanical work done on the machine.

Figure 2.2 shows a simplified no-load energy conversion cycle of a VCM operating at the synchronous speed in the steady-state condition. Theoretically, electrostatic machines are limited by the dielectric breakdown. As a result, there is a maximum operating voltage, V_{max}. It is also assumed that the VCM is a linear variable capacitor and its capacitance changes between C_{min} and C_{max}. Therefore, the characteristic space of the VCM is the triangle **ABC**. Another assumption that simplifies the problem is that the time constant of charging and discharging the VCM is much smaller that the period of the excitation voltage (this is valid in most practical cases because the time constant of the VCM is usually in the range of nanoseconds while the period of the voltage is hardly smaller than microseconds). In an ideal no-load operation at the synchronous speed, the excitation voltage and the capacitance variation waveforms are in phase. Assuming a square-wave excitation voltage, the motor follows the **ABCA** cycle, which repeats in each period. As a result of three energy exchanges in the electrical and mechanical domains, the motor does a net mechanical work equal to the area of the triangle **ABC** in each cycle. From point **A** to point **B**, when the rotor is at the minimum capacitance position, the electrical energy

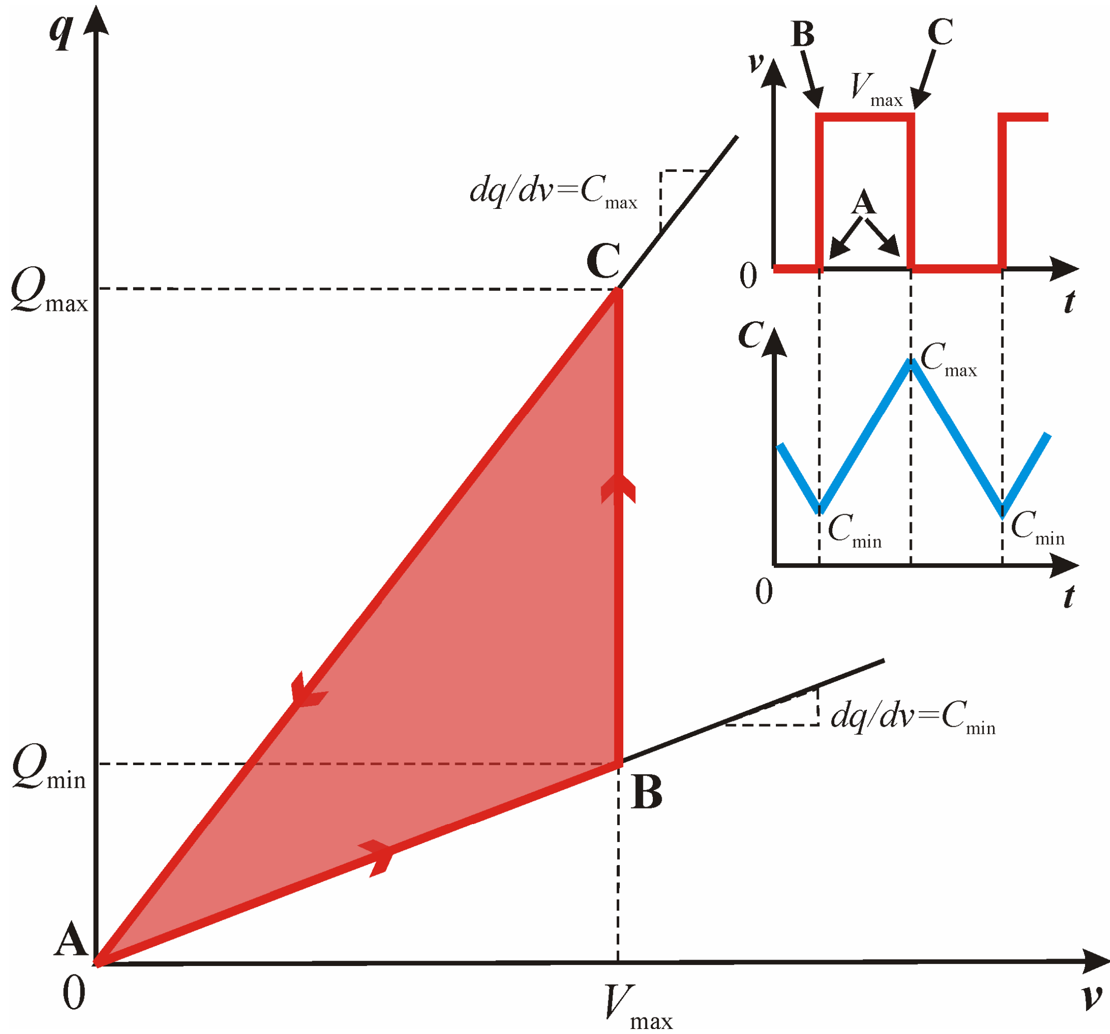

Figure 2.2. The triangle **ABC** is the characteristic space and the path **ABCA** is the no-load energy conversion cycle of a typical VCM. The square-wave excitation voltage and an approximation of the variable capacitance, which are in-phase during the no-load operation, are also shown.

is stored in the VCM. This energy exchange takes place at the leading edge of the excitation voltage square pulse and can be written as:

$$E_{\mathbf{AB}} = \int_0^{Q_{min}} v dq = \frac{1}{2} V_{max} Q_{min} = \frac{1}{2} C_{min} V_{max}^2 . \tag{2.4}$$

From point **B** to point **C**, while the voltage is kept constant, the rotor moves from the minimum to the maximum capacitance position and the energy is exchanged between the electrical and mechanical domains:

$$E_{\mathbf{BC}} = \int_{Q_{\min}}^{Q_{\max}} v dq = V_{\max}\left(Q_{\max} - Q_{\min}\right) = \left(C_{\max} - C_{\min}\right)V_{\max}^{2}. \tag{2.5}$$

And finally, from point **C** back to point **A** the VCM is discharged to zero at the trailing edge of the excitation voltage square pulse. The energy exchange is:

$$E_{\mathbf{CA}} = \int_{Q_{\max}}^{0} v dq = -\frac{1}{2}V_{\max}Q_{\max} = -\frac{1}{2}C_{\max}V_{\max}^{2}. \tag{2.6}$$

Therefore, the net energy exchange can be written as the sum of the energies in equations (2.4), (2.5), and (2.6):

$$E_{\text{net}}^{\max} = E_{\mathbf{AB}} + E_{\mathbf{BC}} + E_{\mathbf{CA}} = \frac{1}{2}V_{\max}\left(Q_{\max} - Q_{\min}\right) = \frac{1}{2}\left(C_{\max} - C_{\min}\right)V_{\max}^{2}. \tag{2.7}$$

The absolute value of the net energy exchange at no-load condition is equal to the area of the triangle **ABC**. Since the sign of the energy is positive, it is equal to the net electrical energy delivered to the VCM (by the excitation source) or the net mechanical work done by the VCM. This is the maximum possible mechanical work that the motor can do in one cycle. As equation (2.7) shows, this maximum mechanical work is limited by the minimum and maximum capacitance difference, and by the dielectric breakdown.

Figure 2.3 shows the energy conversion cycle of a VCM operating at the synchronous speed in the steady-state condition under a certain load. In this case the excitation voltage and the capacitance variation are out of phase. The phase difference is called the *power angle*, which will be discussed in detail later in this chapter. Assuming that the capacitance variation waveform lags behind the excitation waveform, a different cycle, **ADBEA** is followed and repeats in every period (if the capacitance leads the voltage then the **ADCEA** cycle is followed but the final result is the same). Similar to the no-load case, after some energy exchanges, the motor does a

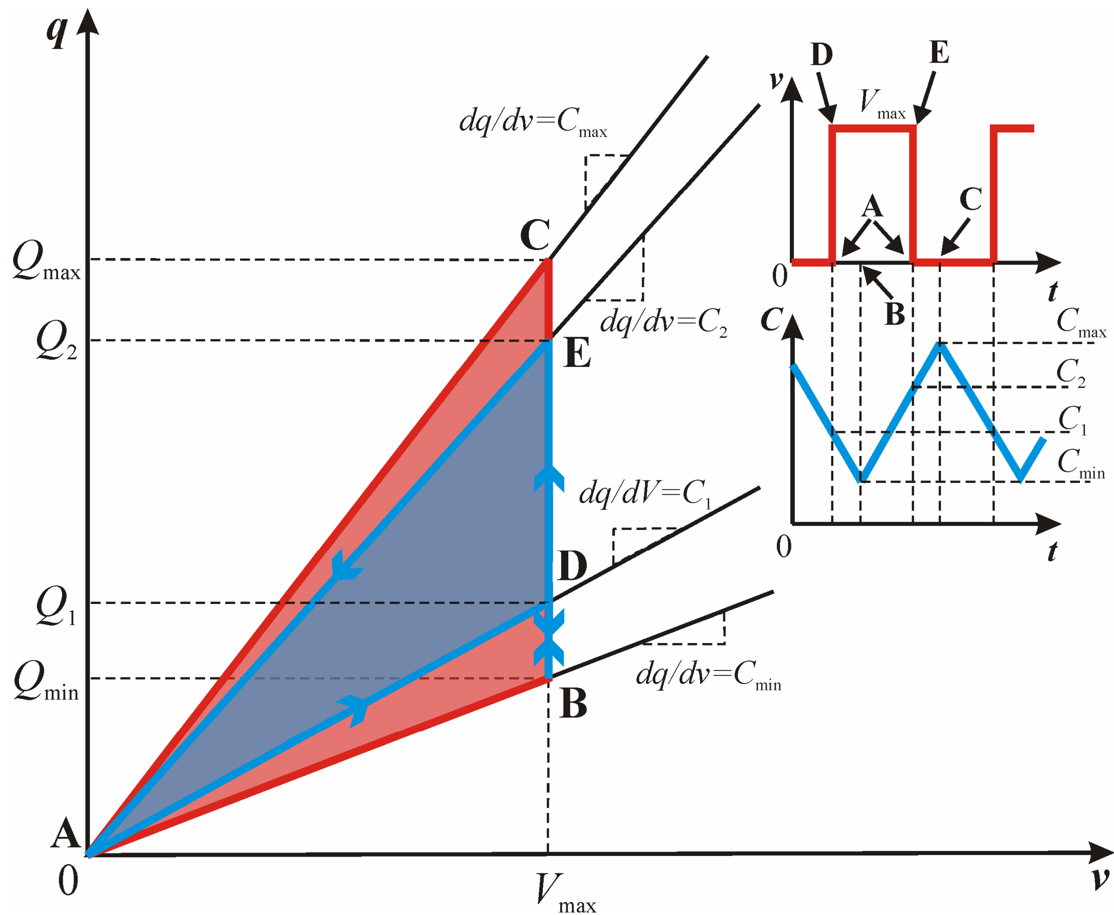

Figure 2.3. The triangle **ABC** is the characteristic space of a typical VCM. The path **ADBEA** is the energy conversion cycle of the VCM when under load. The square-wave excitation voltage and a linear approximation of the variable capacitance, which are out of phase during the load operation, are also shown.

net mechanical work, which is equal to the area of the triangle **ADE**. As expected, this is smaller than the no-load output work (the area of the triangle **ABC**). It will be shown later that the absolute value of the power angle has to be smaller than 90° so that the machine operates in the motor mode. In case of a non-zero power angle, contrary to the no-load case, the starting point of each cycle is different from the minimum capacitance position of the rotor. This corresponds to the leading edge of the excitation voltage square pulse and the path from point **A** to point **D**. The exchanged energy during this segment of the cycle is stored in the VCM:

$$E_{\mathbf{AD}} = \int_0^{Q_1} v dq = \frac{1}{2} V_{\max} Q_1 = \frac{1}{2} C_1 V_{\max}^2. \tag{2.8}$$

From point **D** to point **B**, while the voltage is kept constant, the rotor moves toward the minimum capacitance position. The energy is exchanged between the electrical and mechanical domains:

$$E_{\mathbf{DB}} = \int_{Q_1}^{Q_{\min}} v dq = V_{\max}\left(Q_{\min} - Q_1\right) = \left(C_{\min} - C_1\right) V_{\max}^2. \tag{2.9}$$

$E_{\mathbf{DB}}$ is clearly negative, which means that the electrical energy is generated in this segment of the cycle. In other words, the VCM acts as a generator here. From point **B** to point **E**, while the voltage is still kept constant, the rotor moves from the minimum toward the maximum capacitance position but before reaching there the voltage square pulse is switched off. In this segment the energy is exchanged between the electrical and mechanical domains:

$$E_{\mathbf{BE}} = \int_{Q_{\min}}^{Q_2} v dq = V_{\max}\left(Q_2 - Q_{\min}\right) = \left(C_2 - C_{\min}\right) V_{\max}^2. \tag{2.10}$$

And finally, from point **E** back to point **A** the VCM is discharged to zero at the trailing edge of the excitation voltage square pulse. The energy exchange is:

$$E_{\mathbf{EA}} = \int_{Q_2}^{0} v dq = -\frac{1}{2} V_{\max} Q_2 = -\frac{1}{2} C_2 V_{\max}^2. \tag{2.11}$$

Therefore, the net energy exchange can be written as the sum of the energies in equations (2.8), (2.9), (2.10), and (2.11):

$$E_{\text{net}} = E_{\mathbf{AD}} + E_{\mathbf{DB}} + E_{\mathbf{BE}} + E_{\mathbf{EA}} = \frac{1}{2} V_{\max}\left(Q_2 - Q_1\right) = \frac{1}{2}\left(C_2 - C_1\right) V_{\max}^2. \tag{2.12}$$

The absolute value of the net energy exchange is equal to the area of the triangle **ADE**. Since the sign of the energy is positive, it is equal to the net electrical energy

delivered to the VCM (by the excitation source) or the net mechanical work done by the VCM.

2.2. Variable-Capacitance Machines in Generator Mode

2.2.1. Principle of Operation

When a variable-capacitance machine operates in the generator mode, the energy flows from the mechanical to the electrical domain. The mechanical energy is supplied by physically moving the rotor, causing a change in the rotor position, and therefore, a change in the machine capacitance. In order to have a variable-capacitance generator (VCG) generate electrical energy, there has to be an initial amount of energy stored in the capacitance and the capacitance has to decrease with the rotor motion while the stator is active. The initial energy can be accomplished by charging and discharging the generator capacitance to a small initial charge (or voltage) at a certain frequency and to ensure the decrease in the capacitance takes place at the right moment, the rotor motion must be synchronized with the stator excitation frequency. By keeping the charge (or the voltage) constant while the capacitance decreases, the voltage (or the charge) changes so that the mechanical work will be converted to the electrical energy. Since there are two independent variables, charge and voltage, there are two ways to control the energy conversion in a VCG: charge-controlled and voltage-controlled. In a charge-controlled VCG, the charge is kept constant during the energy exchange between electrical and mechanical domains, while in a voltage-controlled VCG, the voltage is kept constant. Generally, charge-controlled VCGs are more practical (because they do not need a high-voltage source to start the conversion), however, voltage-controlled VCGs can provide more

output energy. There are schemes to combine the two methods to take advantage of both [108]. Since our focus here is mainly on motors, only the charge-controlled VCG will be reviewed in more details in the next subsection.

2.2.2. Energy Conversion Cycle

Figure 2.4 shows a simplified no-load energy conversion cycle of a charge-controlled VCG operating at the synchronous speed in the steady-state condition. With assumptions similar to those of a VCM, The triangle **ABC** is the characteristic space of the VCG. In an ideal no-load operation at the synchronous speed, the voltage and the capacitance variation waveforms are in phase and the generator follows the **ABCA** cycle, which repeats in each period. As a result of three energy exchanges in the electrical and mechanical domains, the generator generates a net electrical energy equal to the area of the triangle **ABC** in each cycle.

From point **A** to point **B**, when the rotor is at the maximum capacitance position, an initial electrical energy is stored in the VCG by connecting a charge reservoir (or a voltage source). This energy exchange takes place at the leading edge of the voltage pulse and can be written as:

$$E_{\mathbf{AB}} = \int_0^{Q_{\max}} v dq = \frac{1}{2} V_{\min} Q_{\max} = \frac{1}{2} C_{\max} V_{\min}^2 . \qquad (2.13)$$

At point **B**, the voltage source is disconnected, and therefore, the charge on the VCG remains constant until the voltage source is reconnected at point **C**. From point **B** to point **C**, while the charge is constant, a mechanical work is done on the rotor, moving it from the maximum to the minimum capacitance position. Since the VCG is disconnected from the source, no electrical energy exchange takes place:

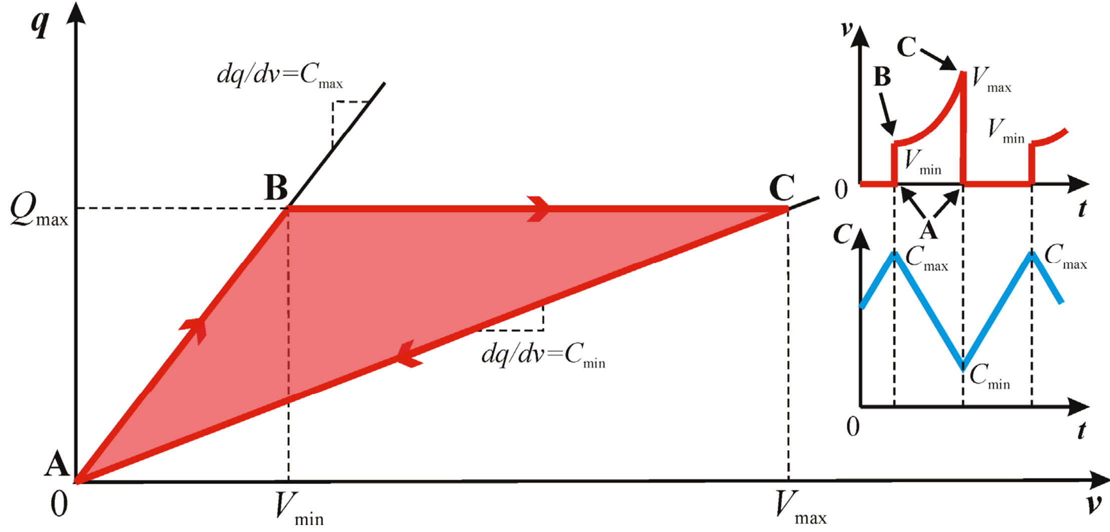

Figure 2.4. The triangle **ABC** is the characteristic space and the path **ABCA** is the no-load energy conversion cycle of a typical charge-controlled VCG. The output voltage and a linear approximation of the variable capacitance, which are in-phase during the no-load operation, are also shown.

$$E_{\mathbf{BC}} = \int_{Q_{max}}^{Q_{max}} v dq = 0. \tag{2.14}$$

This means that the mechanical work done on the rotor has been converted to the electrical energy.

And finally, from point **C** back to point **A** the VCG is discharged to zero at the trailing edge of the voltage pulse. The electrical energy exchange is:

$$E_{\mathbf{CA}} = \int_{Q_{max}}^{0} v dq = -\frac{1}{2} V_{max} Q_{max} = -\frac{1}{2} \frac{C_{max}^2}{C_{min}} V_{min}^2. \tag{2.15}$$

Therefore, the net energy exchange can be written as the sum of the energies in equations (2.13), (2.14), and (2.15):

$$\begin{aligned} E_{net}^{max} = E_{\mathbf{AB}} + E_{\mathbf{BC}} + E_{\mathbf{CA}} &= -\frac{1}{2} Q_{max} \left(V_{max} - V_{min} \right) \\ &= -\frac{1}{2} \frac{C_{max}}{C_{min}} \left(C_{max} - C_{min} \right) V_{min}^2. \end{aligned} \tag{2.16}$$

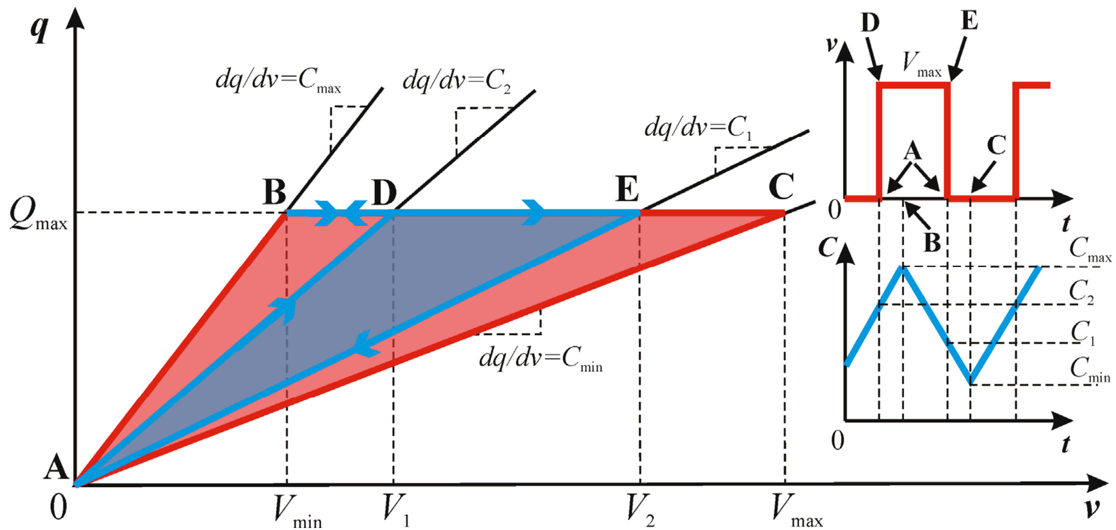

Figure 2.5. The triangle **ABC** is the characteristic space of a typical VCG. The path **ADBEA** is the energy conversion cycle of the VCG when under load. The square-wave output voltage and a linear approximation of the variable capacitance, which are out of phase during the load operation, are also shown.

The absolute value of the net energy exchange at no-load condition is equal to the area of the triangle **ABC**. Since the sign of the energy is negative, it is equal to the net electrical energy generated by the VCG and is also equal to the net mechanical work done on the VCG. This is the maximum possible electrical energy that the generator can generate in one cycle and is limited not only by the minimum and maximum capacitance difference but also the ratio. It is also limited by the initial voltage source used to jump start the generator.

Similar to the VCM, a VCG operating under load has a non-zero power angle and goes through an energy conversion cycle different than the no-load operation. This situation is shown in Figure 2.5. As in the VCM case, the capacitance can lag behind or lead the voltage, but the absolute value of the power angle has to be larger than 90° so that the machine operates in the generator mode. With similar

calculations, it can be shown that the net electrical energy generated by the VCG is equal to the area of the triangle **ADE** in Figure 2.5:

$$
\begin{aligned}
E_{\text{net}} = E_{\mathbf{AD}} + E_{\mathbf{DB}} + E_{\mathbf{BE}} + E_{\mathbf{EA}} = -\frac{1}{2}Q_{\max}\left(V_2 - V_1\right) &= -\frac{1}{2}\left(\frac{1}{C_1} - \frac{1}{C_2}\right)Q_{\max}^2 \\
&= -\frac{1}{2}\frac{C_{\max}^2}{C_1 C_2}\left(C_2 - C_1\right)V_{\min}^2 .
\end{aligned}
\tag{2.17}
$$

2.3. Electromechanical Characteristics of Variable-Capacitance Machines

As mentioned before, the capacitance of a VCM is a function of the position of the rotor. In general, a variable capacitance can be modeled as a multiport transducer that interfaces the electrical and mechanical energy domains. Figure 2.6 shows this concept for the general case of a variable capacitor with three degrees of freedom for the moving electrode. The capacitor has one port in the electrical energy domain, and three ports in the mechanical energy domain, representing Cartesian coordinates x, y, and z. The choice of the coordinate system usually depends on the shape of the capacitor, e.g. for a rotary VCM a cylindrical coordinate system is easier to use while for a linear VCM a Cartesian coordinate system is the best choice. It should also be mentioned that each port represents a pair of dependent variables, which are independent from other pairs in the domain.

In order to analyze a multiport variable capacitor, we can use energy or co-energy equations to calculate other variables in electrical or mechanical domain. In Figure 2.6, the change in the total energy can be written in terms of the sum of changes in all energy domains:

$$dW_t = VdQ + F_X dx + F_Y dy + F_Z dz \tag{2.18}$$

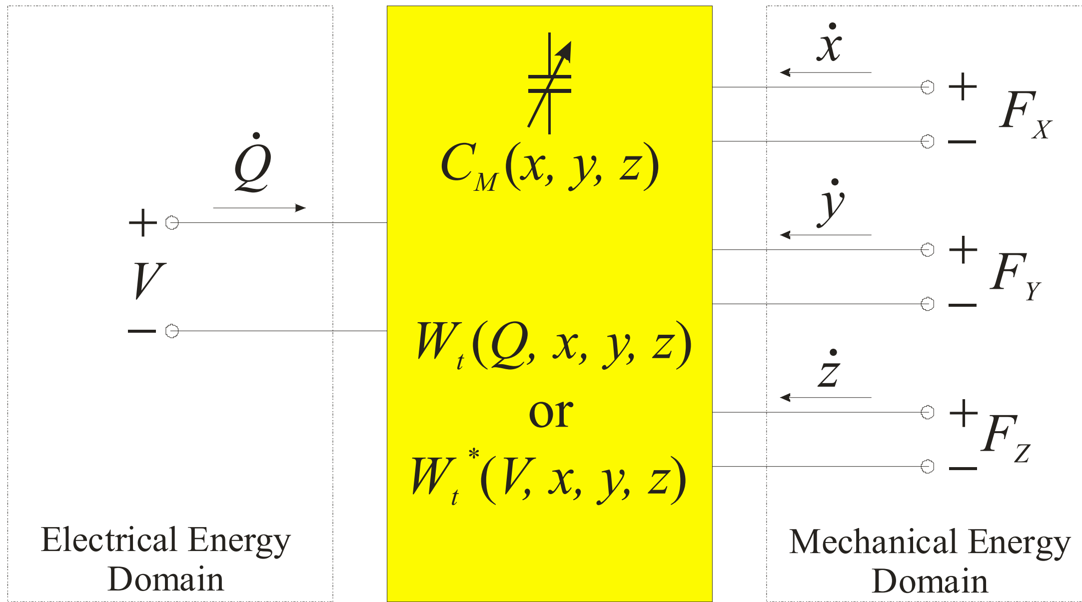

Figure 2.6. Multiport variable capacitor as an energy conversion element between electrical and mechanical energy domains. The capacitor translates electrical entities (voltage and current) to mechanical entities (force and velocity) generally in three independent directions, and vice versa. The conversion function can be energy (W_t) or co-energy (W_t^*) depending on the mode of operation (charge control or voltage control). Note that a "dot" represents the time derivative.

where W_t is the total energy, V is the voltage and Q is the charge of the capacitor, F_X, F_Y, and F_Z are the force components applied to the capacitor electrodes, and x, y, and z are the position of the capacitor moving electrode. Now since the co-energy (W_t^*) is:

$$W_t^* = QV - W_t \tag{2.19}$$

the change in the total co-energy can be written as:

$$dW_t^* = d\left(VQ\right) - dW_t \tag{2.20}$$

and by replacing dW_t from equation (2.18), we will have:

$$dW_t^* = QdV - F_x dx - F_y dy - F_z dz \tag{2.21}$$

2.3.1. Force and Power

In the charge-controlled mode, the voltage across a variable capacitor is calculated by keeping the moving electrode fixed in equation (2.18):

$$V = \left. \frac{\partial W_t(Q,x,y,z)}{\partial Q} \right|_{x,y,z} \tag{2.22}$$

and the force applied to the electrodes is calculated by keeping the capacitor charge fixed:

$$\vec{F} = \vec{\nabla} W_t(Q,x,y,z)\Big|_Q \tag{2.23}$$

The instantaneous mechanical power (P_m) can then be calculated by:

$$P_m = \vec{F}.\vec{u} = F_X \dot{x} + F_Y \dot{y} + F_Z \dot{z} \tag{2.24}$$

where u is the velocity of the capacitor moving electrode. Substituting equation (2.23) in equation (2.24), we will have:

$$P_m = \frac{\partial W_t}{\partial x}\dot{x} + \frac{\partial W_t}{\partial y}\dot{y} + \frac{\partial W_t}{\partial z}\dot{z} \tag{2.25}$$

For a variable capacitor (C_M) with a linear Q-V characteristic in charge control mode, the energy can be written as:

$$W_t = \frac{1}{2}\frac{Q^2}{C_M} \tag{2.26}$$

and substituting equation (2.26) in equations (2.22), (2.23), and (2.25) yields:

$$V = \frac{Q}{C_M} \tag{2.27}$$

$$\vec{F} = -\frac{1}{2}\frac{Q^2}{C_M^2}\vec{\nabla} C_M \tag{2.28}$$

$$P_m = -\frac{1}{2}\frac{Q^2}{C_M^2}\left(\frac{\partial C_M}{\partial x}\dot{x} + \frac{\partial C_M}{\partial y}\dot{y} + \frac{\partial C_M}{\partial z}\dot{z}\right) = -\frac{1}{2}\frac{Q^2}{C_M^2}\frac{\partial C_M}{\partial t} \tag{2.29}$$

Equations similar to equations (2.22) and (2.23) can be derived for the voltage-controlled mode from equation (2.21):

$$Q = \left.\frac{\partial W_t^*\left(V, x, y, z\right)}{\partial V}\right|_{x,y,z} \tag{2.30}$$

$$\vec{F} = -\vec{\nabla} W_t^*\left(V, x, y, z\right)\Big|_V \tag{2.31}$$

and for a linear capacitor in voltage control mode, the co-energy can be written as:

$$W_t^* = \frac{1}{2}V^2 C_M \tag{2.32}$$

and substituting equation (2.32) in equations (2.30), (2.31), and (2.25) yields:

$$Q = VC_M \tag{2.33}$$

$$\vec{F} = -\frac{1}{2}V^2\vec{\nabla}C_M \tag{2.34}$$

$$P_m = -\frac{1}{2}V^2\left(\frac{\partial C_M}{\partial x}\dot{x} + \frac{\partial C_M}{\partial y}\dot{y} + \frac{\partial C_M}{\partial z}\dot{z}\right) = -\frac{1}{2}V^2\frac{\partial C_M}{\partial t} \tag{2.35}$$

Note that the above equations are generally valid for both motor and generator operation of a variable-capacitance machine. By convention shown in Figure 2.6, energy (or power) delivered to the capacitor from each domain is positive. Therefore, a negative energy (or power) means that it is produced (or delivered to the domains from the capacitor). Considering equations (2.28), (2.29), (2.34), and (2.35), this means that the machine operates as a motor when the rate of change of machine capacitance is positive and as a generator when the spatial gradient or the rate of change of machine capacitance is negative. In a VCM the rotor has the freedom to

move in only one direction, e.g. in x direction in a linear VCM and in ϕ direction in a rotary VCM. Therefore, when the rotor moves, the capacitance of VCM (in any phase) varies between a maximum (poles and electrodes are fully aligned) and a minimum (poles and electrodes are fully misaligned). The VCM operates as a motor if the excitation voltage is applied to the stator when the capacitance changes from minimum to maximum. The VCM operates as a generator if the excitation voltage is applied to the stator when the capacitance changes from maximum to minimum.

2.3.2. Mechanical Speed and Synchronous Operation

The output power and force (torque) of the motor depends on the time-dependent excitation voltage and the spatial gradient of the position-dependent capacitance as stated in equations (2.28), (2.29), (2.34), and (2.35). For most practical purposes, we can assume that voltage and capacitance are periodic functions of time and position, respectively. Therefore, we can expand the voltage and the capacitance into Fourier series (shown for the rotary VCM):

$$V(t) = V_0 + \sum_{n=1}^{\infty} V_n \cos(n\omega_s t - \alpha_n) \tag{2.36}$$

$$C_M(\phi) = C_0 + \sum_{n=1}^{\infty} C_n \cos(nN\phi - \beta_n) \tag{2.37}$$

where ω_s is the angular frequency of the excitation voltage and ϕ is the angular position of the rotor. N is the number of cycles of the capacitance variations per one revolution of the rotor and is also equal to the actual number of poles. V_0, V_n, and α_n are the average, the nth harmonic amplitude, and the nth harmonic phase of the

excitation voltage, respectively. C_0, C_n, and β_n are the average, the nth harmonic amplitude, and the nth harmonic phase of the capacitance, respectively.

Assuming that the VCM is operating in the steady-state condition and the rotor angular speed is constant, we can write:

$$N\phi = h\omega_s t - \delta \tag{2.38}$$

$$\phi = h\frac{\omega_s}{N}t - \delta \tag{2.39}$$

where h and δ are constants. δ is the phase difference between the capacitance variations and the excitation voltage waveforms, and is called the *power angle*. The angular speed of the rotor can then be written as:

$$\omega_m = h\frac{\omega_s}{N} \tag{2.40}$$

It has been shown in [36] that the instantaneous mechanical power of the VCM, calculated from equation (2.35), is sum of terms such as:

$$\cos\left(k\omega_s t - \gamma_k\right)\cos\left(l\omega_s t - \eta_l\right)\sin\left(qh\omega_s t - \lambda_q\right)$$

where k, l, and q are integers ($q \neq 0$). The VCM generates a non-zero average mechanical power if:

$$h = \pm\frac{k \pm l}{q} \tag{2.41}$$

The VCM is running at *synchronous speed* when h=1 or $\omega_m = \omega_s / N$. Rewriting the synchronous speed in revolutions per minute (n_r) and in terms of the frequency of the excitation voltage (f_s), we have:

$$n_r = 60\frac{f_s}{N} \tag{2.42}$$

and considering the discussion on the number of poles (N_p) in section 2.11, we can assume that N_p=2N and we get the famous equation for synchronous speed, also used in magnetic machines:

$$n_r = 120\frac{f_s}{N_p} \tag{2.42}$$

In case of the simple sinusoidal excitation, the average power is a function of the amplitude and frequency of the excitation voltage, the VCM capacitance, and the power angle (δ). In order to demonstrate how the average power changes with power angle, we consider the simple case of sinusoidal excitation voltage (first harmonic) and approximate the capacitance with a sine-squared function having a minimum capacitance of $C_{\min}$ and a maximum capacitance of $C_{\max}$:

$$V(t) = V_1 \sin(\omega_s t + \delta) \tag{2.43}$$

$$C_M(\phi) = C_{\min} + \frac{1}{2}(C_{\min} + C_{\max})\sin^2(N\phi) \tag{2.44}$$

Assuming the VCM is running with synchronous speed, it can be shown [39] that by integrating the instantaneous power calculated from equation (2.35), the average mechanical power can be written as:

$$\overline{P}_m = \frac{\omega_s}{2\pi}\int_0^{2\pi/\omega_s} P_m = -\frac{1}{8}V_1^2(C_{\max} + C_{\min})\omega_s \sin(2\delta) \tag{2.45}$$

Figure 2.7 shows a plot of the average power as a function of the power angle. As mentioned before, a positive power indicates the generator mode and a negative power indicates the motor mode. This means that for a power angle in the range of $0<\delta<\pi/2$ (the voltage leads the capacitance), the VCM operates as a motor and for a power angle in the range of $\pi/2<\delta<\pi$ (the voltage lags the capacitance), the VCM

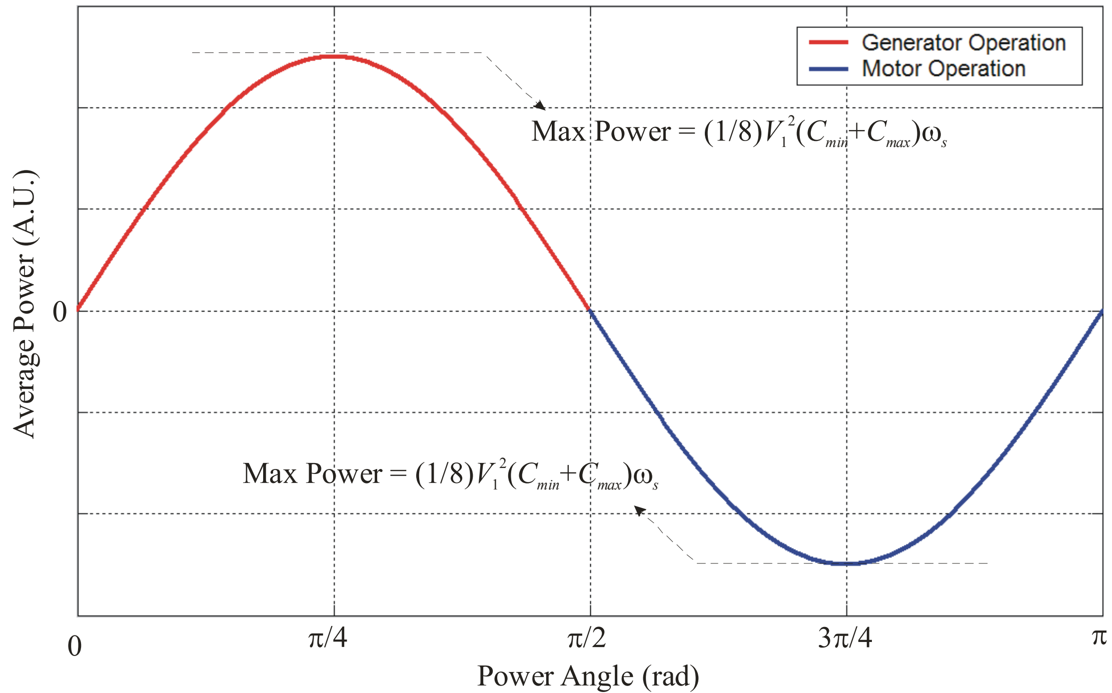

Figure 2.7. The average power of a VCM as a function of the power angle.

operates as a generator. The power angle of the VCM depends on the load imposed on the machine. The VCM adjust its power angle when the load changes so that the speed remains constant (at synchronous speed).

Figure 2.8 shows the excitation voltage, the VCM capacitance, and the instantaneous power as a function of time for two different power angles. As mentioned before and shown in the graphs, a power angle between 0 and $\pi/2$ leads to the motor action and a power angle between $\pi/2$ and π leads to the generator action.

2.4. Electromechanical Modeling using Lumped-Circuit Elements

An electromechanical model based on equations in section 2.3.1 and lumped-circuit elements associated with different components of the VCM has been developed that allows us to predict the dynamic behavior of the device, e.g. transient

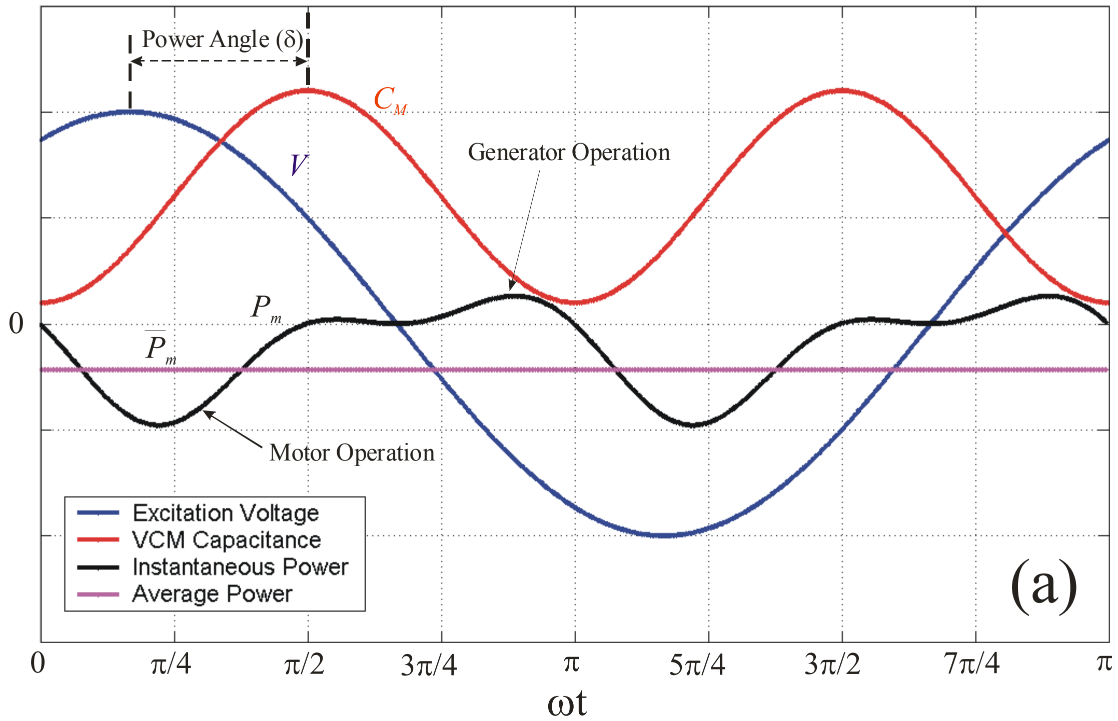

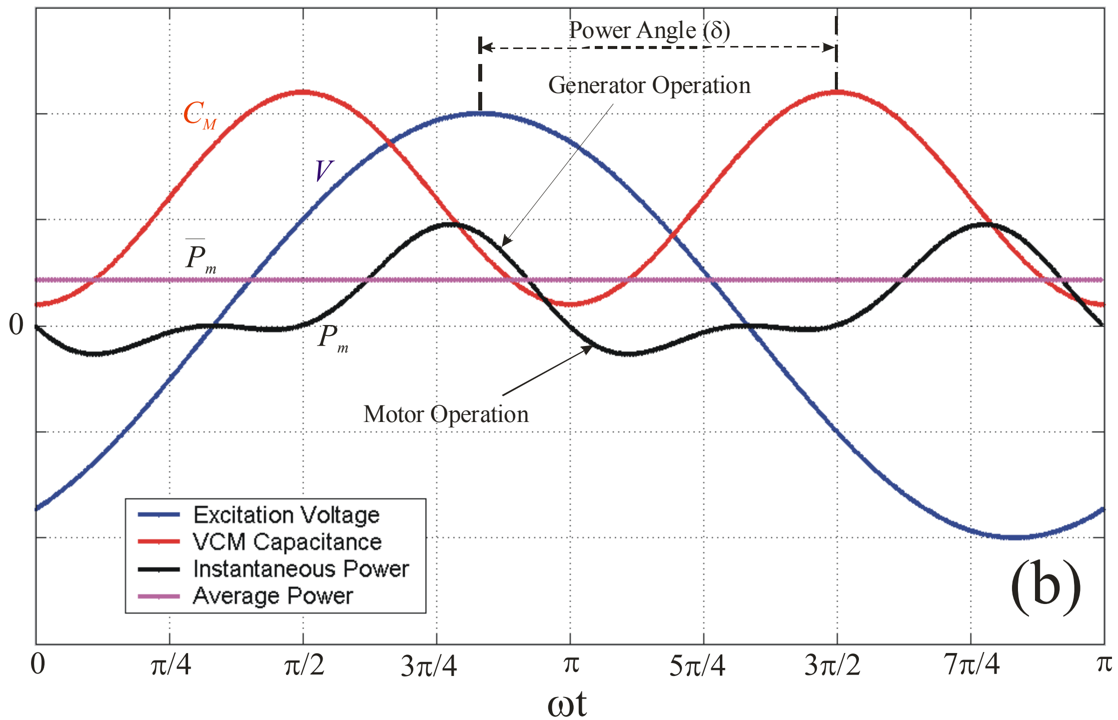

Figure 2.8. Instantaneous and average power of a VCM. In (a) the voltage leads the capacitance ($0 < \delta < \pi/2$) and the average power is negative. The net operation of the VCM is in motor mode. In (b) the voltage lags the capacitance ($\pi/2 < \delta < \pi$) and the average power is positive. The net operation of the VCM is in generator mode.

step response. Since the VCM is driven by a voltage source rather than current source, we will use the equations of the voltage control mode.

Figure 2.9 shows the cross section of a VCM together with the machine capacitance and parasitic elements (only one rotor pole and one active stator electrodes are shown). Two inactive adjacent stator electrodes are also considered for completeness of the model. The bulk of the stator and rotor substrates are assumed to be at ground potential, however, there are resistive paths between the substrate surfaces and the bulk representing by R_S and R_R, respectively. The resistance of the stator electrodes including interconnects are modeled by R_E and the leakage through the dielectric layers (a second layer on top is not shown) are represented by R_L. In addition to the motor capacitance C_M, there are parasitic capacitances between any two conducting components that are at different potentials, i.e. between the electrode and substrate (C_S), and between adjacent electrodes (C_E) on the stator.

Figure 2.10 shows an equivalent circuit for a six-phase linear VCM based on the concept of multiport variable capacitor of Figure 2.6 and lumped-circuit-element model of Figure 2.10. The electrical energy domain includes one port of the variable capacitors and circuit elements associated with the electrical components of the VCM. We assume that the rotor is free to move in x direction, which is the desired linear motion (for a rotary VCM, the rotor is free to move in ϕ direction). Although the motion of the rotor is restricted in y and z directions by a support mechanism (such as bearings), there are rotor vibrations in y and z directions due to the normal force and lateral aligning force in combination with any non-uniformity in the gap, compliance of the silicon substrate, and compliance of the bearings. Therefore, the

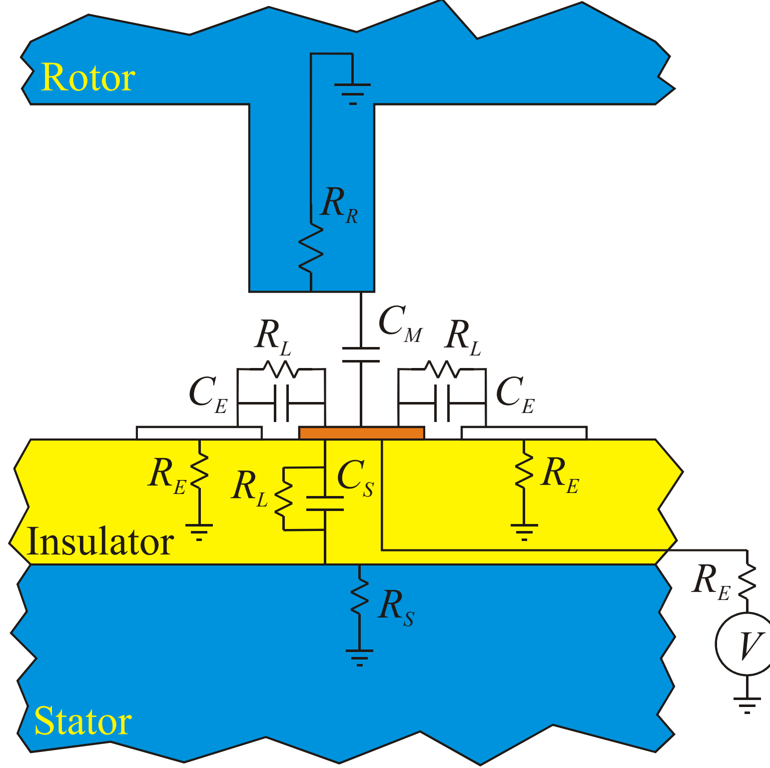

Figure 2.9. Cross section of an active pole/electrode pair in a VCM showing the lumped-circuit elements associated with the components of the device. C_M is a variable capacitor formed between the rotor pole and the stator active electrode. All other elements are parasitic capacitances and resistances.

mechanical energy domain includes three ports of the variable capacitor representing the linear motion in x direction and vibration in y and z directions, and circuit elements associated with the mechanical components of the VCM. The aligning and normal forces in Figure 2.10 can be written according to equation (2.34) as follows (note the change in the sign since direction of velocities is different in Figure 2.10 compared to Figure 2.6):

$$F_X = \frac{\partial W_t^*}{\partial x} = \sum_{i=1}^{6} \frac{1}{2} V_i^2 \frac{\partial C_M}{\partial x} \tag{2.46}$$

$$F_Y = \frac{\partial W_t^*}{\partial x} = \sum_{i=1}^{6} \frac{1}{2} V_i^2 \frac{\partial C_M}{\partial y} \tag{2.47}$$

$$F_Z = \frac{\partial W_t^*}{\partial z} = \sum_{i=1}^{6} \frac{1}{2} V_i^2 \frac{\partial C_M}{\partial z} \tag{2.48}$$

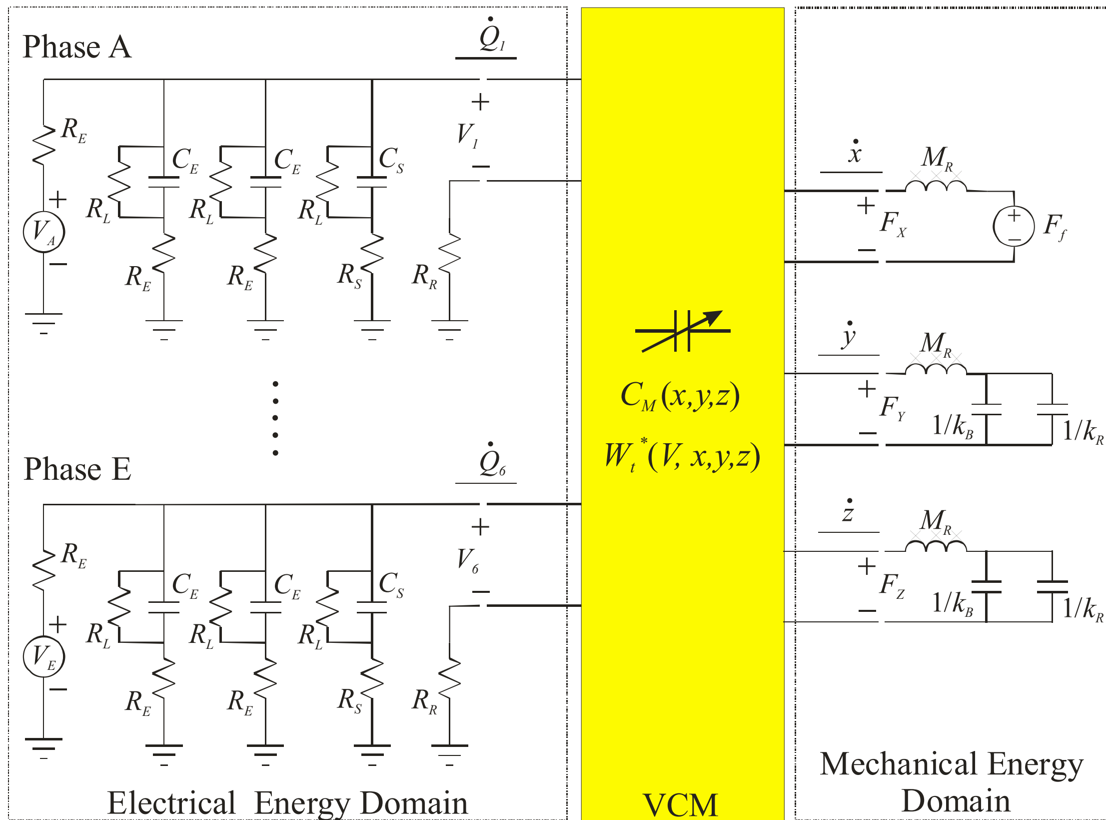

Figure 2.10. An electromechanical model for a six-phase linear VCM. The multiport variable capacitor translates voltage/current of the phases in the electrical energy domain to force/velocity of in x, y, and z directions in the mechanical energy domain. The elements in the electrical energy domain are those shown in Figure 2.9. In the mechanical energy domain, M_R is the rotor mass, and k_R and k_B are the spring constants of the rotor substrate and the bearings, respectively. F_f is the friction force applied to the rotor and is a function of the normal force (F_Z) and the mass of the rotor.

where V_i (for i=1, …, 6) are phase excitation voltages, V_A, …, V_E. The friction force applied to the rotor is the result of interaction between contacting surfaces in the support mechanism. In case of microball bearings, these surfaces are micromachined silicon surfaces on the stator and rotor, and the microball surfaces. We assume that the static friction force (when rotor is still) consists of two components: a component due to stiction (F_0) and a component proportional to the total normal load (F_N). The dynamic friction force (when the rotor is moving) is assumed to be only proportional

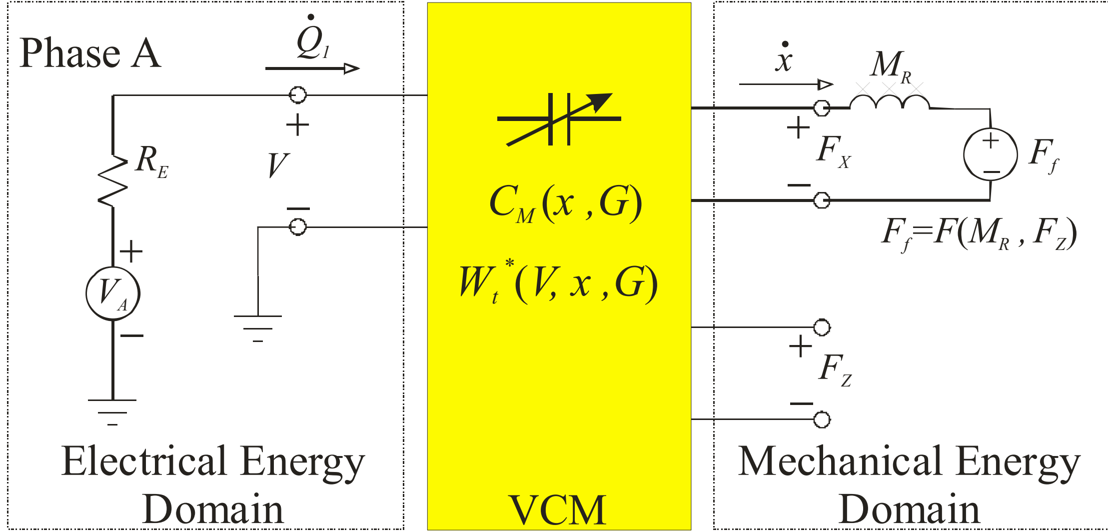

Figure 2.11. A simplified electromechanical model for a single-phase, single-pole VCM.

to the total normal load. The proportionality factors are static (μ_s) and dynamic (μ_d) coefficients of friction (COF), respectively. An accurate model for the rolling friction of microball bearing that takes into account the non-linear dependency of friction on velocity has been developed in [109]. Based on the simple model described above, the friction force can be written as:

$$F_f = \begin{cases} F_0 + \mu_s F_N = F_0 + \mu_s \left(F_{-Z} + M_R g\right) = F_0 + \mu_s \left(-\dfrac{1}{2}\sum_{i=1}^{6} V_i^2 \dfrac{\partial C_M}{\partial z} + M_R g\right) & , \ \dot{x} = 0 \\ \mu_d F_N = \mu_d \left(F_{-Z} + M_R g\right) = \mu_d \left(-\dfrac{1}{2}\sum_{i=1}^{6} V_i^2 \dfrac{\partial C_M}{\partial z} + M_R g\right) & , \ \dot{x} \neq 0 \end{cases} \tag{2.49}$$

where g is the gravity.

The transient and steady-state response of a VCM can be calculated by solving the state equations written for the model of Figure 2.10. As a simple example and to show the methodology, we analyzed the step response of a single-phase, single-pole VCM. We also simplified the model of Figure 2.10 to that shown in Figure 2.11. This reduces the number of state variables to three. We can follow a

similar approach in case of multi-phase, multi-pole VCMs, however, the number of state variables is quite high and the solution to the problem becomes computationally intensive. Considering the simplified model of Figure 2.11, we assume the following state variables:

$$\begin{aligned} X_1 &= V \quad \text{(Voltage)} \\ X_2 &= x \quad \text{(Position)} \\ X_3 &= \dot{x} \quad \text{(Velocity)} \end{aligned} \tag{2.50}$$

The state equations for the circuit of Figure 2.11, therefore, can be written as:

$$\dot{X}_1 = \left(-\frac{1}{R_R C_M \left(X_2, G \right)} \right) X_1 + \left(-\frac{1}{C_M \left(X_2, G \right)} \frac{\partial C_M}{\partial X_2} \bigg|_{z=G} \right) X_1 X_3 + \left(\frac{1}{R_R C_M \left(X_2, G \right)} \right) V_A \tag{2.51}$$

$$\dot{X}_2 = X_3 \tag{2.52}$$

$$\dot{X}_3 = \begin{cases} \left(\frac{1}{2M_R} \frac{\partial C_M}{\partial X_2} \bigg|_{z=G} \right) X_1^2 - \frac{F_0}{M_R} - \mu_s \left(g + \frac{1}{2M_R} \frac{\partial C_M}{\partial z} \bigg|_{z=G} X_1^2 \right) & , \ X_3 = 0 \\ \left(\frac{1}{2M_R} \frac{\partial C_M}{\partial X_2} \bigg|_{z=G} \right) X_1^2 - \mu_d \left(g + \frac{1}{2M_R} \frac{\partial C_M}{\partial z} \bigg|_{z=G} X_1^2 \right) & , \ X_3 > 0 \\ \left(\frac{1}{2M_R} \frac{\partial C_M}{\partial X_2} \bigg|_{z=G} \right) X_1^2 + \mu_d \left(g + \frac{1}{2M_R} \frac{\partial C_M}{\partial z} \bigg|_{z=G} X_1^2 \right) & , \ X_3 < 0 \end{cases} \tag{2.53}$$

$$\text{Boundary Conditions:} \quad X_1(0) = 0,\ X_2(0) = x_0,\ X_3(0) = 0 \tag{2.54}$$

A solution to the derived state equations with the given boundary condition is shown in Figure 2.12 for position, velocity, and applied force (aligning, friction, and net force) in the x direction. The parameter values used for the simulation are shown in Table 2.1. The variable capacitor is calculated based on the parallel-plate approximation assuming a zero minimum. However, the simulation is implemented so that simulated capacitance data from any finite-element software can easily be used instead of the parallel-plate approximation. Initially, the rotor pole is at the fully

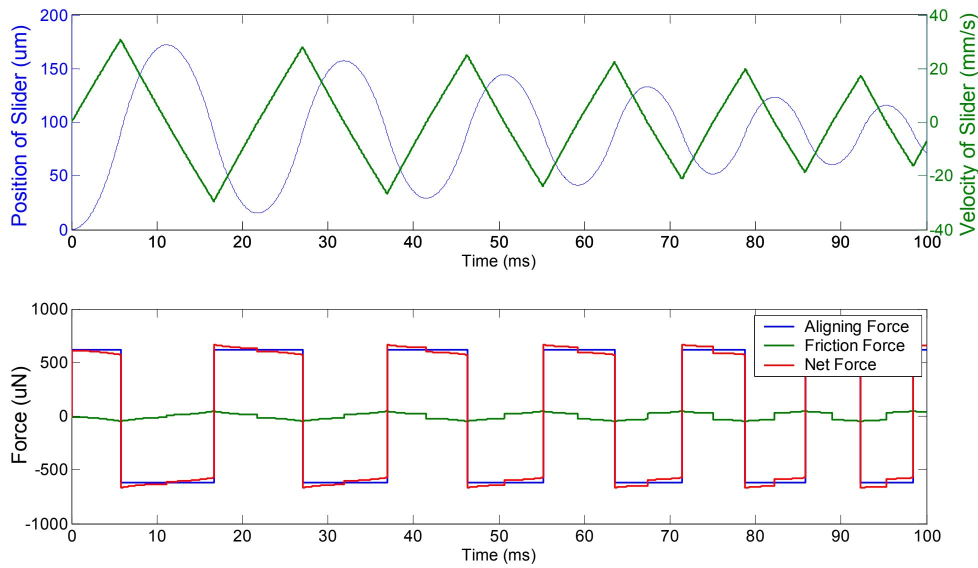

Figure 2.12. Step response of a VCM for rotor position, velocity, and force.

misaligned position and finally, it stops at the fully aligned position if friction is not zero. The existence of friction leads to a damping motion while the motion will be oscillatory in absence of friction. Depending on the amount of friction, the motion of the rotor can be under-damped, critically-damped, or over-damped. In Figure 2.12 the motion is under-damped.

2.5. Polyphase Variable-Capacitance Motors

Similar to magnetic motors, a VCM can operate with a single- or polyphase excitation. Common configurations are single-, two-, three-, and six-phase excitations.

2.5.1. Single-Phase vs. Polyphase

Theoretically, a polyphase VCM can be simply considered as the superposition of several single-phase VCMs. The difference between a single-phase and a polyphase VCM lies in the way that the stator electrodes are excited. The time-

Table 2.1. Parameters Values of the VCM modeled with State Equations (2.51) to (2.54) with the solution shown in Figure 2.12

Parameters	Symbol	Value
Electrode/Pole Width	W	90 μm
Electrode/Pole Length	L	5 mm
Gap	G	10 μm
Rotor Mass	M_R	0.1 g
Static COF	μ_s	0.01
Dynamic COF	μ_d	0.007
Excitation Voltage	V_A	100 V
Electrode Resistance	R_E	2 mΩ

dependent excitation of a single-phase VCM leads to a static potential wave in the air gap of the motor. On the other hand, the excitation of a polyphase VCM is time- and space-dependent, which results in a traveling potential wave.

Although a single-phase VCM is less complicated to fabricate, drive, and control, most VCMs built to date are polyphase motors. There are two main reasons for preference of the polyphase over single-phase (and even two-phase) VCM with first, in order to control the direction of the rotor motion, at least three phases are necessary, and second, with more phases the force/torque coverage of the motor increases, consequently a higher minimum force/torque is achieved. As a result, a smaller ripple will appear in the force/torque, output power, etc.

2.5.2. Three-Phase vs. Six-Phase

A three-phase configuration is the most common excitation in magnetic machines since it is widely available and can easily control the direction of motion, i.e. if the rotor rotates clockwise with an *ABC* phase sequence, it will rotate counter-clockwise with an *ACB* phase sequence. A similar principle can be applied to electrostatic machines. Contrary to the magnetic machines where the poles are activated in pairs leading to a symmetrical distribution of the magnetic flux, the poles

in electrostatic machines are activated individually. This can result in an asymmetrical distribution of the electric field and can lead to a rotor potential above ground in case of a VCM with an electrically-floated rotor. This will decrease the potential difference between stator electrodes and rotor poles and consequently, the force. One way to prevent the asymmetrical distribution of the electric field is to use a six-phase (or more accurately complementary three-phase) configuration where for each phase there is another phase with reversed excitation voltage and as a result the rotor is a virtual ground. Figure 2.13 shows an equivalent circuit (only the capacitors) for a six-phase VCM. The rotor potential is zero due to the symmetry in the six-phase VCM. When phases D, E, and F are excited by voltages with opposite to phases A, B, and C, respectively, the rotor-ground plane is at zero potential, while this is not a valid assumption when D, E, and F are excited by the same voltage as A, B, and C, respectively. The complementary three-phase VCM is the actual dual of a three-phase VRM. By considering the rotor to be a virtual ground, we can assume the six-phase VCM is a system of six conductors and can be represented by the following capacitance matrix:

$$\overline{\mathrm{C}} = \begin{bmatrix} C_{ph} & C_1 & C_2 & C_3 & C_2 & C_1 \\ C_1 & C_{ph} & C_1 & C_2 & C_3 & C_2 \\ C_2 & C_1 & C_{ph} & C_1 & C_2 & C_3 \\ C_3 & C_2 & C_1 & C_{ph} & C_1 & C_2 \\ C_2 & C_3 & C_2 & C_1 & C_{ph} & C_1 \\ C_1 & C_2 & C_3 & C_2 & C_1 & C_{ph} \end{bmatrix} \tag{2.55}$$

where C_{ph} is the self-capacitance of each phase and C_1, C_2, and C_3 are the mutual capacitances. Since the rotor is at zero potential, the energy stored in the system is a function of phase potentials, which is determined by the capacitance matrix. Based on

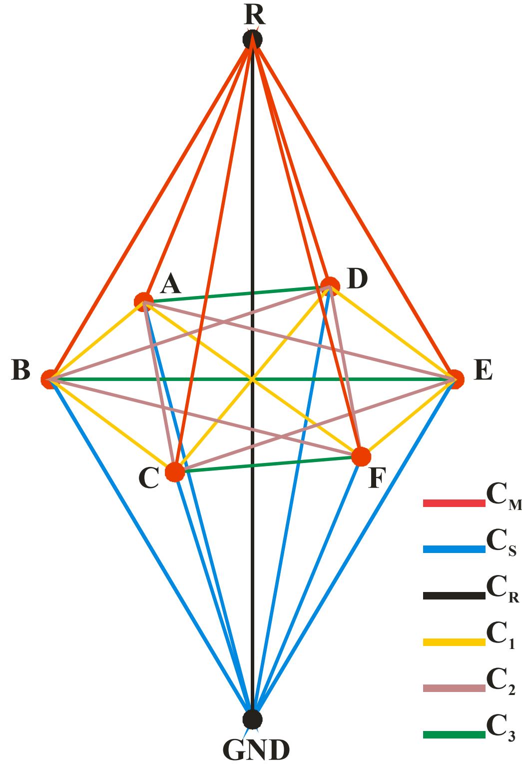

Figure 2.13. An equivalent circuit for a six-phase VCM. If phases D, E, and F are complementary to phases A, B, and C, every point on the rotor ground plane will be at zero potential due to the symmetry.

this and assuming that only the diagonal elements of the capacitance matrix vary with the position of the rotor, a first-order approximation of the aligning force generated by each phase can be written as:

$$F_{ph} = \frac{1}{2} V_{ph}^2 \frac{\partial C_{ph}}{\partial x} \tag{2.56}$$

where V_{ph} is the excitation voltage, C_{ph} is the VCM capacitance per phase, and x is the position of the rotor. For a rotary VCM x is replaced by ϕ.

2.6. Microball Bearing Technology in Silicon

As described in Chapter 1, application of microball bearings in micromachines can improve mechanical stability and robustness of the rotor, provide

Table 2.2. Specifications of the Microball used in our application based on American Ball Manufacturing Association (AMBA) standard

Specification	**Value**
Grade	10
Size Range	284.5 μm
Deviation from Spherical Form	0.254 μm
Lot Diameter Variation	± 0.254 μm
Allowable Ball Gage Variation	± 1.27 μm
Maximum Surface Roughness	25.4 nm
Material	Stainless Steel 440C (16-18 % Cr, 0.95-1.2 % C)

a low-friction motion and define a uniform air gap. Microball bearings consist of two components, microballs that support the rotor and microball housings. The housings are in the form of trenches or grooves etched in the stator and the rotor. Precision microballs (Thomson Precision, Bristol, CT) used in our application are made of stainless steel 440C with a diameter of 285 μm (284.5 μm to be accurate) and a grade of 10 (see Table 2.2 for specifications of grade 10). Microballs as small as 150 μm in diameter and as precise as grade 3 are available off-the-shelf. Microballs made of materials other than stainless steel are also available. The 285 μm diameter microballs are big enough to be handled by a pair of precision tweezers, but still small enough for our application.

The shape, design, and fabrication method of the microball housing depends on the type of the bearing (linear or rotary) and the trade-off between stability and friction. Figure 2.14 shows cross sections of three possible designs for the microball housing: v-groove, anisotropically-etched trench, and isotropically-etched trench. Note that a combination of these is also possible. Ideally, v-groove housing provides the highest stability for the rotor since each microball has two contact points with each v-groove. In case of the linear bearing, trench housing yields the lowest friction

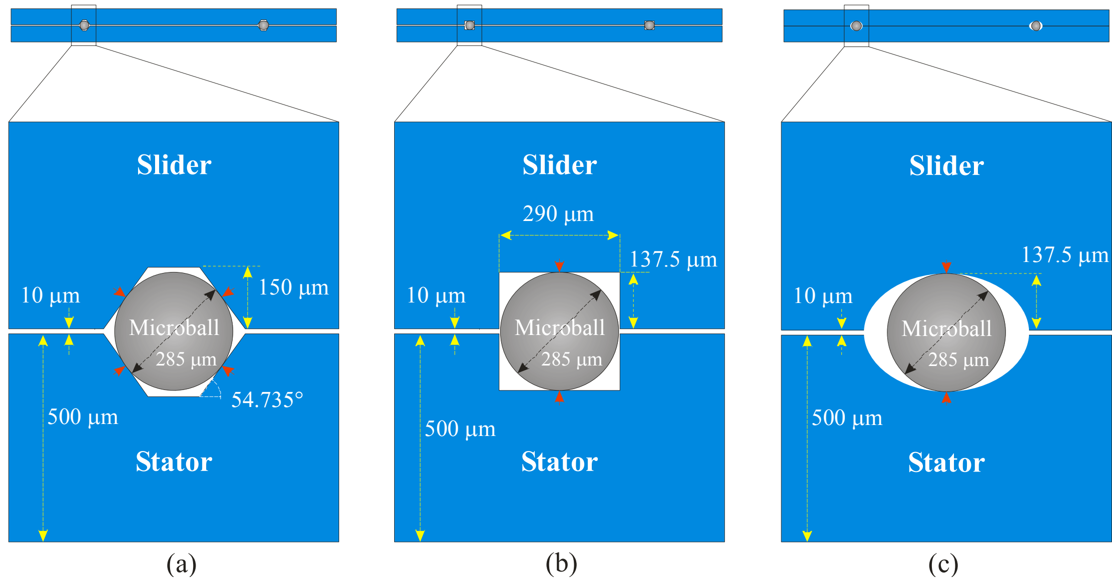

Figure 2.14. Schematic cross-section view of three different designs for linear microball bearings: (a) v-groove design, (b) anisotropically-etched trench design, and isotropically-etched trench design. The v-grooves has a sidewall angle of 54.735°, which is the angle between (100) and (111) crystallographic planes in silicon achieved by anisotropic wet etching. The dimensions are designed to have a 10 µm air gap. The contact points are shown with red arrows. The dimensions are to scale.

since each microball has only one contact points with each trench. In addition, in case of v-grooves, smaller sidewall angle results in lower friction.

The dimensions of the microball housings in Figure 2.14 are calculated to obtain a 10 µm gap between the stator and the rotor (or slider in case of the linear device). The design parameters of microball bearings can be calculated based on simple geometrical equations. For example, in case of all-v-groove microball bearings as shown in Figure 2.15, the following equations can be used to determine unknown parameters:

$$b + \frac{2h}{\tan\theta} = W \tag{2.57}$$

$$G\cos\theta + W\sin\theta = d \tag{2.58}$$

$$G + 2h = d + 2z \tag{2.59}$$

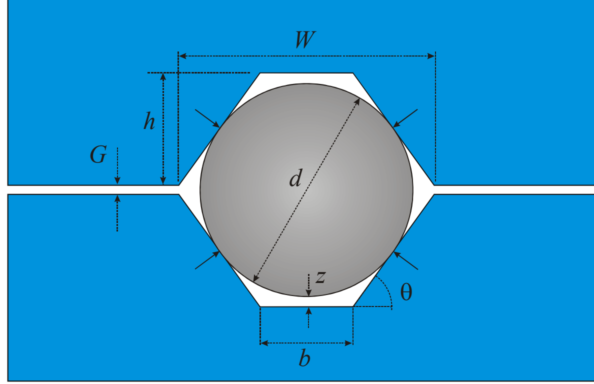

Figure 2.15. Cross-section view of v-groove microball bearings showing geometrical design parameters

where W is the width of the v-groove, h is the depth of the v-groove, b is the width of the v-groove bottom floor, θ is the angle of the v-groove sidewall, G is the air gap, d is the diameter of the microball, and z is the distance between the bottom of the microball and the v-groove bottom floor. It is also important to note that for a given v-groove width and microball diameter the air gap is defined according to equation (2.58) independent of the v-groove depth. However, there is an allowed range for the depth:

$$\frac{W}{2}\tan\theta - \frac{d}{2}\left(\frac{1}{\cos\theta} - 1\right) < h < \frac{W}{2}\tan\theta \tag{2.60}$$

The minimum depth is set at the point where the microball touches the bottom floor (z=0) and the maximum depth is specified assuming that the sidewalls reach to each other (b=0).

Linear microball bearings consist of two parallel v-grooves or trenches on each of the stator and the slider as shown in Figure 2.16. The active area of the linear micromotor is fabricated between the two parallel v-grooves on the stator and the slider. Three different designs for the linear microball bearing were already shown in Figure 2.14. As a trade-off between stability and ease of fabrication, we

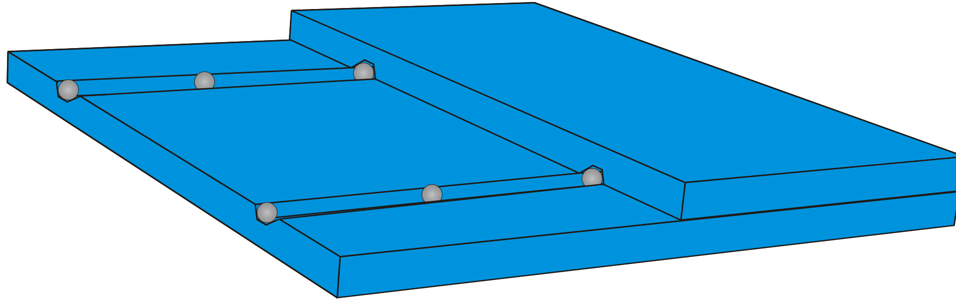

Figure 2.16. Schematic 3D view of linear microball bearings with two parallel v-grooves on stator and slider.

chose the trench design for our B-LVCM. In practice, the width of the trenches has to be slightly larger than the diameter of the microball to compensate for fabrication tolerances. We have designed the trenches to be 5 μm larger than the microballs. This might lead to a wobbling motion and a larger effective friction force.

Another design parameter is the length of the housing that restricts the motion of the microballs. We have considered two different designs: continuous and split trenches. Top views are shown in Figure 2.17. In a continuous trench, the microballs are free to roll along the bearing housing. This design provides the maximum range of motion but it is vulnerable to microball jamming and rotor imbalance. A split trench is a trade-off between microball jamming and range of motion. We used the split trench design on the stator and the continuous trench design on the slider. Fabrication of linear microball bearings is discussed in section 3.5.1.

Rotary microball bearings consist of a circular v-groove or trench on each of the stator and the rotor as shown in Figure 2.18. The active area of the micromachine is fabricated inside the circular trench. Same three designs for linear microball bearings shown in Figure 2.14 can be used for rotary microball bearings. The v-groove design, however, is different from the linear bearings in the way it is

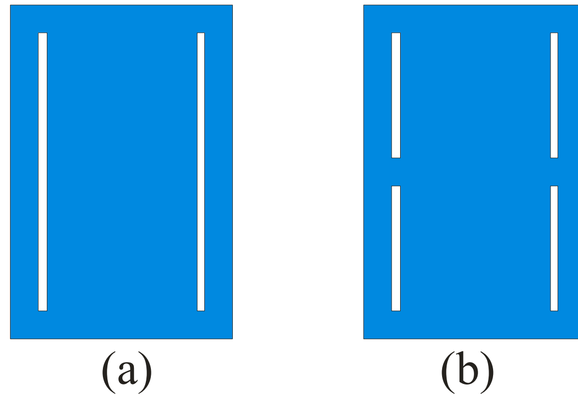

Figure 2.17. Schematic top view of two designs for linear microball bearings: (a) continuous trench and (b) split trench.

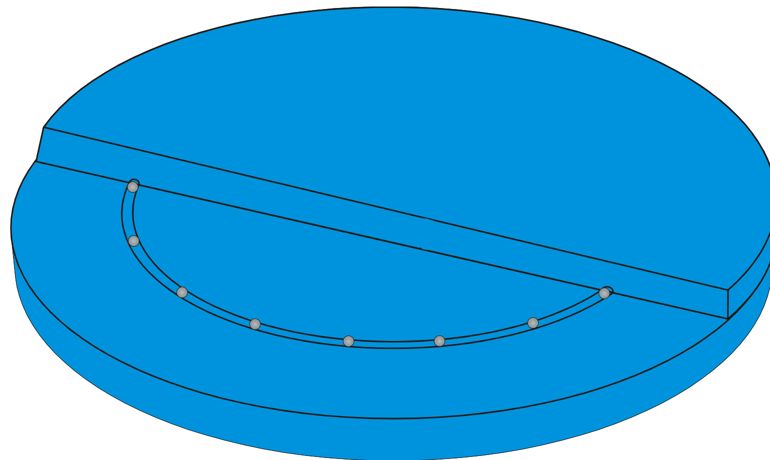

Figure 2.18. Schematic 3D view of rotary microball bearings circular v-grooves or trenches on stator and slider.

fabricated. The fabrication of the rotary microball bearings is discussed in section 3.5.2.

2.7. A Six-Phase Bottom-Drive Linear Variable-Capacitance Micromotor

The B-LVCM, shown schematically in Figure 2.19(a), consists of two silicon plates, stator and slider, and four stainless-steel microballs. The slider is free to move and supported on the microballs (~285 μm in diameter) housed in 290-μm wide parallel trenches etched in both silicon plates. The depths of these trenches define the machine air gap. The microball housings on each side of the stator active area consist

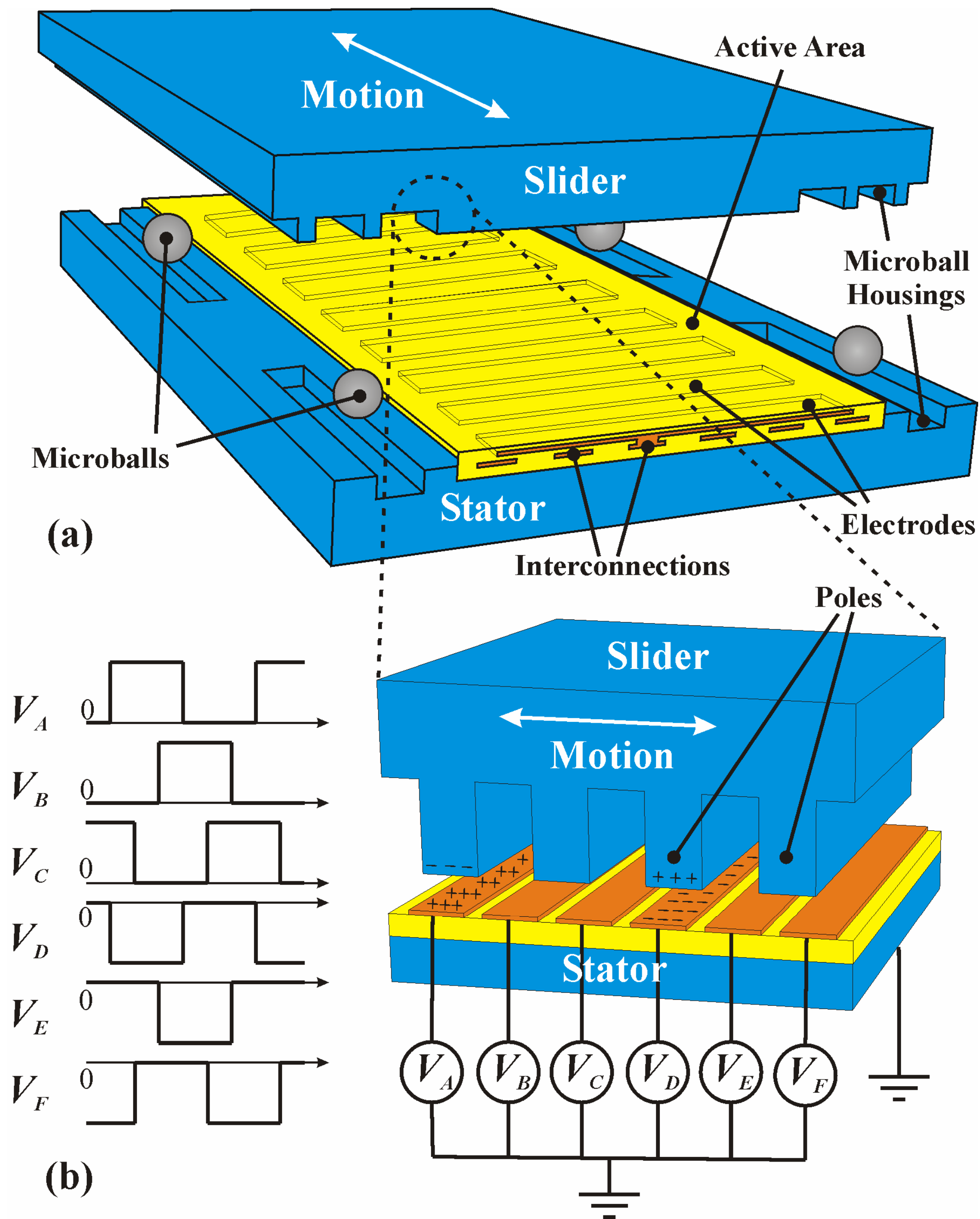

Figure 2.19. (a) Schematic 3D view of the 6-phase, bottom-drive, linear, variable-capacitance micromotor (B-LVCM), and (b) principle of operation and square-wave excitation.

of two identical separate trenches to prevent jamming and collision of the microballs. Contrary to the stator, the housings on each side of the slider active area are continuous trenches so that the maximum range of motion is achieved. Figure 2.20 and 2.21 show schematic top views of the stator and the slider, respectively.

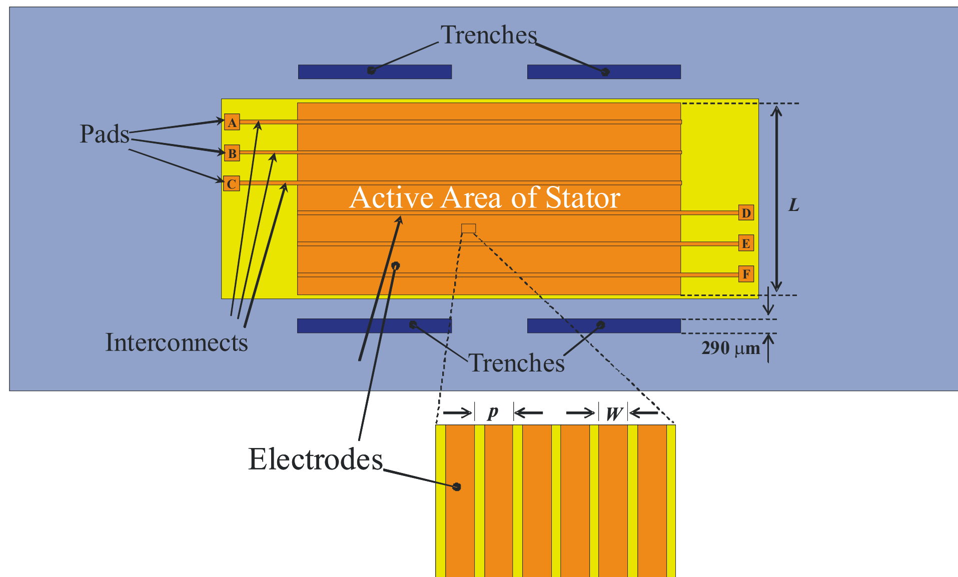

Figure 2.20. A schematic top view of the B-LVCM stator. Dimensions are to scale based on device $D2_{SHORT}$ design.

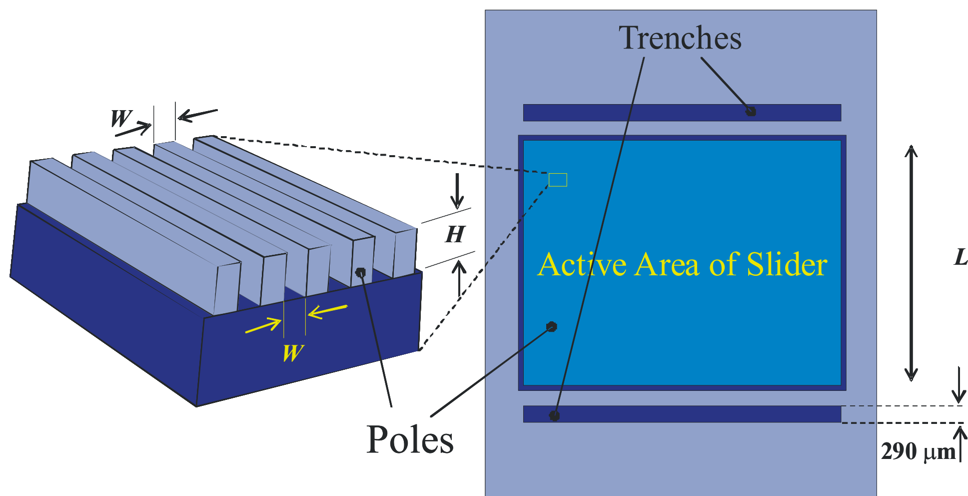

Figure 2.21. A schematic top view of the B-LVCM slider. Dimensions are to scale based on device $D2_{SHORT}$ design.

The stator active area consists of a stack of five layers: 1) an insulating BCB layer that is formed by EBiS process and electrically isolates the active area from the substrate, 2) a metal layer that forms six parallel interconnection lines, 3) an ILD BCB layer that electrically isolates the interconnection lines from electrodes, 4) a metal layer that forms several parallel electrodes, and 5) a passivation BCB layer that

protects the active area. Each interconnection line connects every sixth electrodes together to form a 6-phase motor. The slider active area consists of a salient silicon pole structure, which is formed by periodic parallel deeply-etched trenches. The slider active area is smaller (about 2/3) than the stator active area so that the size of the effective active area (where the electrostatic force is applied) is constant and equals to the size of the slider active area. This also helps to reduce the end effects caused by the fringing electric fields. The stator electrode pitch is designed to be different from the slider pole pitch so that the electrode to pole ratio is 3:2 (or 6:4 to be accurate). This provides a smoother motion of the slider compared to 2:1 and 3:1 ratios [110]. Table 2.3 shows the design parameters for six different B-LVCM devices. The difference between SHORT and LONG devices is their stator/slider length. As mentioned before, the B-LVCM is a long-range micropositioner, which is a direct benefit of microball bearing mechanism. The range of motion is defined by the length of the identical separate trenches on the stator. As shown in Table 2.3, the range of motion can be from 3 mm up to about 6 mm.

Figure 2.19(b) shows the B-LVCM principle of operation. The device can be driven by six square-wave voltages in the form of a complementary three-phase configuration, where A, B, and C are 120° out of phase, and D, E, and F are the opposite sign of A, B, and C, respectively. When the excitation voltage is applied to stator electrodes, image charges are concentrated on the slider poles. The resulting electrostatic force aligns the active electrodes and poles, leading to slider motion. A continuous motion of the slider is achieved by exciting all six phases in the

Table 2.3. Three different designs of the B-LVCM

Device	Air Gap (µm)	Electrode Width/Pitch (µm)	Pole Width/Pitch (µm)	Active Area (mm^2)	Range of Motion (mm)
$D1_{SHORT}$	5	30/40	30/60	31.05	3.86
$D1_{LONG}$	5	30/40	30/60	50.25	5.78
$D2_{SHORT}$	10	90/120	90/180	31.95	3.66
$D2_{LONG}$	10	90/120	90/180	49.95	5.82
$D3_{SHORT}$	20	180/240	180/360	35.10	3.00
$D3_{LONG}$	20	180/240	180/360	49.50	5.88

appropriate sequence. The direction of the slider motion can be changed by switching the excitation order of two complementary phase pairs (e.g. A/D and B/E).

Table 2.4 shows the estimated maximum aligning force for the six B-LVCM designs, assuming a minimum capacitance of zero and a linear profile for the spatial gradient of the capacitance. The instantaneous aligning force is a function of the slider position. The maximum capacitance was numerically calculated using FEMLAB™. For each phase, the maximum capacitance occurs when all the stator electrodes of that phase are fully aligned with a set of slider poles. The minimum capacitance occurs when there is no overlap between the stator electrodes of that phase and any of the slider poles.

Since the B-LVCM is a synchronous machine, assuming a 50 % duty cycle for the excitation waveforms, the average slider speed in steady-state continuous motion can be written as

$$u_{ave} = 2Wf_s \tag{2.61}$$

where W is the electrode/pole width and f_s is the frequency of the stator excitation. The estimated average slider speed is also shown in Table 2.4.

Table 2.4. Estimated force and speed of the B-LVCM

Device	Maximum Aligning Force at 100 V P-P (mN)		Average Slider Speed (mm/s)		
	Per Phase	Total (Six Phases)	10 Hz	20 Hz	50 Hz
$D1_{SHORT}$	1.02	3.07	0.6	1.2	3.0
$D1_{LONG}$	1.61	4.82	0.6	1.2	3.0
$D2_{SHORT}$	0.20	0.59	1.8	3.6	9.0
$D2_{LONG}$	0.31	0.93	1.8	3.6	9.0
$D3_{SHORT}$	0.05	0.14	3.6	7.2	18.0
$D3_{LONG}$	0.08	0.23	3.6	7.2	18.0

The important output parameters of the B-LVCM are the average aligning force applied to the slider, the average speed of the slider motion, and the direction of motion. For a designed B-LVCM there are certain parameters that can be changed for controlling the B-LVCM. These parameters can be used in both open-loop and closed-loop control configuration. We have used an open-loop configuration to control the B-LVCM, however, the open-loop control has a limited range of operation. A closed-loop control, which includes position sensors and active control of the excitation voltages, is especially necessary for micropositioning applications. It should be noted that with an open-loop control the precision of positioning is essentially determined by the electrode pitch and is affected by the irregularities due to fabrication tolerances. With a closed-loop control, however, the accuracy of the position sensor determines the precision of the positioning. When controlling a static parameter, e.g. position, the nonuniformities of friction do not affect the precision of the positioning. However, in controlling the dynamic parameters, e.g. speed and force, the friction profile of the bearing has to be taken into account.

Chapter 3: Material Characterization, Process Development, and Device Fabrication

As mentioned in chapter 1, BCB-based polymers have outstanding features that make them a promising material for a variety of MEMS applications. In this work, BCB has been used as an insulating dielectric material in electrostatic micromachines to replace the traditional silicon dioxide. BCB has already proven to be an important dielectric material in microelectronic applications for packaging and multichip modules [78-81] and in MEMS for bonding [92, 111], mechanical support , and structural components [96, 97]. This is the first time that BCB is being used as an electrical component for MEMS applications. Therefore, an understanding of BCB electrical properties and the effect of design, process, and operation parameters, as well as reliability issues is necessary to predict and evaluate the performance of a BCB-based device. In order to address this need, we have developed a characterization methodology to study specific electrical properties of BCB and the effect of moisture absorption. This study provides us with specific knowledge to design and fabricate efficient, reliable electrostatic microactuators with BCB insulating films.

In order to incorporate the BCB polymer films in the fabrication of the device, we have developed the embedded BCB in silicon (EBiS) process, a novel, unique fabrication method for BCB-based electrostatic microactuators that is applicable to a variety of applications. The key step in the EBiS process is chemical mechanical planarization (CMP) of BCB films. CMP of polymers has not been studied as extensively as conventional materials such as silicon, silicon dioxide, and silicon

nitride. Therefore, we characterized CMP of BCB polymers, which will be discussed later in this chapter. Other fabrication processes of BCB polymers such as deposition, pattern transfer (etching for dry-etch BCB and photolithography for photosensitive BCB), curing, removal, etc. are standard and discussed in great detail in the manufacturers' documents (see Tables 1.2 and 1.3). Fabrication of the stator and the slider will also be discussed in this chapter.

3.1. Electrical Characterization of Benzocyclobutene Polymers

As elaborated in Chapter 1, the motivation behind using BCB-based polymers in electrostatic micromachines is to reduce the electrical loss by minimizing the parasitic capacitance associated with the insulating dielectric layer on the stator. This relies on the low dielectric constant and the large thickness of the BCB film. In addition, the residual stress of BCB film compared to silicon dioxide is much lower (see Table 1.4) and causes less wafer bow, film cracks, and better mechanical robustness and reliability. However, BCB film absorbs a small amount of moisture when exposed to an open environment. Furthermore, it is subject to a series of wet processes and moderate temperatures during the development of the device. As a result, its electrical and mechanical properties might degrade, leading to device failure during the operation. The low dielectric constant of BCB is a key factor in our application and needs to be reliable under process and operational conditions to guarantee the expected efficiency and performance. One reliability issue is the electrical breakdown, which is especially important in electrostatic micromachines because the operating voltage level is quite high. The breakdown limits the maximum performance of the device. All these issues need to be investigated to obtain a clear

understanding of the behavior of BCB as a dielectric material for MEMS applications.

Most of background information on BCB polymers and their unique features were discussed in Section 1.3.2. In this section, we present the results of two fundamental research activities on BCB polymers, electrical characterization, which is the key to understanding the electrical behavior of this material as an insulating film, and characterization of CMP, which is the most challenging process step in fabrication of the micromotor.

The electrical properties studied in this work are the dielectric constant (more accurately, the real part of the complex dielectric constant) and the current-voltage (I-V) characteristic of the BCB film. The leakage current and the breakdown voltage can be determined from the I-V curve. For a specific geometry, the dielectric strength (the electric field at breakdown) can be calculated using the measured breakdown voltage. We have also studied the effect of moisture uptake on these properties and the reliability issues associated with that. Another electrical property of a dielectric material is the dissipation factor (dielectric loss tangent, or the imaginary-to-real-part ratio of the complex dielectric constant), which becomes important at high frequencies. Since the micromotor is a low frequency device, the dissipation factor was not a subject of our study, although it was measured to verify the validity of dielectric constant measurement.

Since the introduction of BCB-based polymers for microelectronic applications in 1990, there have been a few studies on the electrical characterization of these materials. The methods of measurement and/or the test structures are not

clearly described in publications on most of previous studies, and therefore, it is not possible to compare the results. There are also some discrepancies in the reported data for some of the electrical properties. Most studies, with couple of exceptions, have been done on thin (1 μm) films.

The reported dielectric constant in the literature ranges as high as 3.1 [76]. The nominal dielectric constant of BCB is 2.65 as mentioned in [77] and the data specification sheets from the manufacturer. It was also reported to be flat over a wide range of frequencies (1 kHz to 60 GHz) and temperatures (25 °C to 200 °C) [77, 79, 80], although it was reported that the dielectric constant changes drastically with cure temperature [112]. Capacitance measurements on free-standing films yielded a dielectric constant of 2.6 to 2.8 [79, 80]. Extraction of the dielectric constant from accumulation capacitance of 1 MHz C-V curves of metal-insulator-semiconductor capacitors yielded values from 2.2 to 2.8 for cure temperatures from 200 °C to 350 °C [112].

Less data was reported for I-V characteristics of BCB. The nominal value of dielectric strength as mentioned in the specification data sheet from Dow Chemical is 3×10^6 V/cm. The dielectric strength measured on a 1.7-μm thin film deposited on silicon substrate was reported to be 4×10^6 V/cm while it was measured to be 2.5×10^6 V/cm for a 22-μm free standing film [79, 80].

The phenomena of moisture uptake in BCB films was studied in detail using gravimetric measurements [113], however, no electrical characterization was performed in that study. It was also stated that the change in the dielectric constant of BCB-based dielectric polymers under humid conditions is negligible since DVS-bis-

BCB has a nonpolar molecular structure [77], although no experimental data was presented to support the statement.

In this chapter, we introduce a method suitable for measuring the dielectric constant and the I-V characteristics of thick, spin-on dielectric materials. We have used this method to measure the electrical properties of BCB and the effect of moisture uptake on these properties.

3.1.1. Test Structures

The test devices used for electrical characterization of BCB polymer films are interdigitated capacitors (IDCs) with fine finger width and spacing, relatively large finger length, and a large number of fingers. The IDCs are thin metal structures sandwiched between two layers of the dielectric film. There are two reasons that this type of device was chosen for characterization of the electrical properties. The periodic structure of an IDC is similar to that of the stator electrodes in the electrostatic micromotor; and in order to study the effect of the moisture uptake, it is easier and faster for the underlying dielectric layer to absorb moisture through the spacing between the fingers in the IDC. The IDCs were used in both dielectric constant and I-V characteristic measurements.

3.1.1.1 Design

Figure 3.1 shows the schematics of the top and cross-section views of an IDC. All designed IDCs have 500 fingers (250 fingers for each electrode) with equal finger width and spacing (a finger width to pitch ratio of 0.5). There are four different finger widths, 1 μm, 2 μm, 3 μm, and 4 μm and two different finger lengths, 1mm and 10

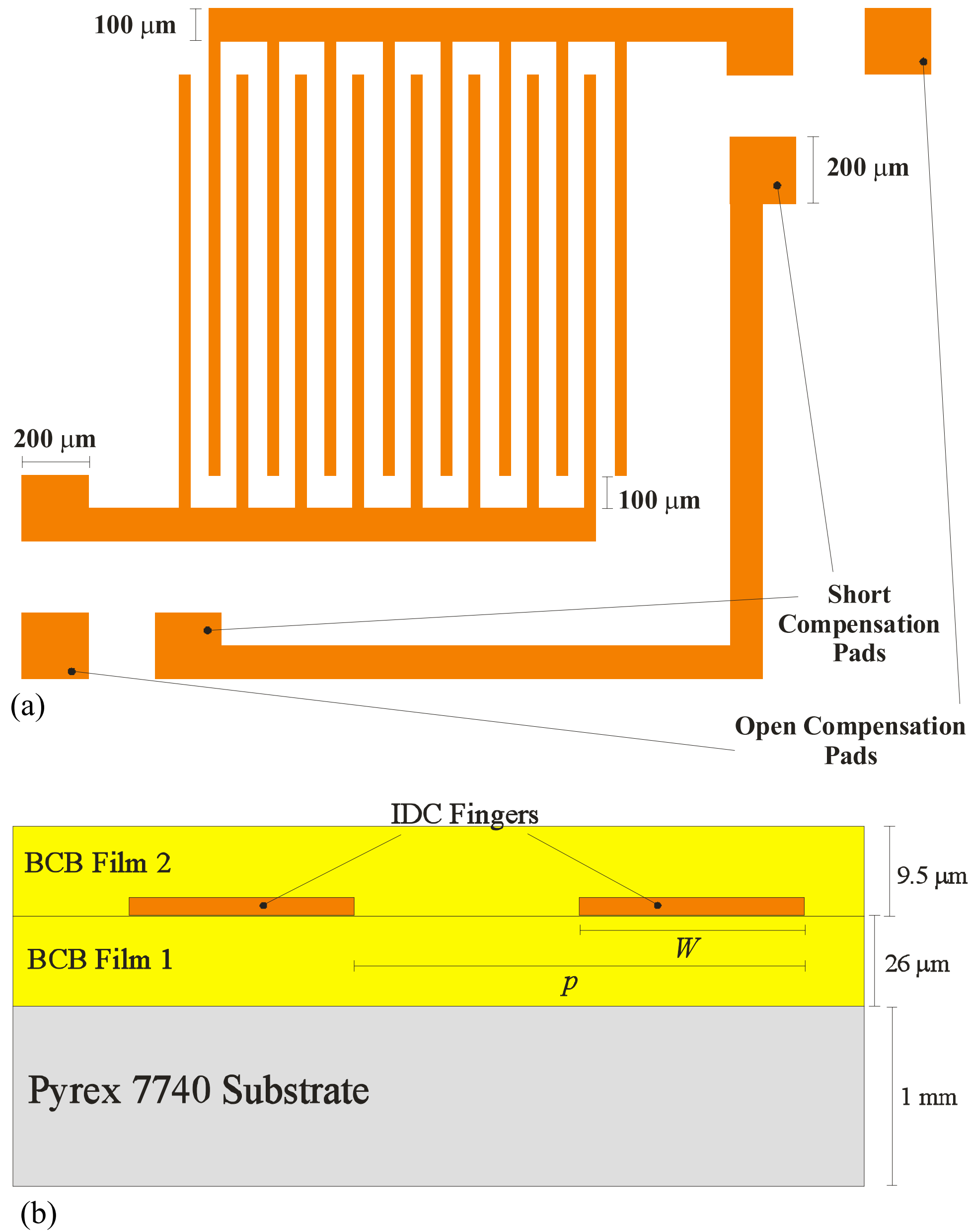

Figure 3.1. Schematic views of an IDC test structure, (a) top view and (b) cross-section view. Dimensions are not to scale.

mm, hence, eight different IDCs. We used a 1-mm-thick, 4” Pyrex 7740 wafer as the substrate. The important physical properties of Pyrex 7740 are summarized in Table 3.1. Since Pyrex is a non-conducting material, using a Pyrex wafer instead of a silicon wafer minimizes the effect of parasitic elements during the tests. We experienced difficulties in fabrication when using a 0.5-mm-thick Pyrex wafer due to the wafer

Table 3.1. Physical Properties of Pyrex 7740 (at 25 °C unless otherwise noted)

	Physical Property	Condition	Unit	Value
Electrical	Dielectric Constant	at 1 MHz		4.6
	Dissipation Factor	at 1 MHz		0.004
	Dielectric Strength		V/m	5×10^5
	Volume Resistivity		Ω.m	8×10^{12}
Mechanical	Density		kg/m^3	2230
	Young's Modulus		GPa	62.8
	Poisson Ratio			0.2
	Shear Modulus		GPa	26.2
	Flexural Strength		MPa	69
	Knoop Hardness		TPa	4.1
Thermal	Thermal Conductivity		W/m.K	1.1
	Specific Heat		J/kg.K	180
	CTE	0-300 °C	ppm/°C	3.25
	Thermal Diffusivity		m^2/s	6.9×10^{-7}
	Strain Point		°C	510
	Annealing Point		°C	560
	Softening Point		°C	821
	Working Point		°C	1252
Optical	Index of Refraction	at 589.3 nm		1.474
	Transmission (1-mm-thick sample)	at 440 nm at 560 nm	%	91 91.8

bow caused by the residual stress of thick dielectric films; therefore, a 1-mm-thick wafer was used.

There are some design considerations when choosing the thickness of the dielectric layers and the thickness of the metal film. The thickness of the bottom and top dielectric films needs to be larger than the pitch of the IDC under test for reasons that will be discussed in Section 3.1.3.1. Cyclotene 3022-63 was used as the dielectric

under test. Having the highest viscosity among Cyclotene solutions, it provides a maximum of 26 μm and a minimum of 9.5 μm film thickness after cure and allows using a larger pitch IDC. The bottom and top dielectric films are designed to be 26 μm and 9.5 μm thick, respectively, both with a thickness bigger than the largest pitch (8 μm). A thicker dielectric top layer leads to a more complicated fabrication process. Furthermore, the thickness of the metal film compared to the finger width is an important parameter that affects the capacitance measurements. A metal film of zero thickness is ideal, but if the metal film is too thin, the resistance of IDC electrodes becomes large, leading to difficulties and errors in measurements. Our measurements have shown that a metal thickness near 3000 Å provides reasonably low resistance electrodes. On the other hand, if the metal thickness is comparable to the finger width, a numerical compensation is necessary when measuring the dielectric constant with this method.

3.1.1.2 Fabrication

The fabrication process flow of test devices is shown in Figure 3.2. As the figure shows, capacitance test step I is performed on an intermediate device before the second layer of BCB is deposited. The capacitance test step II and the I-V test are performed on the final device with two layers of BCB. The sample is baked in a 5 liter/min flow of nitrogen at 200 °C for two hours before each test step. The nitrogen bake drives the absorbed moisture out of the BCB film.

The test structures were fabricated on a 1 mm thick, 4” Pyrex 7740 wafer (see Table 3.1). It is very important that the wafer is cleaned aggressively and dehydrated long enough to remove any organic residues and moisture right before deposition of

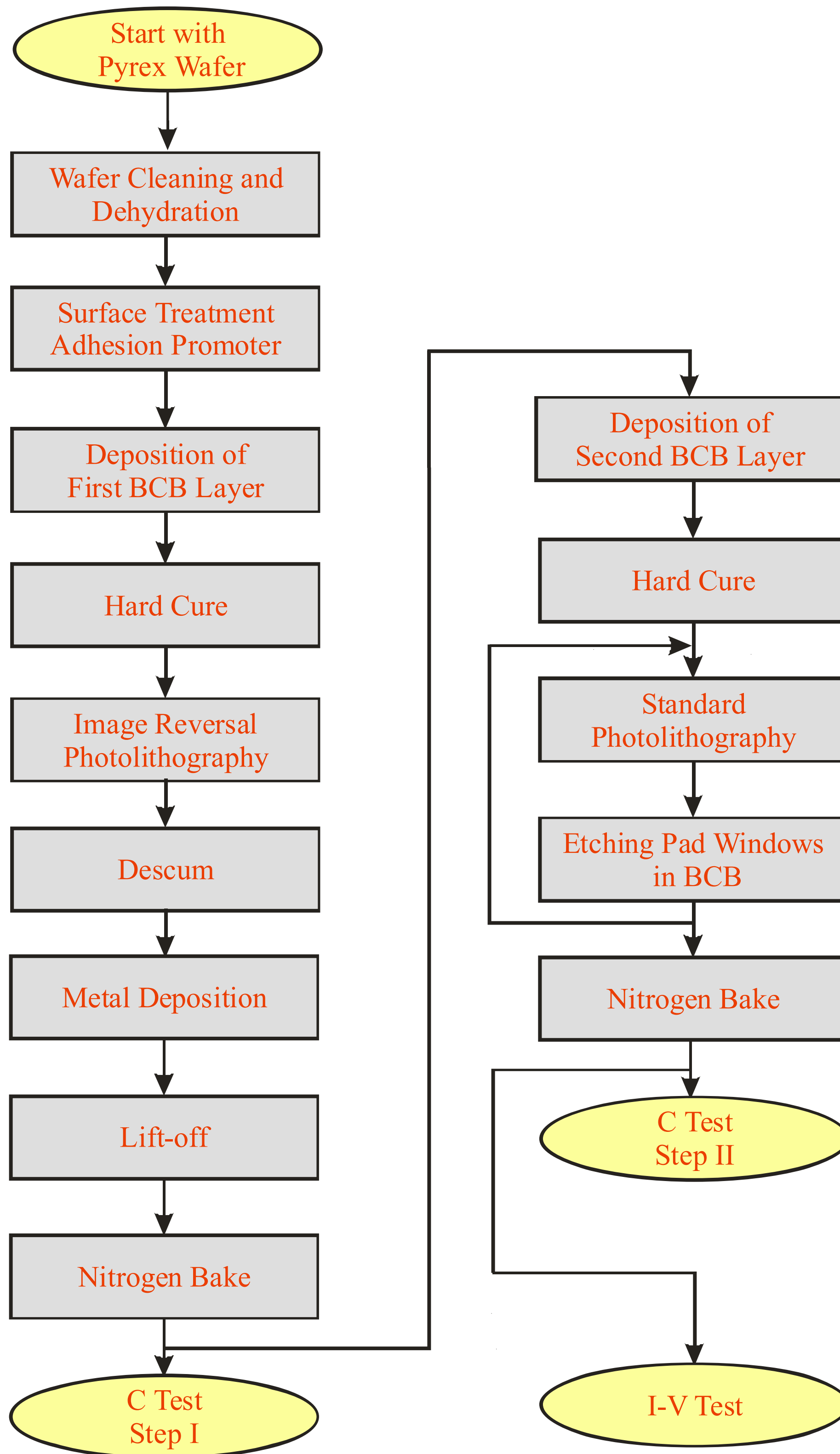

Figure 3.2. Process flow for fabrication of IDC test structures showing at what steps capacitance and current-voltage tests are performed.

BCB. An adhesion promoter, AP3000 from Dow Chemical was applied onto the wafer to improve the adhesion of BCB to the substrate and a 26 μm thick BCB (Cyclotene 3022-63) film was spun on and hard cured at 250 °C for one hour in the nitrogen flow.

We used a lift-off process to fabricate the IDCs, providing smoother and more accurate metal lines. Furthermore, the advantage of lift-off over a metal etching process in this case was to avoid the exposure of the deposited BCB film to metal etchants that contain strong acids. In order to facilitate the lift-off process, an image reversal photolithography was used to pattern AZ5214E photoresist. AZ5214E is a positive-tone photoresist from Clariant Corporation (Muttenz, Switzerland). A post exposure bake at 125 °C for 3 minutes reverses the tone of this photoresist and a flood exposure with a high dose of 1200 mJ/cm^2 makes the unexposed areas soluble in developer. This makes the AZ5214E image reversal process suitable for lift-off, because it reverses not only the pattern but also the profile of the photoresist, providing a re-entrant profile. After photolithography, a 30 second oxygen (O_2) plasma descumming was performed on the wafer to remove any remaining photoresist residue after development. A Minilock™ (Trion Technology, Tempe, AZ) plasma etcher was used for descumming at an RF power of 50 W, a chamber pressure of 200 mT, and an oxygen flow of 50 sccm, removing the AZ5214E photoresist at 3600 Å/min. The metal layers (200 Å of Cr and 3000 Å of Au) were then deposited using e-beam evaporation. The lift-off was performed in an ultrasonic bath to fabricate the IDCs. The wafer was treated with ultrasonic waves for one hour inside acetone and one hour inside deionized (DI) water.

After the first test step, a second layer of Cyclotene 3022-63 with a thickness of 9.5 µm was spun on and cured in a similar way to the first layer. However, no AP3000 was applied prior to the deposition of the second layer for two reasons: (1) we had noticed in our experiments that AP3000 reacted with cured BCB when spun on it, and (2) when cured, the two BCB layers would naturally bond together encapsulating the IDC metal structures, so there was no need for an adhesion promoter between the two.

Since the etch selectivity of BCB over photoresist etch mask is quite low, we performed two series of photolithography with AZ9245, a positive photoresist from Clariant, and two dry etching steps to open windows in the BCB film for IDC electrode pads. The BCB was etched for a total time of 30 minutes with O_2/CF_4 in the plasma etcher at an RF power of 100 W, a chamber pressure of 250 mT, an O_2 flow of 90 sccm, and a CF_4 flow of 10 sccm. The etch rate of BCB was measured to be about 0.3 µm/min with an etch selectivity of about 0.6 to AZ9245 photoresist.

Separate samples were fabricated for C and I-V tests. Figure 3.3 shows optical micrographs of the fabricated IDCs.

3.1.2. Environmental Test Setup

A custom-made environmental test setup was built to study the reliability of BCB film and its electrical properties before and after moisture uptake, which might occur if the film was exposed to an open environment. The setup consists of two parts: a humidity-stress setup and an electrical test setup.

The humidity-stress setup was intended to accelerate the moisture uptake in the BCB film by exposing the sample to a flow of hot, humid nitrogen for a certain

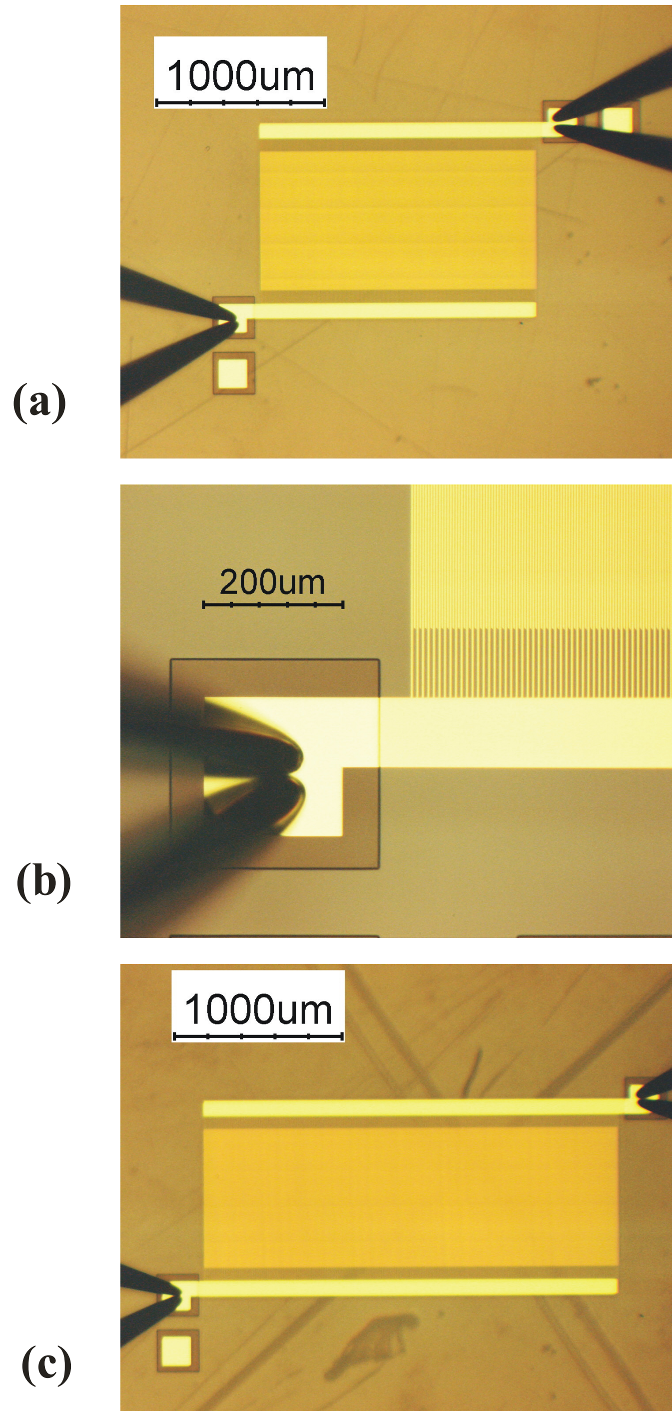

Figure 3.3. Optical micrographs of fabricated IDCs with (a), (b) 2-µm finger width/spacing, and (c) 3-µm finger width/spacing.

period of time (usually 2-3 hours is enough time to saturate the BCB film with moisture). The setup is capable of maintaining a temperature of 85 °C and a relative humidity of 85 %RH inside a wafer chamber (humidity-stress chamber). Dry nitrogen

is heated by passing through a pipe heater and then is mixed with steam before entering the chamber. The steam is sucked from a boiling water container by a small fan. Two heaters on the top and bottom of the chamber help to keep the temperature constant inside the chamber and prevent condensation on the wafer. A thermo-hygrometer reads the temperature and relative humidity. The temperature and relative humidity are adjusted by manually controlling the heaters, and the flows of nitrogen and steam. It should be noted that the chamber is not air tight. A picture of the humidity-stress setup is shown in Figure 3.4.

The electrical test setup allows performing different electrical tests on the sample under a flow of dry nitrogen at room temperature. The setup was built to fit on the wafer chuck of a probe station and includes a wafer chamber (electrical test chamber), which houses the wafer under a constant flow of dry nitrogen at room temperature. The chamber has windows for insertion of four test probes and a thermo-hygrometer sensor. Figure 3.5 shows pictures of the electrical test setup and the chamber during a capacitance measurement. The electrical test setup includes several instruments and equipment to facilitate the I-V and C tests and data collection. Figure 3.6 shows the block diagram of the electrical test setup.

3.1.3. Measurement of Dielectric Constant

In this section, we describe a method that is suitable for measurement of the dielectric constant of any film provided that it can be spin-coated (or deposited in some other way) on the wafer thicker than the pitch of the IDC under test. This method is based on two capacitance measurements on IDCs and it has some advantages over the conventional parallel-plate-capacitor method. This approach is

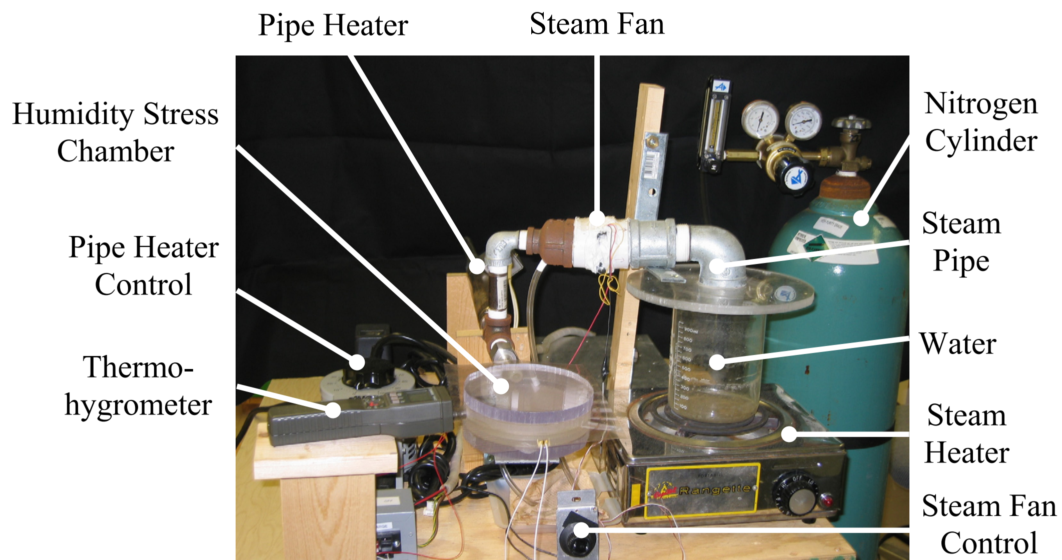

Figure 3.4. The custom-made humidity-stress setup.

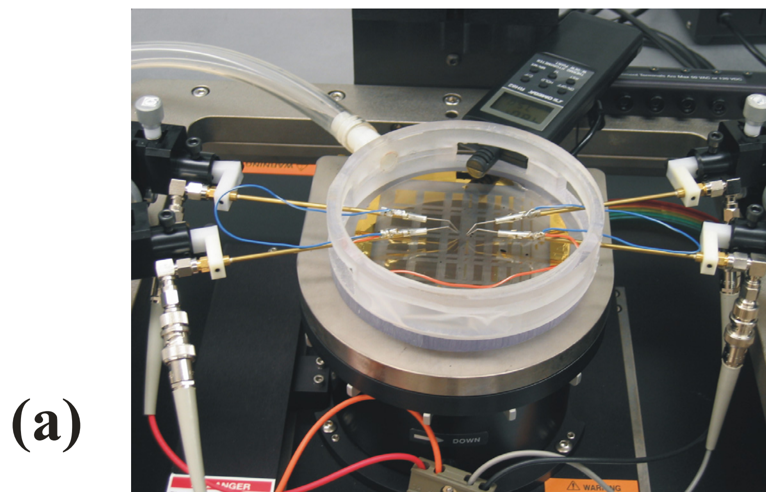

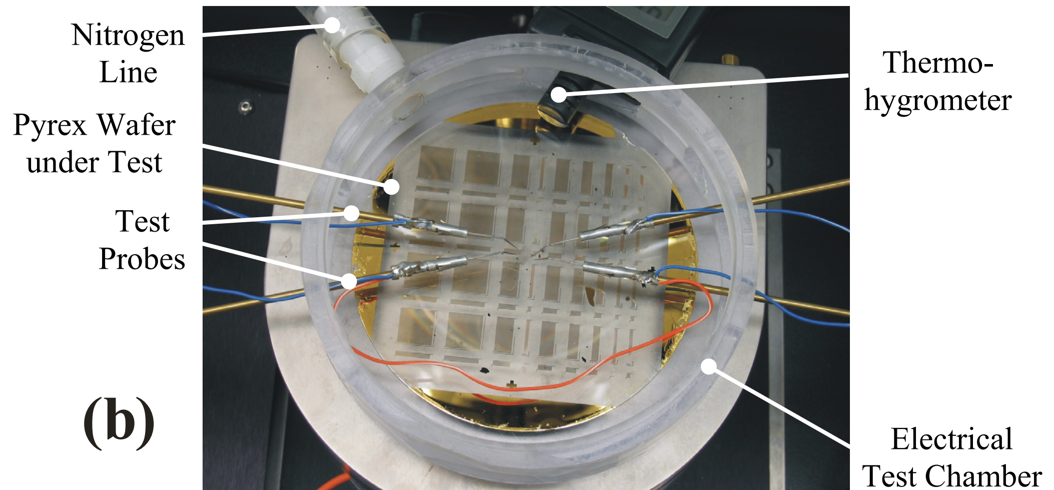

Figure 3.5. (a) The electrical test setup and (b) the electrical test chamber.

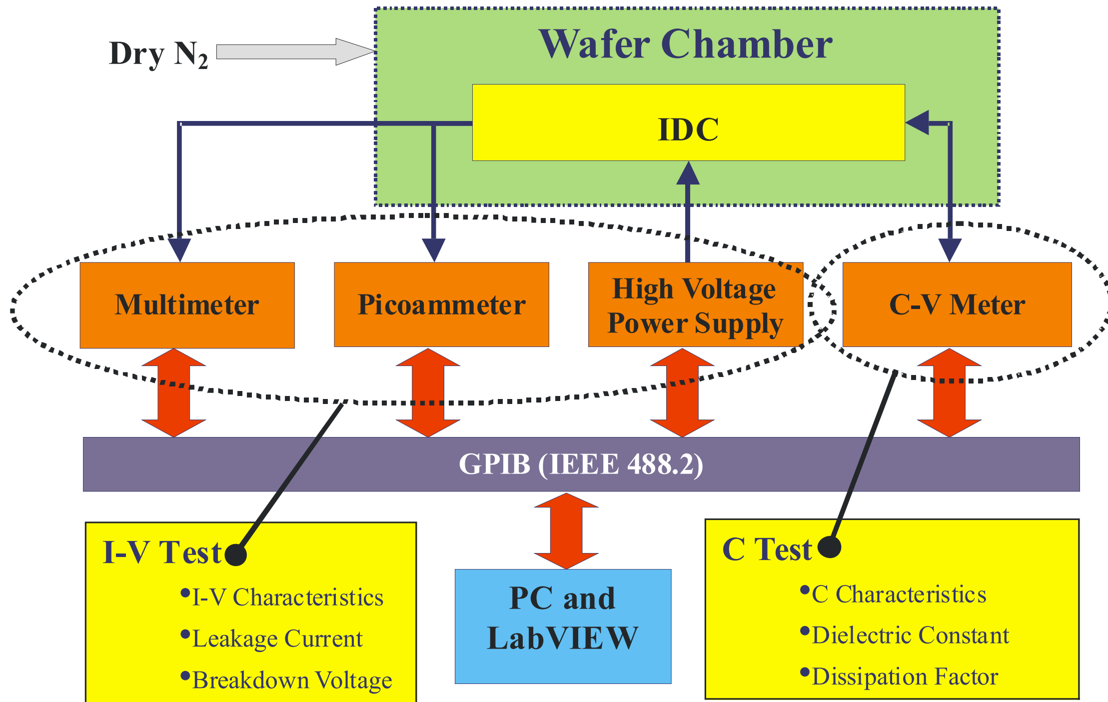

Figure 3.6. Block diagram of the electrical test setup.

independent of the thickness of the dielectric material under test as long as it is thicker than the pitch of the IDCs. Under some circumstances it can also be independent of the geometrical features of the devices under test. It is also a useful method to measure the effective dielectric constant over a large area to take into account the fabrication imperfections. This makes the method applicable for large area devices like micromotors and microgenerators. In addition, the special structure of IDCs makes the study of the effect of moisture uptake easier. We have applied this method to BCB films using the fabricated IDCs.

3.1.3.1. Theory

In general, the capacitance of an IDC sandwiched between two dielectric layers, as shown in Figure 3.7, can be calculated provided that the number of IDC fingers (N), the IDC finger length (L), width (W), thickness (t), and pitch (p), the dielectric layers thickness (d_1 and d_2), and relative permittivity (k_{D1} and k_{D2}) are

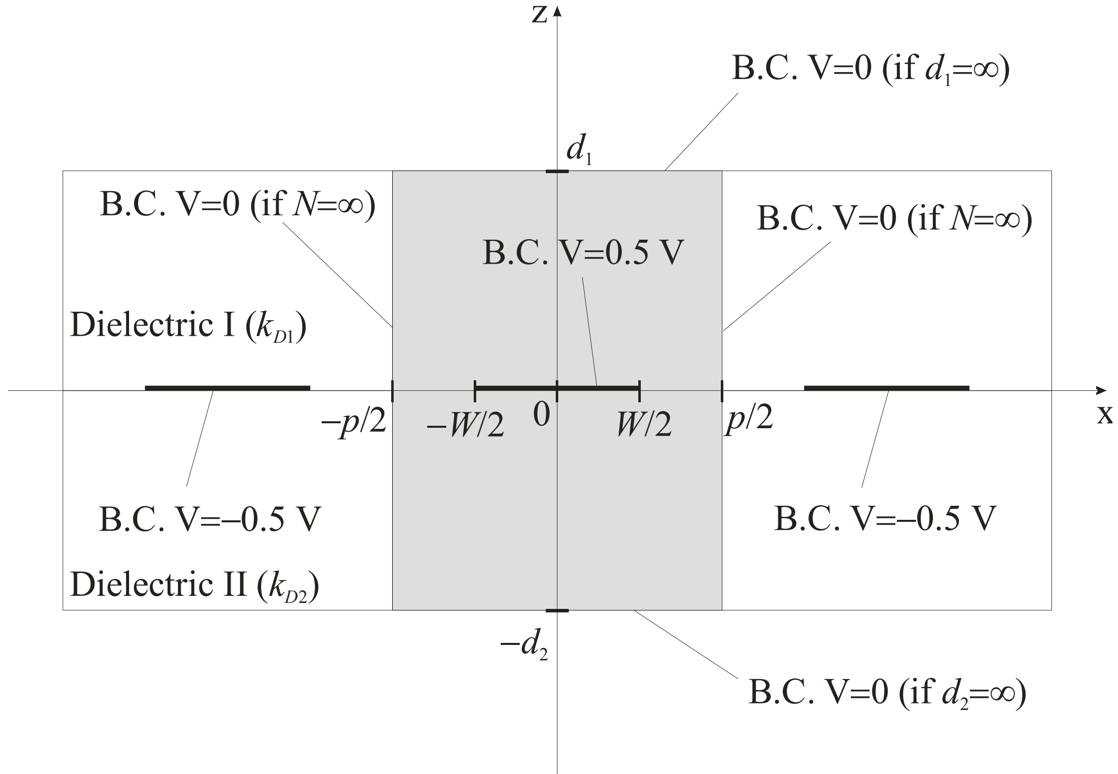

Figure 3.7. Schematic cross section of an IDC showing the dielectric layers, fingers, and boundary conditions. The electric potential between two adjacent fingers is assumed to be 1 V. Due to the symmetric structure of an ideal IDC, the solution is a periodic function with the period of p, therefore, the Laplace Equation is solved analytically and numerically in the shaded area.
(W: finger width, p: finger pitch).

known. The solution to this problem is complicated and a closed form solution might not be possible. However, in most cases an estimation based on the simplified *ideal* IDC problem is satisfactory.

The ideal IDC problem is defined with the following assumptions: (i) N is infinite, (ii) L is infinite, (iii) t is zero, (iv) d_1 and d_2 are infinite, and (v) the dielectric materials are isotropic. These assumptions allow building a simple two-dimensional (2D) symmetric model for the complex three-dimensional (3D) asymmetric structure. Solving the Laplace Equation over the shaded area in Figure 3.7 with the above

assumptions and the specified boundary conditions (B.C.) yields the following equation for the capacitance per finger per unit length [114]:

$$C = \frac{(k_{D1} + k_{D2})\varepsilon_0}{\mathrm{K}\left(\cos\frac{\pi W}{2p}\right)} \sum_{n=0}^{\infty} \frac{\mathrm{P}_{n-1}\left(\cos\frac{\pi W}{p}\right)}{2n+1} \sin\left(\frac{(2n+1)\pi W}{2p}\right) \tag{3.1}$$

where k_{D1} and k_{D2} are the dielectric constants of bottom and top dielectric layers, respectively, ε_0 is the permittivity of vacuum, W is the finger width, p is the finger pitch, $\mathrm{K}(x)$ is the complete elliptic integral of the first kind, and $\mathrm{P}_{n\text{-}1}(x)$ is the Legndere Polynomial of the order of n. A closer look at equation (3.1) shows that it can be written in the following form:

$$C = (k_{D1} + k_{D2})\varepsilon_0 \, \mathrm{G}\left(\frac{W}{p}\right) \tag{3.2}$$

where G is a function of IDC finger width to pitch ratio. In other words, G is only a function of geometrical features of the IDC, and is independent of the material properties. Equation (3.1), and therefore equation (3.2) are relatively accurate for non-ideal IDCs if: (i) N is large, (ii) $L >> W$, (iii) $t << p-W$, and (iv) $d_1 > p$, $d_2 > p$.

The effect of the finite thickness of dielectric layers on the IDC capacitance is analytically shown in [114]. For a non-ideal IDC with a 26-µm bottom dielectric layer and a 9.5-µm top dielectric layer as shown in Figure 3.1(b), the analysis predicts an error of 0.03% and 0.12 % in the calculated capacitance of 6-µm pitch and 10-µm pitch IDCs, respectively, when using equation (3.2). This prediction is in agreement with our numerical simulation of the IDC capacitance with FEMLAB™ (COMSOL Inc., Burlington, MA) as seen in Figure 3.8. As a result, the capacitance of an IDC can be accurately modeled by equation (3.2) if the thickness of dielectric layers is

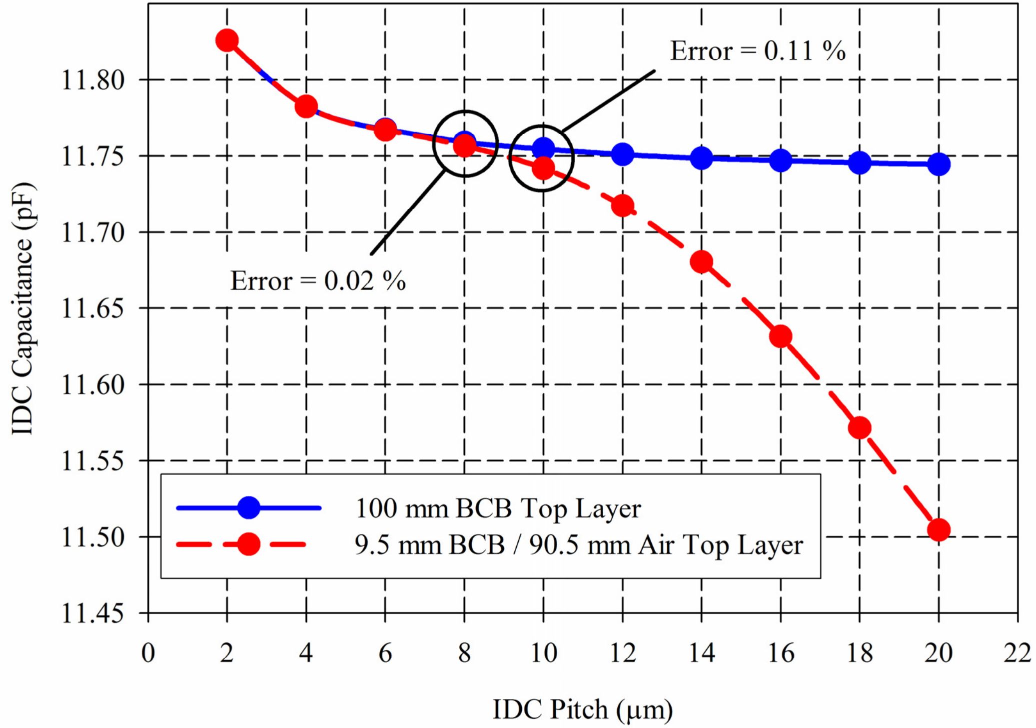

Figure 3.8. Two-dimensional (2D) finite-element numerical simulation of the capacitance vs. pitch in a 500-finger IDC with 1-mm long fingers, showing the effect of BCB top layer thickness. The simulation is performed based on the IDC design of Figure 2.1 and boundary conditions of Figure 2.7. The blue graph represents the (almost) ideal case assuming a very thick (100 µm) BCB layer on top and the red graph is for the IDC design assuming 9.5 µm of BCB and 90.5 µm of air on top. As the graphs show, the capacitance of the 8-µm pitch IDC deviates from the ideal case by only 0.02 % while as the pitch increases beyond the BCB top layer thickness, the deviation blows up drastically. Note that the increase in capacitance at smaller pitches is due to the non-zero finger thickness (0.004 µm in this simulation).

larger than the IDC pitch. We have also experimentally demonstrated the accuracy of the model as shown in Figure 3.9.

Based on the above observations, for an IDC with N fingers and finger length L, the total capacitance of an IDC, if the required assumptions are met, can be written from equation (3.2) as:

$$C_T = (k_{D1} + k_{D2})\varepsilon_0 NL\,\mathrm{G}\left(\frac{W}{p}\right) = (k_{D1} + k_{D2})\varepsilon_0\,\mathrm{G}_T\left(\frac{W}{p}\right) \tag{3.3}$$

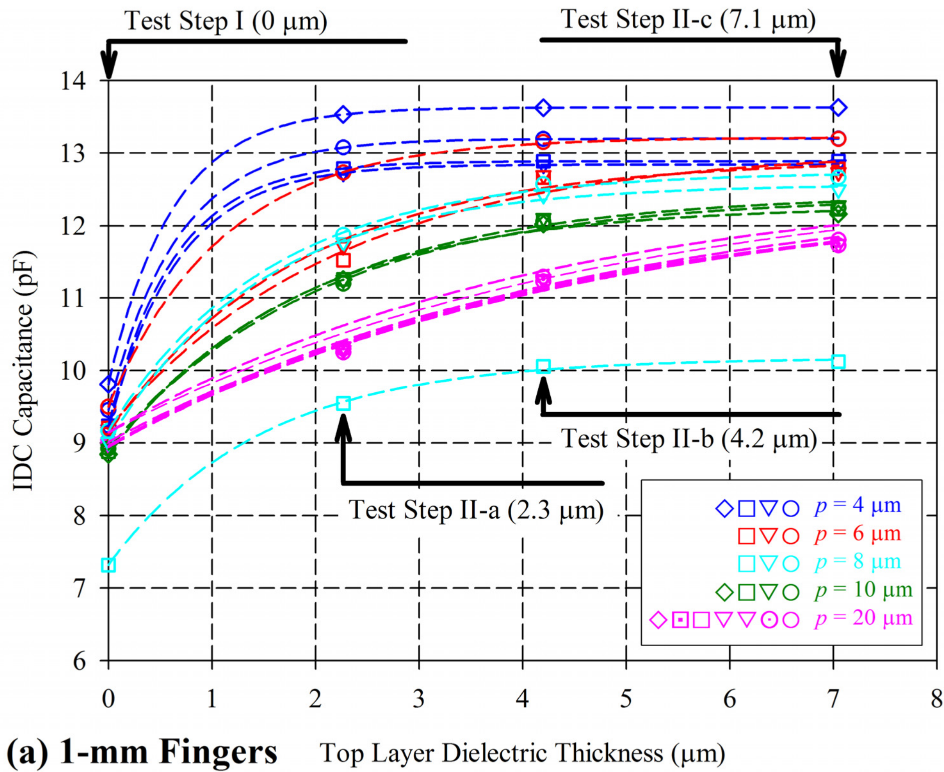

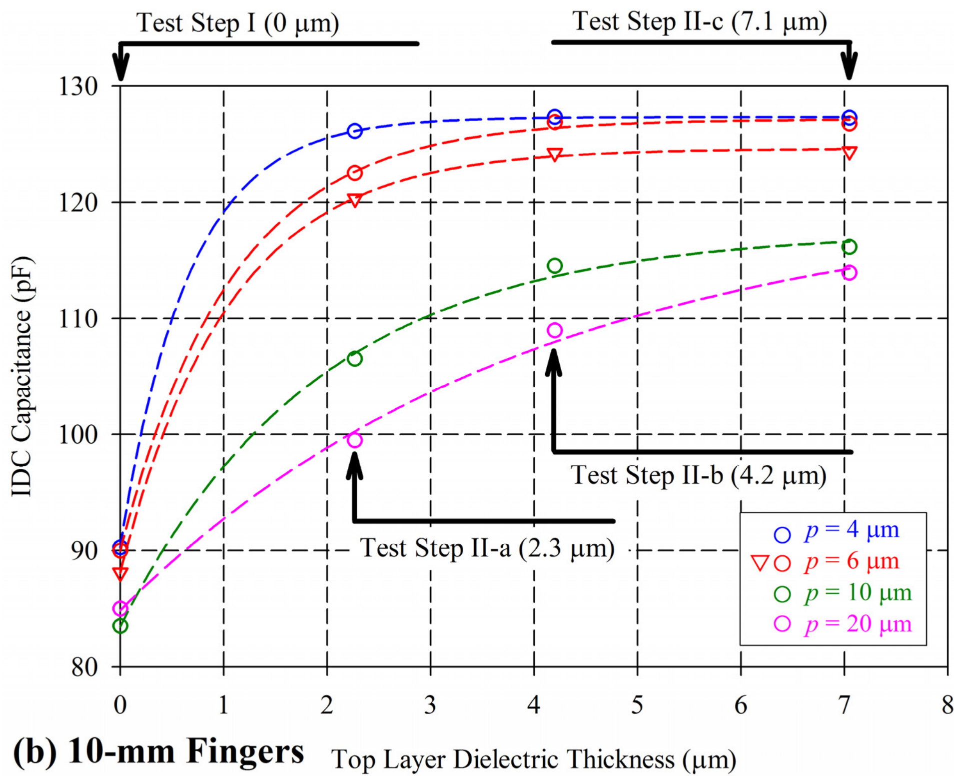

Figure 3.9. Capacitance measurement on several IDCs with different pitch sizes before (0 µm) and after (3.3 µm, 4.2 µm, 7.1 µm) deposition of the second BCB layer: (a) 1-mm long fingers and (b) 10-mm long fingers. The capacitance becomes independent of the BCB thickness as the thickness increases beyond the pitch.

where $G_T = NLG$. We call G_T the geometry factor of an IDC with N fingers of length L and a width to pitch ratio of W/p. Note that changing the finger width, W, does not change the capacitance as long as W/p remains constant.

Our method for measurement of the dielectric constant is based on equation (3.3). Since the geometry factor does not change with material properties, it is possible to extract k_{D1} or k_{D2} if the other is known using two capacitance tests (see Figure 3.2). In the capacitance test step I, the bottom dielectric layer is the BCB polymer ($k_{D1}=k_{\mathrm{BCB}}$) and the top dielectric layer is dry nitrogen ($k_{D2}=1.00058\cong1.00$), therefore equation (3.3) becomes:

$$C_I = (k_{BCB} + 1)\varepsilon_0 \, G_T \,. \qquad (3.4)$$

In the capacitance test step II, both layers are BCB ($k_{D1}=k_{D2}=k_{\mathrm{BCB}}$), and therefore we can rewrite equation (3.3) as:

$$C_{II} = 2k_{BCB}\varepsilon_0 \, G_T \,. \qquad (3.5)$$

Then, k_{BCB} is extracted from equations (3.4) and (3.5):

$$k_{BCB} = \left(\frac{2C_I}{C_{II}} - 1 \right)^{-1} \qquad (3.6)$$

where the capacitance ratio must satisfy $0.5 < C_I / C_{II} < 1$. For practical low-k materials the ratio range narrows down to $0.625 < C_I / C_{II} < 0.75$.

It is possible to compensate for the effect of finger thickness on the capacitance of IDC. Figure 3.10 shows the result of simulation with FEMLAB for 500-finger IDCs designed for this study. The capacitance per unit length of IDCs with different finger width is plotted versus the finger thickness. As Figure 3.10 shows and equation (3.3) verifies the capacitance of all IDCs is the same when finger thickness

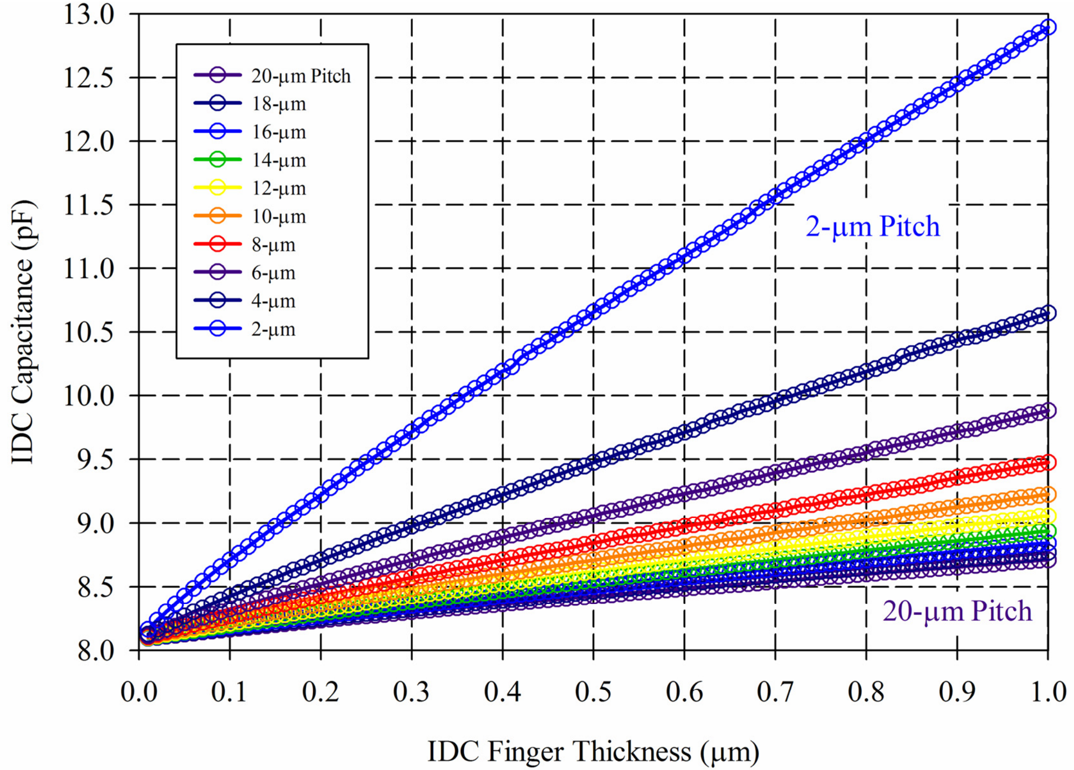

Figure 3.10. Estimation for the capacitance of 500-finger IDCs based on the FEA simulation of a single pitch. For IDCs with very thin fingers the capacitance is almost independent of the IDC pitch and finger width as far as the ratio remains constant. As the thickness increases, the capacitance of large-pitch IDCs is less sensitive. The finger length was 1 mm in this simulation.

is small. As the finger thickness increases, the capacitance also increases linearly and deviates from the ideal IDC case; however, this deviation is more severe for smaller finger widths, as expected. Based on this observation, for an IDC with considerable finger thickness, we can add an extra capacitance term associated with a parallel-plate capacitor defined between the walls of fingers (see Figure 3.11). Therefore equation (3.3) is corrected as:

$$C_T = C_{top} + C_{bottom} + C_{thickness} = (k_{D1} + k_{D2})\varepsilon_0 \, \mathrm{G}_T\left(\frac{W}{p}\right) + C_{thickness}. \quad (3.7)$$

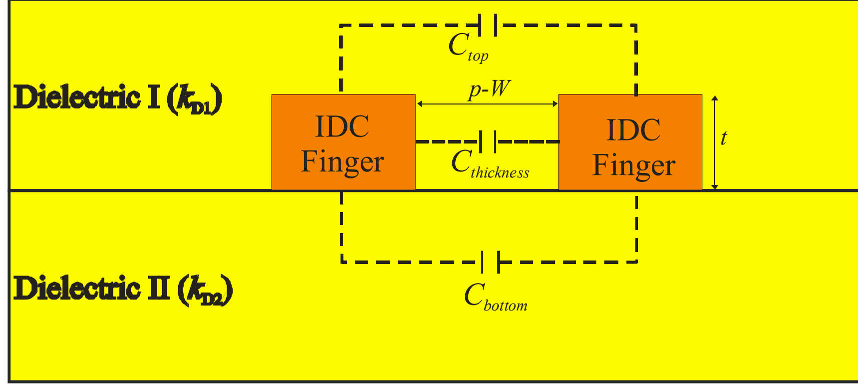

Figure 3.11. Schematic cross section of an IDC with thick fingers.

The extra term increases linearly with finger thickness and is proportional to the number of fingers and finger length:

$$C_{thickness} = k_{D2}\varepsilon_0 NL\frac{t}{p-W}. \tag{3.8}$$

Application of this correction to equations (3.4) and (3.5) and considering p=2W yields:

$$C_I = (k_{BCB}+1)\varepsilon_0\, G_T + \varepsilon_0 NL\frac{t}{W} = (k_{BCB}+1)\varepsilon_0\, G_T + \varepsilon_0\, g_T \tag{3.9}$$

and

$$C_{II} = 2k_{BCB}\varepsilon_0\, G_T + k_{BCB}\varepsilon_0 NL\frac{t}{W} = 2k_{BCB}\varepsilon_0\, G_T + k_{BCB}\varepsilon_0\, g_T \tag{3.10}$$

where g_T=NLt/W is the thickness geometry factor depending on the geometrical features of the IDC. Solving equations (3.9) and (3.10) for k_{BCB} yields:

$$k_{BCB} = \frac{C_{II}}{2\varepsilon_0 g_T}\left\{\sqrt{\left(\frac{2C_I}{C_{II}}-1-\frac{\varepsilon_0 g_T}{C_{II}}\right)^2+\frac{4\varepsilon_0 g_T}{C_{II}}}-\left(\frac{2C_I}{C_{II}}-1-\frac{\varepsilon_0 g_T}{C_{II}}\right)\right\}. \tag{3.11}$$

Equation (3.11) was used to compensate for the thickness of the IDC fingers while equation (3.6) yielded the uncompensated data assuming a zero thickness (t=0) for the IDC fingers. In other words, equation (3.6) is the asymptotic form of the

equation (3.11) when $t \rightarrow 0$. The systematic accuracy of the extracted dielectric constant based on the above method is around 0.1 % as long as the IDC pitch is smaller than the dielectric layer thickness. This is shown in Figures 3.12 and 3.13 where the effect of top layer thickness on the dielectric constant is simulated similar to the simulation shown in Figure 3.8. Both uncompensated and compensated data are shown. Figure 3.12 shows the simulation results for IDCs with extremely thin fingers (t=0.004 μm), while in Figure 3.13 the finger thickness is assumed to be the same as in the fabricated IDCs (t=0.32 μm).

3.1.3.2. Experiment

An Agilent 4279A 1 MHz C-V meter [115] was used to measure the capacitance and dissipation factor of IDCs. This equipment uses the auto balancing bridge method, an accurate method for impedance measurement at low frequencies from 20 Hz to 110 MHz [116]. In this method, as shown in Figure 3.14, a sinusoidal test signal (usually at 1 MHz) is applied to the high (H_C, H_P) terminals and the current passing through the impedance under test (Z_X) is balanced with the current passing through a known resistor (R) to maintain a zero potential at low (L_C, L_P) terminals. With measurement of the voltage across Z_X and R, Z_X can be determined. A capacitance meter, such as 4279A, assumes Z_X to be an RC equivalent, and therefore, the resistance and capacitance can be determined from the real and imaginary parts of Z_X, respectively.

The four test leads (H_C, H_P, L_C, L_P) of 4279A can be used in a two- or four-terminal configuration to measure the capacitance and dissipation factor. We used a four-terminal configuration to minimize the errors associated with mismatches

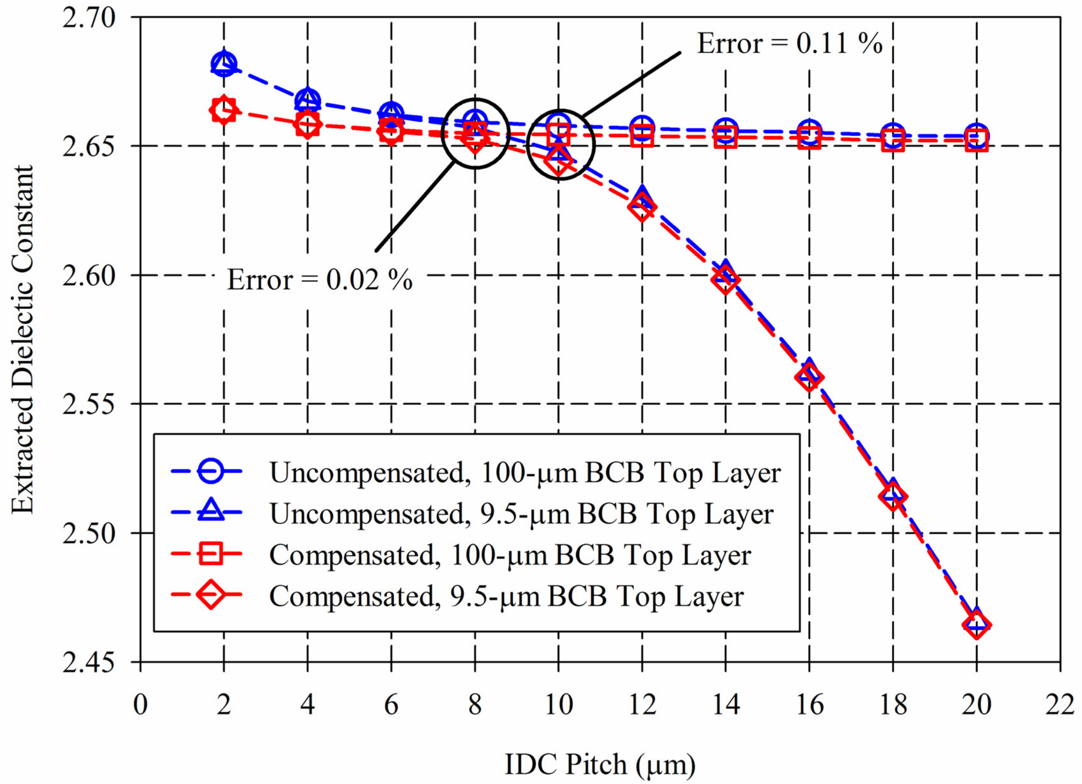

Figure 3.12. 2-dimensional finite-element numerical simulation of the extracted dielectric constant vs. pitch in a 500-finger IDC with 1-mm long fingers, showing the effect of BCB top layer finite thickness. The finger thickness was assumed to be 0.004 µm in this simulation. Both uncompensated and compensated data has been plotted to show the effect of finger thickness.

between the test leads, probes, and contact points (see Figure 3.15) [116]. In addition, a standard 1 m test cable designed for 4279A was used so that during the open and short compensation, the impedance of the test cable was accounted for. The amplitude of the test signal was set to 1 V (highest available to minimize the effect of noise). The C-V meter uses an averaging technique to eliminate random errors. The averaging time and the number of data points for averaging was set to medium mode and 256 (highest number available), respectively. For each set of devices, an open and a short compensation was performed. The open compensation takes into account any stray admittance (in parallel to the device under test) and the short compensation

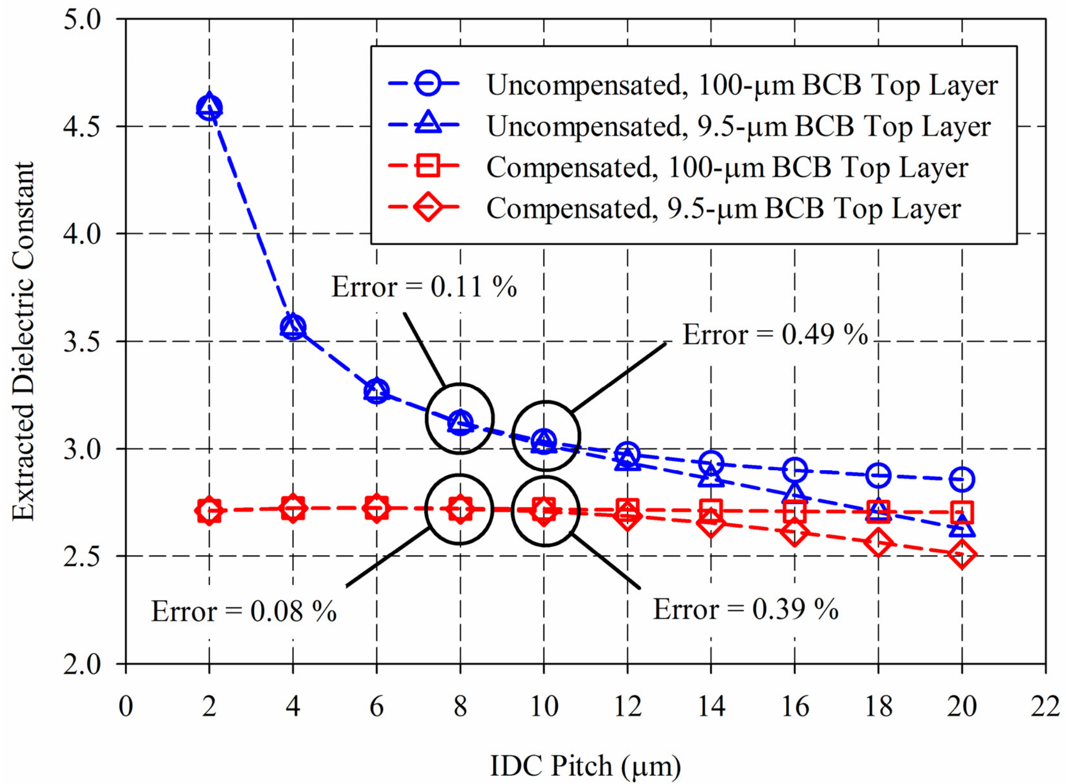

Figure 3.13. 2-dimensional finite-element numerical simulation of the extracted dielectric constant vs. pitch in a 500-finger IDC with 1-mm long fingers, showing the effect of BCB top layer finite thickness. The finger thickness was assumed to be 0.32 µm, which is the measured finger thickness in the fabricated IDCs.

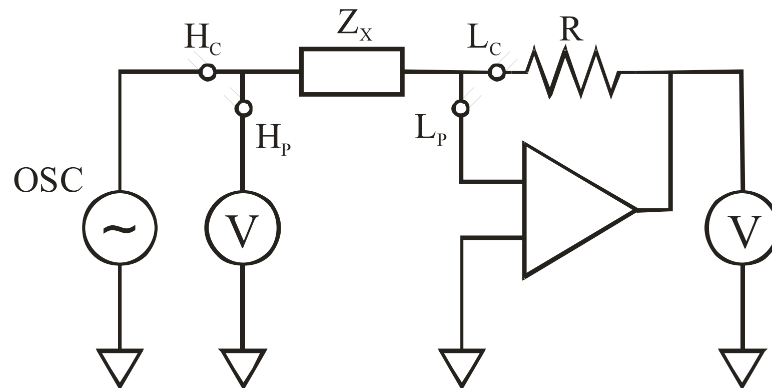

Figure 3.14. A simplified schematic of the auto balancing bridge circuit to measure impedance. A sinusoidal signal is applied to the high (H_C, H_P) terminals and the currents passing through Z_X and R are balanced so that a voltage of zero is maintained at the low (L_C, L_P) terminals. The actual circuit in practical instruments is much more sophisticated.

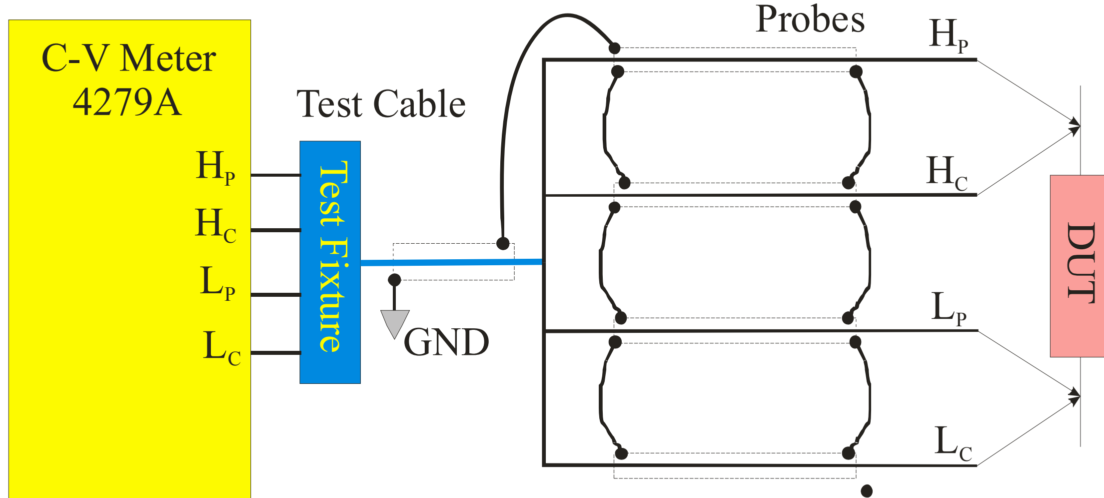

Figure 3.15. Four-terminal configuration for capacitance measurement.

considers any stray impedance (in series with the device under test). Under these circumstances, an accuracy of ±(0.07 % of reading + 0.03 % of full scale) is expected for capacitance measurement with 4279A. This will lead to an accuracy of about 7 fF (fF=10^{-15} F) for 1-mm long IDCs and about 70 fF for 10-mm long IDCs as long as dissipation factor (D) satisfies $D < 0.1$. For this reason, all data points with $D > 0.1$ were eliminated. Each capacitance data point presented here is the average of 12 measurements with a maximum standard deviation of 2.4 fF. Figure 3.16 shows the capacitance values measured at test steps I and II for 1-mm long IDCs. The measurements were performed in a relative humidity of 0.0 %RH at room temperature. Figure 3.17 shows the extracted dielectric constant of BCB before thickness compensation using equation (3.6) and after thickness compensation using equation (3.11). The nominal value (k=2.65) is plotted for comparison. As Figure 3.17 shows, the dielectric constant obtained from equation (3.6) depends on the pitch of the IDCs. This is due to neglecting the IDC finger thickness. On the other hand, the dielectric constant obtained from equation (3.11) is independent from the geometrical

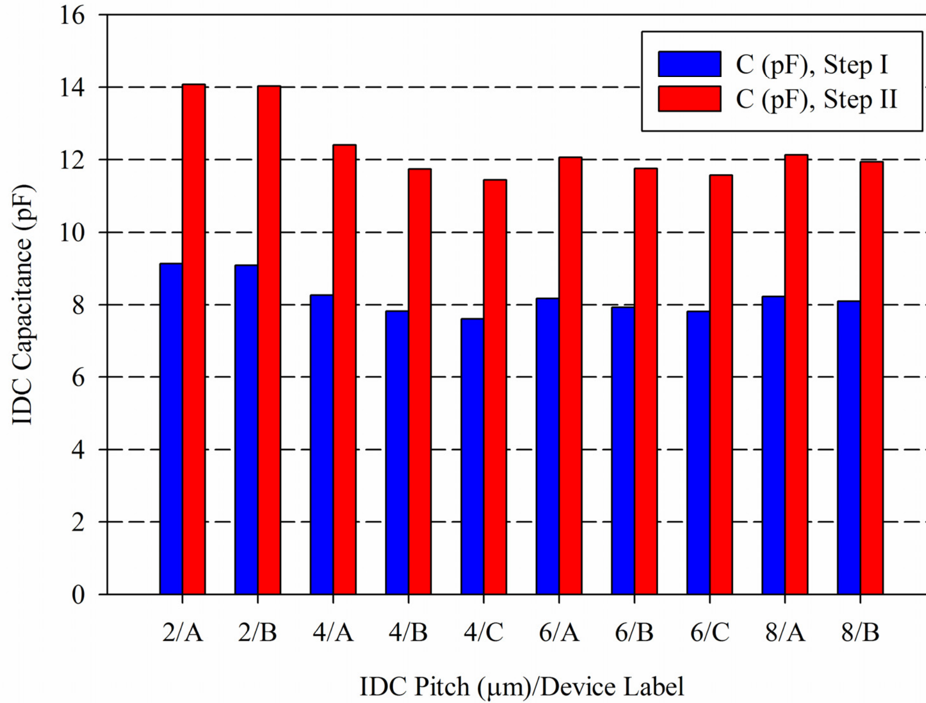

Figure 3.16. IDC Capacitance values measured in test steps I and II for 1-mm-long IDCs at 0.0 % relative humidity and room temperature.

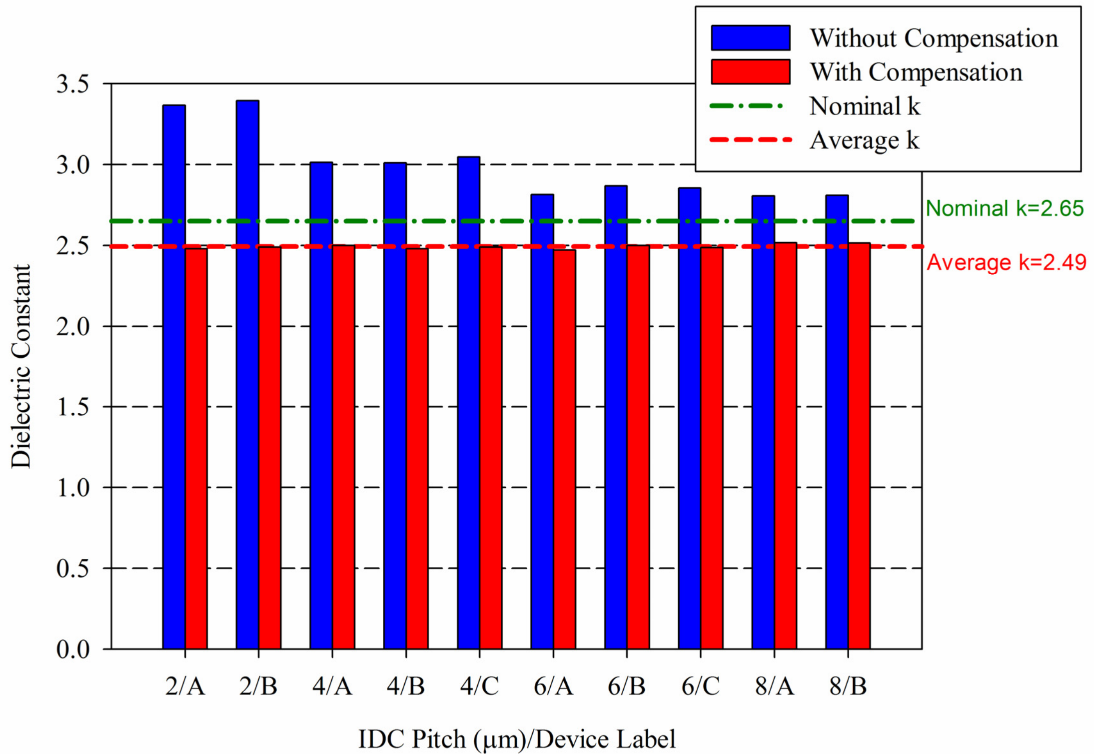

Figure 3.17. Dielectric constant of BCB before and after finger thickness compensation extracted from equations (3.6) and (3.11), respectively.

dimensions of the IDCs since the effect of thickness was compensated. An average value of 2.49 with a standard deviation of 1.5 % was obtained for BCB after compensation. However, the compensated values still differ from the nominal value of the dielectric constant by 6 % on average. A few factors may contribute to this difference. The compensation for the finger thickness is based on a perfectly fabricated IDC according to design specifications; however, there are process imperfections that can change the contribution of the finger thickness to the total capacitance of the IDC. In addition, the imperfections can change the local properties of the dielectric film leading to different values for the dielectric constant.

3.1.3.3. Effect of Moisture Uptake

The dielectric constant of water is quite high (around 80 at room temperature). This leads to a significant change in the dielectric constant of a polymer if the moisture absorption is appreciable. In order to measure the effect of moisture uptake on BCB film, the wafer was exposed to a humidity of 85 %RH at 85 °C for 2 hours inside the wafer chamber of the environmental test setup (see Figures 3.4 and 3.5). The capacitance of the IDCs was measured using the capacitance test setup. Figure 3.18 shows the values of capacitance before and after humidity stress. The change in the capacitance is due to the change in the dielectric constant as a result of moisture uptake in the BCB film. The measurements show that the dielectric constant increases by 1.2 % on average. As a result, the characteristics of BCB as a low-k material exhibit a small change following moisture uptake. In the long term, this is an important and useful feature that helps with the reliability of BCB-based micromachines.

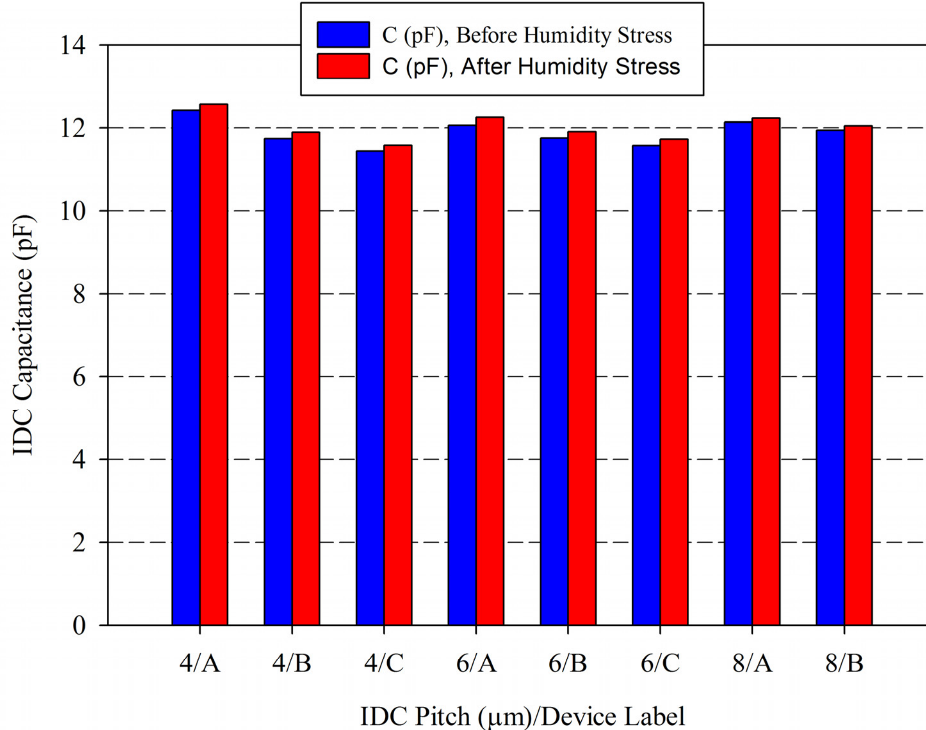

Figure 3.18. IDC Capacitance values before and after a humidity stress of 85 %RH at 85 °C for 2 hours.

3.1.4. Measurement of Current-Voltage Characteristics

In order to understand the behavior of the BCB electrostatic devices, the current-voltage (I-V) characteristic of the BCB film must be known. This is especially important in electrostatic MEMS where in some cases such as high-power devices (e.g. micromotors, etc) voltages up to hundreds of volts are used to drive these actuators. More importantly, if the operation region of the device is too close to the electrical breakdown of the BCB film, the likelihood of the device failure will be quite high, especially if the I-V characteristic is a function of environmental parameters such as humidity. In this section, we summarize the results of our study on the I-V characteristic of BCB films to address these issues. This study provides experimental data that can be used to predict the electrical behavior of BCB-based

devices and define the safe operation limits and conditions for these devices. The conducted experiments involved driving the IDCs to the electrical breakdown point and literally burning out the devices.

3.1.4.1 Theory

Most non-conducting solids (including dielectrics and semiconductors) exhibit a non-linear I-V characteristic (more prominent at high electric fields) so that as the electric field (or voltage) rises, the leakage current density (or current) increases more rapidly. At a certain critical point, the current becomes unstable and suddenly jumps to orders-of-magnitude larger values. At this point the solid basically acts like a conducting material. This phenomenon is called the *electrical breakdown*. When measuring the I-V characteristic of the solid, the breakdown can be observed under high electric fields. One important aspect of this phenomenon is that the properties of the solid do not recover if the electric field is removed after breakdown. This is a notion of an irreversible damage to the solid.

A great number of electrical failures in devices with dielectric components are caused by the *dielectric breakdown*. The associated critical field is called the *dielectric strength* and the associated critical voltage is called the *breakdown voltage*. The mechanism of dielectric breakdown can be a single or a combination of electric-field-driven processes. At normal electric fields, these processes are at equilibrium and as the field increases and passes the critical point, an inherent positive feedback dominates the equilibrium, resulting in an uncontrollable *runaway* of a quantity such as current density, temperature, or compressive stress [117]. In most cases, a structural defect in the solid provides a path with minimal resistance for current. In

some cases, the thermal instability of certain sites in the solid triggers a thermal runaway process that eventually leads to breakdown. For some solids, the I-V curve is modeled by one of the following exponential functions [118]:

$$I = Ae^{\alpha V} \tag{3.12}$$

$$I = Ae^{Be^{\alpha V}} \tag{3.13}$$

where A, B, and α are constants. The characteristic difference between the two models is that equation (3.13) features an extremely steep increase in the current at a rather lower voltage and as a result the breakdown voltage is defined more specifically while the transition in equation (3.12) is rather gradual and the electrical breakdown occurs over a higher, broader range of voltages. Figure 3.19 illustrates the different behavior of the two functions for $A=B=\alpha=1$. The units of voltage and current are defined by the units of A, B, and α.

3.1.4.2 Experiment

Figure 3.20 shows the circuit with which the I-V characteristic of IDCs was measured. The accuracy of the picoammeter was 0.1 pA. All signals, especially in the input of the picoammeter were shielded using coaxial cables to minimize the noise. Since the level of applied voltage was high, the accuracy of voltage measurement was not crucial. The test was carried out by stepping up the applied voltage in 10 V increments, holding the voltage at each step until the change in current was undetectable, and measuring the current. Note that applying a step voltage to a capacitor causes the current rises suddenly and then decays exponentially. Obviously, measuring the current right after applying the voltage leads to an incorrect data point. In order to eliminate this error, we performed the measurement after the current was

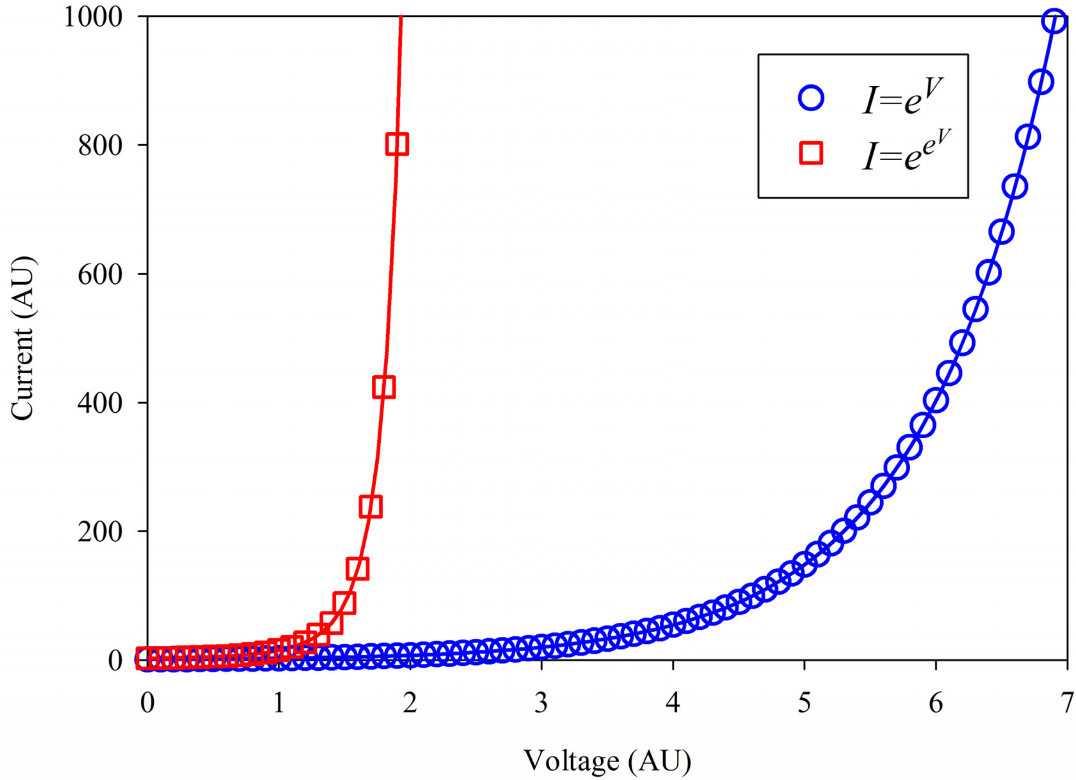

Figure 3.19. General form of two exponential functions used to describe the I-V characteristic of some solids (AU: arbitrary unit)

stabilized in each step. This cycle was repeated until the current started to rise suddenly. The current surge usually happened so fast that the device was permanently damaged (burned) due to excessive heat before the applied voltage was removed or the current-limit of the power supply was activated. Therefore, the last measured data point was one step right before the dielectric breakdown. The I-V characteristic was also measured after a humidity stress of 85 %RH at 85 °C. It should be noted that to ensure that the BCB film is completely dry for tests before humidity stress, the sample were cured in dry nitrogen flow at 200 °C for 2 hours.

Figure 3.21 shows the measured results for 1-mm-long IDCs with 2-µm and 3-µm finger width/spacing before and after the humidity stress. Exponential curve fits, similar to equations (3.12) and (3.13), are also shown on the plots. As it is seen,

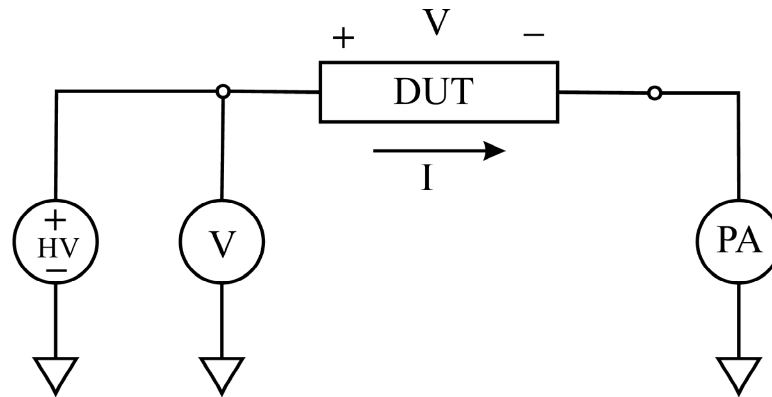

Figure 3.20. Circuit for measurement of I-V characteristic of BCB films. The voltage is applied to the device under test (DUT) using a high voltage (HV) power supply. The voltage is measured by a digital multimeter (V), and the current is measured by a picoammeter (PA). The internal current limit of the HV power supply limits the current in case of breakdown.

both models agree very well with the experimental results. In order to quantitatively measure the accuracy of a curve fit, it is common to use the coefficient of determination (R^2), which is given for each curve fit in Figure 3.21. A R^2 closer to one means a better curve fit. By comparing R^2 in Figure 3.21, it is evident that equation (3.13) provides a more accurate model for the I-V characteristic of BCB films.

As Figure 3.21 shows, the breakdown voltage of the dry BCB film is about 450 V for 2-μm-finger IDC and about 960 V for 3-μm-finger IDC. This means that the dielectric strength of the BCB film before the humidity stress is approximately in the range of 225 V/μm to 320 V/μm, which is comparable to the nominal value of 300 V/μm from Table 1.4.

3.1.4.3 Effect of Moisture Uptake

As shown in Figure 3.21, after the humidity stress the breakdown voltage drops drastically to about 200 V for 2-μm-finger IDCs and to about 540 V for 3-μm-finger IDCs, resulting in a dielectric strength approximately in the range of 100 V/μm

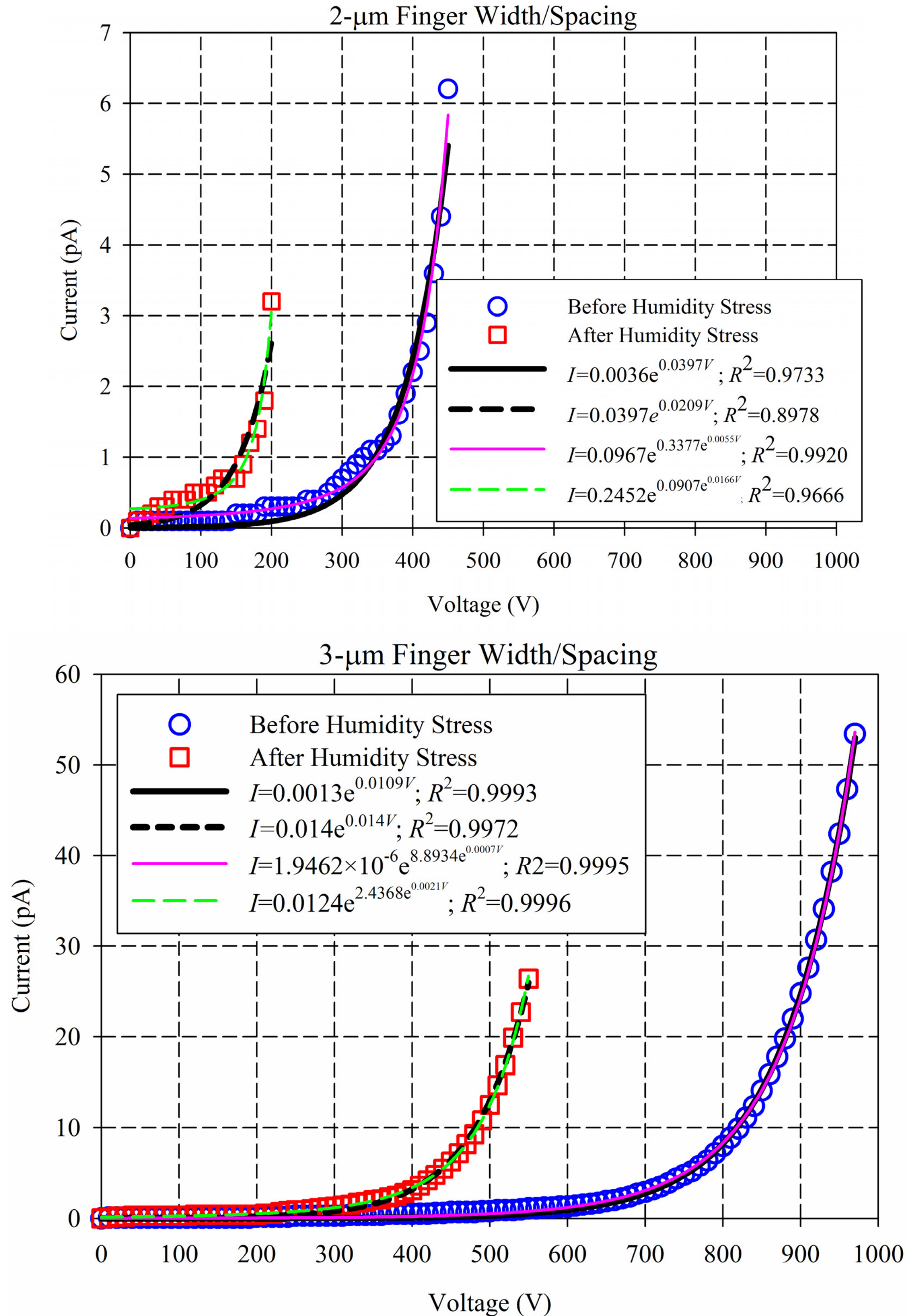

Figure 3.21. I-V characteristics of 1-mm-long IDCs before and after humidity stress with exponential curve fitting based on equations (3.12) and (3.13) for 2-μm and 3-μm finger width/spacing. R^2 is the coefficient of determination.

to 180 V/μm, which is close to half of the nominal value (300 V/μm from Table 1.4). The leakage current depends on the applied voltage and finger spacing. The leakage current of dry BCB film ranges from 0.1 pA to 6.2 pA for 2-μm-finger IDCs and from 0.1 pA to 53.4 pA for 3-μm-finger IDCs. After the humidity stress, the increase in the leakage current can be as big as one order of magnitude, depending on the applied voltage. As these measurements show, the I-V characteristic of BCB film depends on the geometry of the device under test and absorption of moisture. We believe that the size and the structure of the device are important factors in the likelihood of electrical failure since these factors contribute to the nature and number of defects and imperfections in the dielectric film. We also believe that moisture helps to form or enhance the conducting paths inside the dielectric material so that even with small moisture absorption the dielectric strength of the dielectric film decreases appreciably. As seen in Figure 3.21, the leakage current is also different by one order of magnitude for different finger spacings. This is because the IDC with larger finger spacing fails at higher voltages where the resistance of the dielectric film drops even more, leading to a higher leakage current.

The drastic change in the I-V characteristic of BCB after moisture uptake can lead to reliability issues in BCB-based micromachines, specifically limitation of the maximum operating voltage and occurrence of the early breakdown in humid environment. These results, however, provide designers with specific knowledge to design and fabricate reliable micromachines using BCB polymers.

3.2. Chemical Mechanical Planarization of Benzocyclobutene Polymers

The surface of the wafer is globally planarized during the EBiS process, although BCB polymers are excellent planarizers with a degree of planarization (DOP) of about 95 % when coated over isolated, shallow trenches [77]. This is especially necessary when dealing with deep, wide trenches. In this work, the planarization of BCB polymers has been achieved using CMP, which is the de facto standard for global planarization in integrated circuit chip fabrication today [119].

3.2.1. Principles of Chemical Mechanical Characterization

CMP is a planarization/polishing method that uses a combination of mechanical abrasion and chemical etching to physically remove material from places of high topography and flatten the wafer surface. In all experiments presented here, a 6EC CMP tool from Strasbaugh (San Luis Obispo, CA) was used for polishing the wafers. The 6EC is shown in Figure 3.22.

The output parameters that are commonly used to benchmark a CMP process are removal rate, removal uniformity, removal selectivity, and surface topography of the polished film. These parameters are the result of mechanical and chemical interaction at the interface of three major components of a CMP process: polishing pad, polishing slurry, and wafer. These interactions take place inside the polishing area of the 6EC shown in Figure 3.23. The basic operation of the tool is as follows: The wafer is held onto a wafer chuck inside the wafer carrier initially using vacuum suction. While polishing platen and the wafer carrier rotate at user-defined speeds and

a user-defined down force pressure is applied to the wafer, it is brought to contact with the polishing pad. The polishing slurry pours onto the polishing pad at a user-

Figure 3.22. Strasbaugh 6EC CMP tool. The main unit, including polishing area, control panels, and touch-screen computer is shown.

Figure 3.23. The polishing area of the Strasbaugh 6EC CMP tool. Polishing platen and pad, wafer carrier, polishing arm, and slurry dispenser can be seen. This tool has a 4” wafer chuck inside the wafer carrier.

defined flow rate through the slurry dispenser. There are several variables that affect these interactions and control the output parameters, making the CMP process a complicated phenomenon to analyze and model. Table 3.2 summarizes the major control parameters and the affected output parameters in a generic CMP process [120].

Table 3.2. CMP Control and Output Parameters

Control Parameter	**Output Parameter**
Down Force Pressure	RR[a], RU[b], RS[c]
Wafer Carrier Rotation Speed	RR, RU, RS
Platen Rotation Speed	RR, RU, RS
Slurry Chemistry	RR, RS, ST[d]
Slurry Abrasive (Type, Size, Percent)	RR, RS, ST
Pad Hardness	RR, RU, RS, ST
Pad Porosity	RU
Wafer Carrier Film Hardness	RU

[a] RR: Removal Rate; [b] RU: Removal Uniformity; [c] RS: Removal Selectivity; [d] ST: Surface Topography.

The control parameters of CMP are not limited to those listed in Table 3.2. For instance, pad conditioning can impact the polishing results. Some CMP tools (including 6EC) allow the user to apply a back pressure (positive or negative) on the wafer to compensate for the wafer bow or apply a pressure to the retaining ring to adjust the polish of the wafer edge. Platen temperature, slurry flow rate, and polishing time also affect the output parameters. The most important control parameters are down force pressure, platen rotation speed, and wafer carrier rotation speed. These parameters determine the removal rate of the film based on the empirical Preston Equation [121]:

$$RR = K_p P v \tag{3.14}$$

where RR is the removal rate, v is the linear velocity of the platen relative to the wafer, P is the down force pressure pressing the wafer onto the pad, and K_p is the Preston coefficient. The Preston coefficient is a function of the mechanical and chemical properties of the polishing pad, slurry, and the film being polished. Considering only the mechanical properties of the film, it has been shown that the Preston coefficient is inversely proportional to the Young's modulus of the film [122]:

$$K_p = \frac{1}{2E} \tag{3.15}$$

where E is the Young's modulus of the film being polished. It has also been shown that equation (3.14) applies to hard-pad CMP systems more accurately while RR is proportional to $P^{1.5}$ for soft-pad CMP systems [123]. More complete and accurate CMP models can be found in [124-130].

CMP of polymer materials such as BCB polymers is more challenging than inorganic materials such as silicon dioxide and metals. Some specific properties of BCB polymers that result in observation of distinct phenomena during CMP process are: (i) BCB polymers are known to have hydrophobic surfaces [131], resulting in low surface reactivity and low removal rate; (ii) The hardness of most polymers, including BCB, is lower than that of inorganic materials, leading to high levels of scratching and post-CMP defects; (iii) The lower hardness of BCB polymers can also result in embedded abrasive particles in the polished film; (iv) The level of polymer cross-linking (polymerization) in BCB is a function of cure temperature and time, therefore, the hardness and surface reactivity of BCB polymers, and as a result, the removal rate strongly depend on cure temperature and time.

3.2.2. Characterization of Chemical Mechanical Planarization

Considering the challenges in planarization of BCB polymers, it is important to understand the behavior of blanket BCB polymer films in CMP process before characterizing the CMP process for more complicated structures such as EBiS islands. Furthermore, such characterization can help with the design and optimization of the EBiS process. For these reasons, we conducted a series of experiments to study and characterize the CMP process for BCB polymer films. In this characterization, we were mainly interested in the difference between parameters of uncured and cured films, such as removal rate, non-uniformity, and surface topography.

The physical properties of dry-etch and photosensitive BCB polymers, as Table 1.4 shows, have minor differences. Therefore, the characterization samples were prepared with the dry-etch (non-photosensitive) BCB polymer (Cyclotene 3022-

63) instead of the photosensitive BCB polymer (Cyclotene 4026-46), which is used in the fabrication of the micromotor. All samples were 4” silicon wafers and prepared in the following manner. Each wafer was dehydrated at 130 °C for 10 minutes on a hotplate. AP3000, an adhesion promoter developed for Cyclotene by Dow Chemical, was dispensed and spun onto the wafer at 3000 rpm for 30 s. Next, Cyclotene 3022-63 was dispensed and spun onto the wafer, first at 500 rpm for 8 s and then, at 5000 rpm for 30 s. The sample was then baked at 85 °C for 150 s on hotplate. This bake step does not initiate the polymerization but can drive out most of the remaining solvent. Several wafers were prepared and cured at different temperatures to study the effect of cure temperature on CMP parameters.

All wafers were polished in our 6EC CMP tool with a k-grooved IC-1000 pad stacked on a SUBA IV pad from Rohm and Haas Electronic Materials (Phoenix, AZ). The specifications of the slurries used in this research, MSW2000A from Rohm and Haas Electronic Materials and ILD1300 from Nitta Haas Incorporated (Osaka, Japan), are listed in Table 3.3. Table 3.4 shows the polishing and pad conditioning parameters of the two CMP recipes that we used for polishing wafers.

Initial polishing experiments were conducted using MSW2000A slurry with both recipes I and II. Figure 3.24 shows AFM scans of soft-cured (cured at 210 °C for 40 minutes) BCB polymer surface before and after CMP with MSW2000A slurry using recipes I and II. Recipe I uses lower down force pressure and rotation speed, yielding lower removal rate but better uniformity, less defects, and better surface quality. Recipe II uses higher pressure and rotation speed, yielding higher removal

rate but less uniformity, more scratches, and higher surface roughness. However, both recipes resulted in substantial embedded abrasive particles in the film.

Table 3.5 summarizes the quantitative data before and after CMP with each recipe. As seen in Table 3.5, the removal rate of the cured film is very low but the non-uniformity and surface roughness increases dramatically after CMP. This is most likely because the removal of BCB with MSW2000A results from mechanical abrasion rather than chemical etching. This is expected because, as Table 3.3 shows, the percentage of abrasive particles in MSW2000A is relatively high, and the solution is acidic. We have observed that BCB polymers exhibit more resistance to acids than bases. It has been experimentally shown that adding surface-active agents (surfactants) such as Triton-X 100 to some slurries can improve the removal rate

Table 3.3. Specifications of CMP Slurries

Specifications	**MSW2000A**	**ILD1300**
Primary Target Material	Tungsten	SiO_2
Abrasive Material	Alumina	Silica
Median Diameter of Particles	170 nm	175 nm
Percentage of Abrasives	28 %	13 %
Solution	Proprietary	NH_4OH
pH (at 25 °C)	3.9	10.75
Specific Gravity (at 25 °C)	1.25 g/cm^3	1.07 g/cm^3
Manufacturer	Rohm and Haas, USA	Nitta Haas, Japan

Table 3.4. CMP Recipes

	Input Parameters	Recipe I	Recipe II
Polishing	Down Force Pressure (psi)	2	3
	Platen Rotation Speed (rpm)	34	120
	Carrier Rotation Speed (rpm)	27	114
	Backside Pressure (psi)	0	0
	Slurry Flow Rate (ml/min)	250	250
Pad Conditioning	Sweep Type	in-situ	
	Sweep Cycle (sweeps/cycles)	3	
	Platen Rotation Speed (rpm)	30	
	Carrier Rotation Speed (rpm)	25	
	Stroke Pause (s)	30	
	Slurry Flow Rate (ml/min)	75	

[131]. An alternative approach in some applications is to perform CMP on uncured or partially cured BCB polymers because the lower level of cross-linking can provide a higher removal rate. Furthermore, since BCB exhibits poor chemical resistance to bases [132], slurries with high pH, such as ILD1300, can potentially produce higher removal rates. Another advantage of ILD1300 over MSW2000A is its lower percentage of abrasive particles, which reduces the post-CMP scratches and embedded particles. Most experiments and processes in this study were conducted using ILD1300 and Recipe I because they produced the overall best results.

In order to study the performance of ILD1300 slurry and the effect of cure temperature, three samples were prepared. One wafer was left uncured and two other

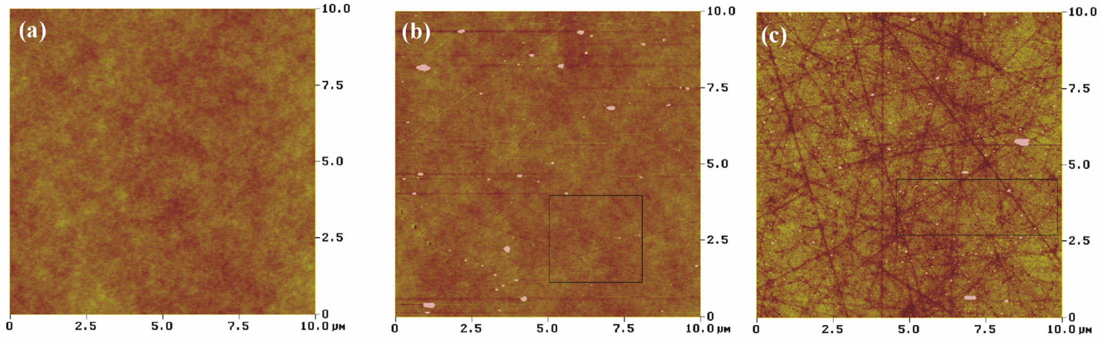

Figure 3.24. AFM scans of BCB polymer surface cured at 210 ºC showing the effect of CMP with MSW2000A slurry: (a) before CMP, (b) after CMP with recipe I, and (c) after CMP with recipe II.

Table 3.5. Specifications of Soft-cured BCB Film before and after CMP with MSW2000A Slurry and Recipes I and II

Parameters	**Pre-CMP**	**Recipe I**	**Recipe II**
Polishing Time	N/A	120 s	120 s
Non-uniformity	0.3 %	0.8 %	1.8 %
Removal Rate	N/A	7 nm/min	45 nm/min
P-P Roughness	41 Å	1383 Å	1511 Å
Mean Roughness	4 Å	7 Å	12 Å
RMS Roughness	5 Å	29 Å	33 Å

wafers were cured at two different temperatures below and above 200 °C, which is the activation temperature of BCB polymerization [79, 80]. The exact cure temperatures are listed in Table 3.6. Note that the higher cure temperature is close to the standard hard-cure (250 °C) temperature recommended for BCB polymers.

Figure 3.25 shows AFM scans of the uncured and cured BCB films before and after CMP using recipe I with ILD1300 slurry. With the exception of the uncured BCB, It is clear that the embedded particle density after CMP is less compared to MSW2000A slurry (see Figure 3.24). The scratch density is much higher in Figure 3.25(b) because the BCB is cured at a lower temperature (188 °C) compared to the soft-cure or hard-cure temperatures. As shown in Figure 3.25(c), the embedded particle density is high in case of the uncured BCB. Comparing Figures 3.25(a),

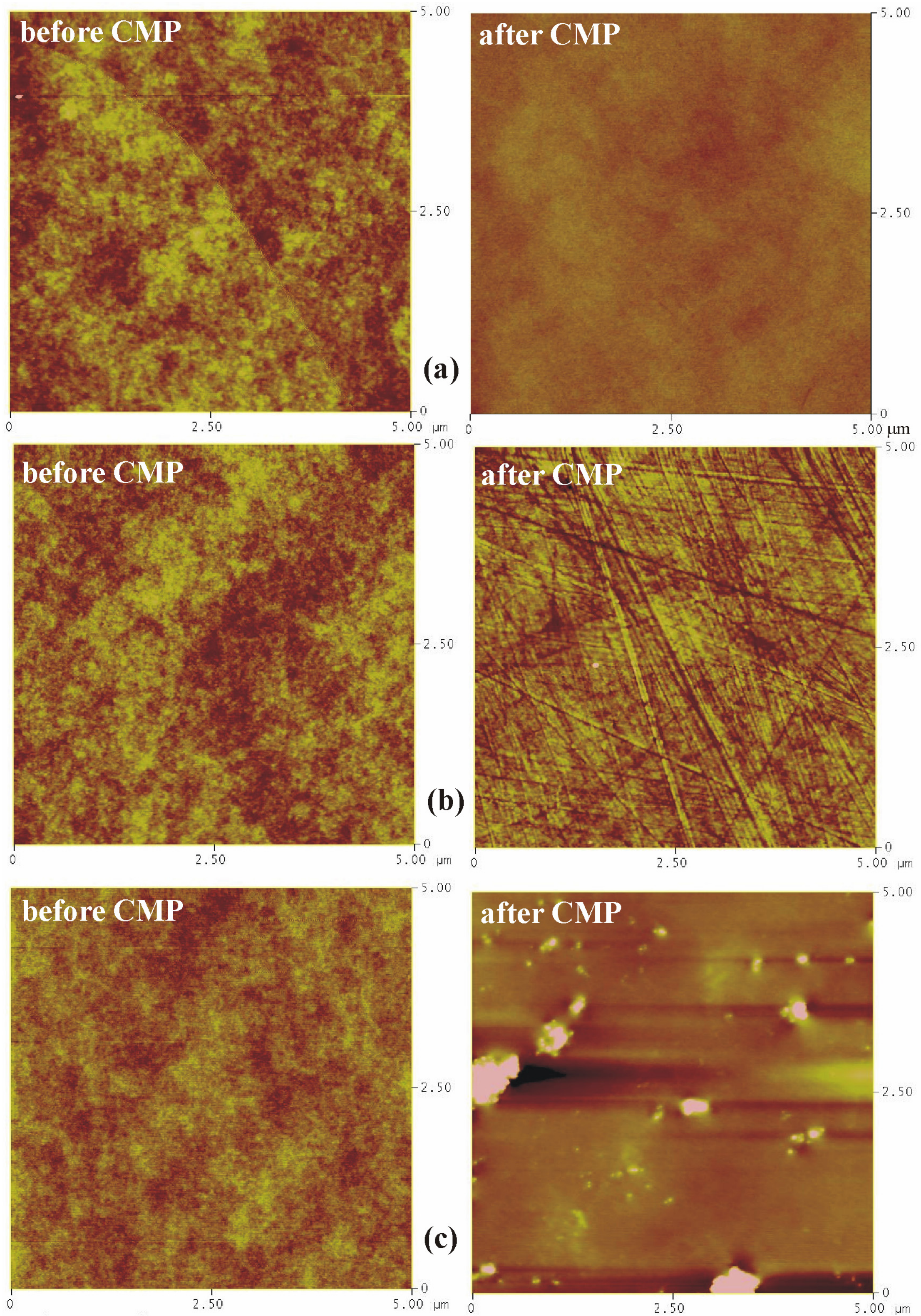

Figure 3.25. AFM scans of BCB polymer surface showing the effect of CMP using recipe I with ILD1300 slurry: (a) cured at 255 °C, (b) cured at 188 °C, and (c) uncured. Quantitative data is shown in Table 3.6.

Table 3.6. CMP of BCB Polymer Cured at Different Temperatures using ILD1300 Slurry and Recipe I

Parameters	**Wafer #1 (Uncured)**		**Wafer #2 (188 °C, 50 min)**		**Wafer #3 (255 °C, 70 min)**	
	Pre	Post	Pre	Post	Pre	Post
Mean Thickness (μm)	10.43	6.46	9.36	9.33	9.31	9.30
Non-Uniformity (%)	1.1	3.3	0.9	1.4	0.6	0.5
Polishing Time (s)	N/A	65	N/A	305	N/A	305
Removal Rate (nm/min)	N/A	3663	N/A	6.8	N/A	3.2
P-P Roughness (Å)	32	1884	41	661	58	44
Mean Roughness (Å)	3	31	4	6	4	1
RMS Roughness (Å)	3	67	5	13	5	2

2.25(b), and 2.25(c) reveals that the scratch and embedded particle density is a function of cure temperature. Table 3.6 summarizes the quantitative data before and after CMP. The removal rate of BCB is extremely low at temperatures above 200 °C and increases as the cure temperature decreases (although it is still very low at 188 °C cure temperature). The removal rate is quite high for uncured BCB. The surface roughness of the film decreases after CMP for cure temperatures above 200 °C while it increases as the cure temperature goes below 200 °C. This shows that the CMP characteristics of BCB film are determined by the cure temperature, so that by controlling the level of polymerization through cure temperature, the output parameters of CMP process can be adjusted. In a related study conducted in our group, it has been shown that the removal rate of BCB film exhibits a drastic change at a cure temperature between 140 °C and 160 °C [133]. This suggests that the polymerization is initiated at a much lower temperature around 150 °C although the activation temperature of BCB is around 200 °C.

3.3. Overview of Fabrication Process

The B-LVCM consists of three separate parts: silicon stator, silicon slider, and stainless-steel microballs. The microballs are available off-the-shelf in different grades. The stator and the slider were fabricated on separate silicon wafers. Fabrication of the B-LVCM consists of 48 process steps, including eight photolithography steps as shown in Table 3.7 and requires 8 chrome photomasks. The fabrication process flow is a combination of several unit processes, shown in Table 3.8. These unit processes were developed, characterized, and fine-tuned during the course of this research.

Table 3.7. Photolithography Levels for Fabrication of the Stator and the Slider

Part	Mask Level	Mask Tone	Fabrication
Stator	1	Dark Field	Silicon Pits (EBiS)
	2	Dark Field	Insulating BCB (1st BCB, EBiS)
	3	Clear Field	Interconnects (1st Metal)
	4	Dark Field	ILD BCB / Vias (2nd BCB)
	5	Clear Field	Electrodes (2nd Metal)
	6	Dark Field	Passivating BCB / Pads (3rd BCB)
	7	Dark Field	Trenches (Microball Housings)
Slider	8	Dark Field	Poles/Trenches (Microball Housings)

3.4. Embedded Benzocyclobutene in Silicon Process

Integration of BCB polymer films with conventional MEMS processes such as silicon bulk micromachining is not a trivial task, mainly because the polymer can not withstand the harsh condition of some chemical environments, especially hot potassium hydroxide (KOH). The poor adhesion of the BCB polymers to metals and other inorganic films makes the integration even more challenging. Thin BCB polymer film (~1 μm) has been successfully integrated with micromachined silicon v-

Table 3.8. Unit processes used in fabrication of the B-LVCM

Process	Target Material	Mask Level	Details
Dehydration	Wafer	All	Hotplate, 130 °C/30 min
Clean	Wafer	1	Standard RCA Clean
Photolithography (Positive, 6 μm)	AZ 9245	1	Spin: 1750 rpm/5 s + 3000 rpm/40 s, Soft Bake: Hotplate, 110 °C/90 s, Exposure: 300 mJ/cm^2, Develop: AZ 400K 1:3, 180 s
Photolithography (Positive, 10 μm)	AZ 9245	7, 8	Spin: 300 rpm/5 s + 1000 rpm/40 s, Soft Bake: Hotplate, 110 °C/120 s, Exposure: 720 mJ/cm^2, Develop: AZ 400K 1:3, 180 s
Photolithography (Image Reversal)	AZ 5214E	3, 5	Spin: 3000 rpm/30 s, Soft Bake: Hotplate, 100 °C/60 s, Exposure: 40 mJ/cm^2, Post-Exp Bake: Hotplate, 125 °C/45 s, Flood Exposure: 1200 mJ/cm^2, Develop: AZ 400K 1:6, 120 s
Photolithography (BCB, Thick)	Cyclotene 4026-46	2	Modified Manufacturer's Recipe
Photolithography (BCB, Thin)	Cyclotene 4024-40	4, 6	Modified Manufacturer's Recipe
Resist Strip	Resist	1, 7, 8	ALEG-310, 80°C/15min
Partial Cure	BCB	2	Box Furnace, 170 °C/50 min
Soft Cure	BCB	6	Box Furnace, 210 °C/50 min
Hard Cure	BCB	7	Box Furnace, 250 °C/60 min
RIE (Resist Descum)	Resist	1, 3, 5, 7, 8	Trion Plasma Etcher, 200 mT/50 W/30 s, O_2=50 sccm
RIE (BCB Descum)	BCB	2, 4, 6	Trion Plasma Etcher, 250 mT/100 W/30 s, O_2=90 sccm, CF_4=10 sccm
DRIE	Silicon	1, 7, 8	STS Plasma Etcher
CMP	BCB	2	Strasbaugh 6EC, ILD1300 Slurry
Sputtering	Chromium (Cr) Gold (Au)	3, 5	AJA Magnetron Sputtering 5 mT/50 W /8 min (Cr)/20 min (Au)
Lift-off	Cr/Au	3, 5	Ultrasonic Bath, Acetone (60 min) + DI Water (60 min)

grooves [132], while integration of thick BCB polymer films is still facing the challenge of polymer undercut during silicon etching.

We have developed a novel technique called embedded BCB in silicon (EBiS) [134] to take advantage of the unique features of BCB polymer films for electrical

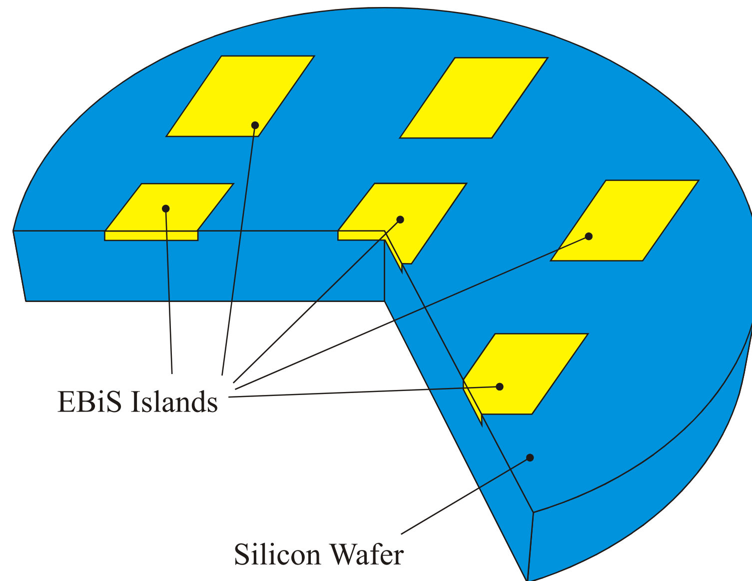

Figure 3.26. A schematic of a silicon wafer with several planarized embedded BCB in silicon (EBiS) islands

and thermal isolation, and to integrate these films with other microfabricated structures and devices. The objective of EBiS process is to develop planarized isolated islands of thick BCB polymer films embedded in a silicon substrate. These islands act as the insulating beds for active areas, where subsequent devices and structures are fabricated. As an example, one application area of EBiS is bottom-drive electrostatic micromotors, where the electrodes and interconnects of the stator are insulated from the substrate using EBiS islands.

A schematic of a silicon wafer after development of EBiS islands is shown in Figure 3.26. The EBiS process is an alternative to the conventional method where a thick dielectric film such as silicon dioxide is deposited across the wafer and subsequent layers and structures are fabricated on top of the film. There are several advantages for the EBiS process over the conventional method: (i) the overall wafer bow is reduced because the residual stress is limited to small embedded islands compared to a blanket film across the wafer; (ii) the polymer film and the associated

problems such as etching difficulties, adhesion, etc. in areas outside the islands are minimized; (iii) the subsequent fabrication processes are less prone to fabrication defects, leading to higher yields because the islands are highly planarized; (iv) since the polymer layer is embedded in the substrate, the adhesion of the polymer to the substrate is improved compared to blanket film; (v) if metal films are present, the overall adhesion of the metal films to the substrate is improved by limiting the polymer to a small area on the substrate; (iv) in case of etching silicon v-grooves in hot KOH, the polymer can be completely masked with a metal layer to prevent undercut.

The EBiS process is adopted from thick buried oxide in silicon (TBOS) process [69]. TBOS is a fabrication process developed to create isolated islands of plasma-enhanced chemical vapor deposited (PECVD) silicon dioxide to reduce the overall wafer bow for subsequent wafer bonding. EBiS, however, enables the incorporation of spin-on, thick BCB polymer films in silicon substrate, leading to excellent electrical and thermal isolation, lower electrical energy loss, lower residual stress and wafer bow, and easier fabrication and process integration.

3.4.1. EBiS Fabrication Process

EBiS process uses standard microfabrication tools and techniques including photolithography, reactive ion etching (RIE) or deep reactive ion etching (DRIE), and CMP. The process consists of consecutive BCB deposition, patterning, and planarization steps until the desired step height reduction (SHR) is achieved on the wafer. The number of deposition and planarization steps depends on the desired size of the BCB islands, the desired thickness of the BCB polymer film, and the viscosity

of the Cyclotene solution. For instance, large island areas (e.g. 5 mm × 10 mm and larger), and a 25-µm thick BCB polymer film are required to achieve good electrical isolation in the electrostatic micromotor. In this case, two to three layers of Cyclotene 4026-46 are needed to completely fill the islands.

Figure 3.27 shows the main steps in EBiS process. Starting from a silicon wafer, the island areas are patterned in photoresist and etched in silicon using conventional photolithography and RIE or DRIE as seen in Figure 3.27(a). Silicon is etched as deep as required for the desired isolation (we have used RIE to etch 12-µm deep trenches and DRIE to etch 25-µm trenches on different test samples). The photoresist etch mask is then stripped off the wafer. Next, an adhesion promoter for BCB polymers, AP3000 is dispensed and spun onto the wafer. Photosensitive BCB is then dispensed, spun on and patterned over the etched islands as seen in Figure 3.27(b). The BCB pattern area is chosen to be 100 µm larger on each side than the island area. This ensures that no void is developed inside the BCB islands. However, a BCB ridge forms around each island and needs to be removed. A short descumming in O2/CF4 plasma is also performed to remove any remaining BCB residue after development. At this point the BCB is still uncured.

Planarization is the most important step in EBiS process. A short CMP is performed to remove the uncured BCB ridges around the islands as shown in Figure 3.27(c) and leaves a depression over the island area. Figures 3.28 and 3.29 show the optical micrographs and optical profilometry graphs of BCB islands before and after CMP that illustrate the removal of the 100-µm wide BCB ridges. The uncured BCB ridges, as shown in Figures 3.28(a) and 3.29(a), were completely removed after 5

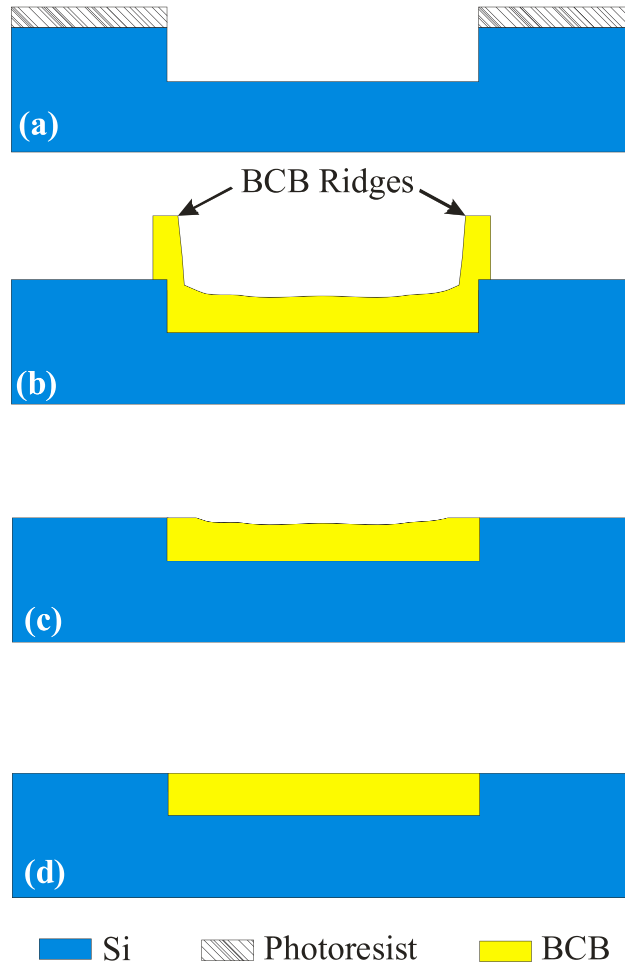

Figure 3.27. Major fabrication steps of EBiS process: (a) DRIE of silicon to form islands, (b) spin-casting and patterning the first layer of photosensitive BCB polymer, (c) planarizing the BCB islands with CMP, and (d) repeat steps b and c for the second layer of photosensitive BCB polymer with partial-curing to fill and planarize the EBiS island.

minutes of CMP (recipe I with ILD1300 slurry; see tables 3.3 and 3.4). The average removal rate of the uncured BCB ridges was found to be higher than 1.6 μm/min. The exact removal rate could not be determined because the ridges might have been completely removed within a shorter polishing time. Considering the removal rate of the uncured blanket BCB film, as discussed in section 3.2.2, about 2 to 3 minutes of polishing time should have been enough to remove the ridges.

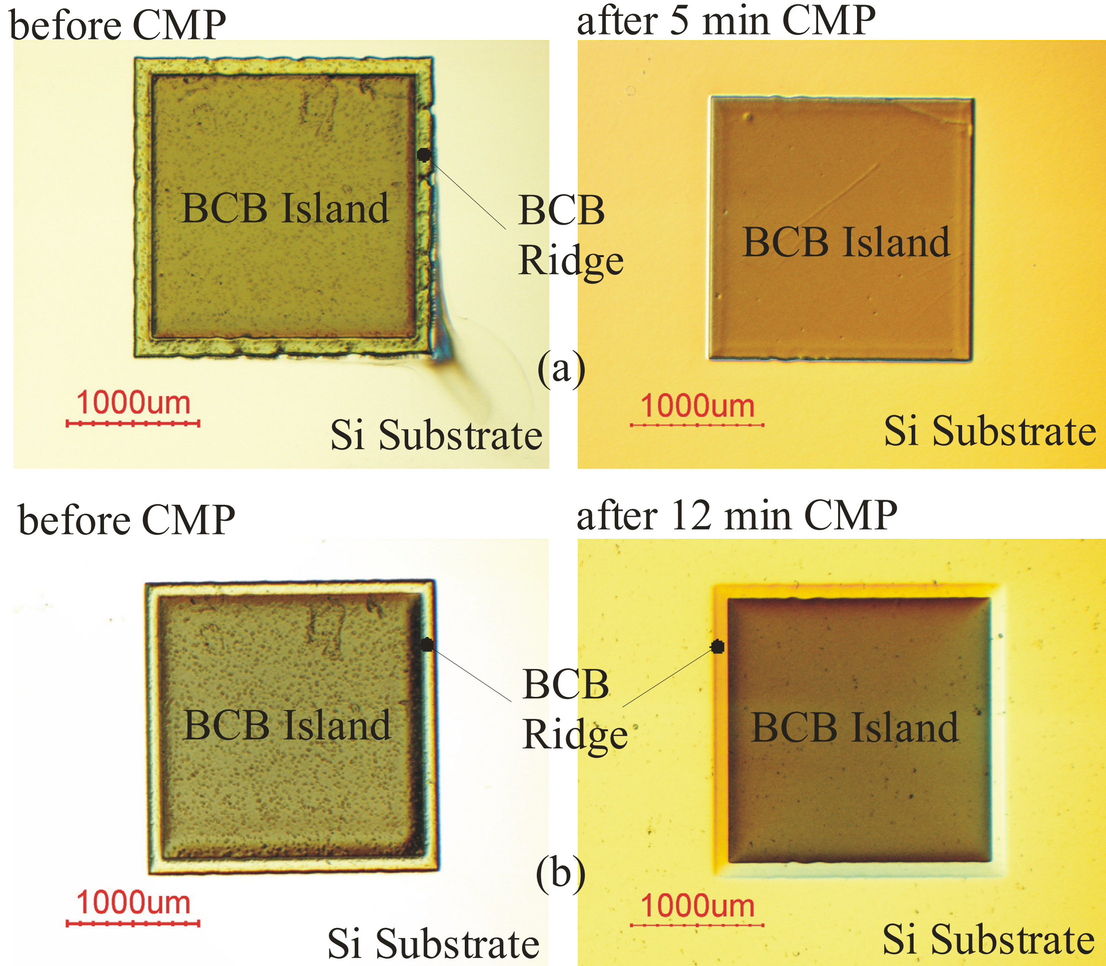

Figure 3.28. Optical micrographs of two identical 2 mm × 2 mm EBiS islands on two samples before and after CMP with ILD1300 slurry and recipe I: (a) uncured, and (b) cured at 210 °C (standard soft cure).

In order to fill the depression, the second BCB layer is spun on and patterned. At this point, the films should be partially cured at a temperature close to the activation temperature of BCB polymerization. The curing helps with cross-linking of the BCB layers. If the cure temperature is too low, the top BCB layer will be peeled off during the CMP. On the other hand, if the cure temperature is too high, the CMP removal rate of the BCB ridges will be too low. However, since a ridge is mechanically weaker than a blanket film, the removal rate of cured BCB ridges is

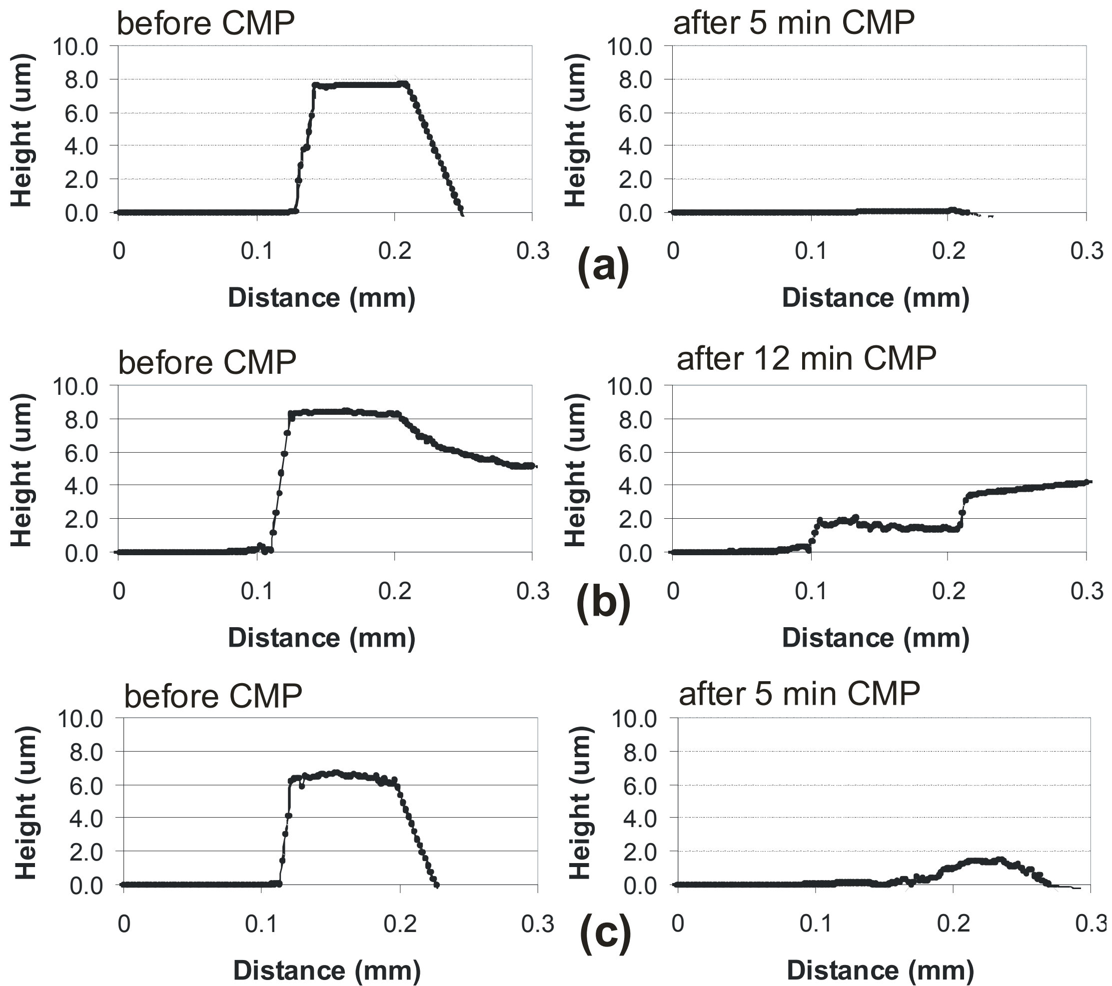

Figure 3.29. Optical profiles of BCB ridges around three identical EBiS islands on three samples before and after CMP with ILD1300 slurry and recipe I: (a) uncured, (b) cured at 200 °C, and (c) cured at 210 °C (standard soft cure).

initially much higher than the removal rate of blanket films. As Figures 3.28(b) and 3.29(b) show, the soft-cured BCB ridges were not completely removed after 12 minutes of CMP (recipe I with ILD1300 slurry; see Tables 3.3 and 3.4). The average removal rate was measured to be 0.3 μm/min. To further increase the removal rate of the ridges, the BCB film was cured at temperatures lower than the standard soft cure (210 °C). The removal of the 200 °C-cured BCB ridges, as shown in Figure 3.29(c), was much faster, with an average removal rate of 0.9 μm/min. We were able to

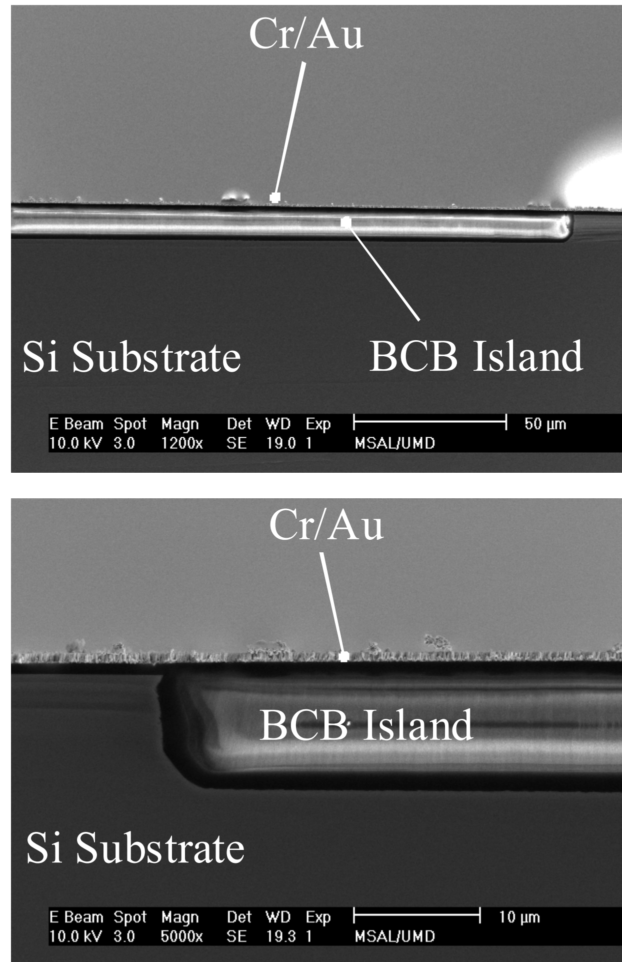

Figure 3.30. Scanning electron micrographs (SEMs) showing the cross section of a 5 mm × 10 mm, 12-µm deep EBiS island after deposition of two BCB layers and planarization. Thin layers of chromium (Cr) and gold (Au) were sputtered on the wafer to help with taking the SEM and to test the adhesion of metal layers.

increase the removal rate of the cured BCB ridges up to 2.4 µm/min with no peel-off by lowering the cure temperature to 184 °C.

Finally, as shown in Figure 3.27(d), the BCB islands are planarized using CMP, providing a planar surface for the subsequent process steps. Depending on the subsequent processes, a soft cure (at 210 °C for 40 minutes) or a hard cure (at 250 °C for 60 minutes) of BCB polymer is performed at the end of the process. Figure 3.30

shows scanning electron micrographs (SEMs) of the cross-section of a completed EbiS island. The island is 12 μm deep with an area of 5 mm × 10 mm.

3.4.2. Process Development and Characterization

In order to study how the planarity of the EBiS islands evolves during the fabrication, we measured the island depth and the BCB ridge height before and after each BCB film deposition and before and after each CMP run. The measurement was performed on four wafers (A, B, C, and D) with islands of two different sizes, 5 mm × 14 mm and 5 mm × 20 mm. The islands were etched using DRIE to an average depth of 26.8 μm. Figure 3.31 shows how the average island depression depth in each wafer changes after each step. Two layers of BCB polymer were deposited and three CMP runs were performed. The average island depression depth was reduced to below 2 μm. It is clear from the trend of reduction in the depression depth that with another BCB layer deposition and CMP run, the average island depression can be reduced to close to zero. Although the mechanical abrasion is negligible in a depression, an increase in the depression depth is observed after each CMP step. This shows that ILD1300 slurry can chemically remove BCB polymer from the island area. Figure 3.32 shows the changes of the average BCB ridge height in each wafer after each step. The average height was reduced to less than 1 μm and could be reduced even more with a longer CMP at the end. In order to quantify the planarization of the EBiS process, we calculated the total step height reduction (T-SHR) in each step for each wafer. T-SHR is given by:

$$T - SHR = \left(1 - \frac{h_{ridge} + d_{dep}}{d_{island}}\right) \times 100 \tag{3.16}$$

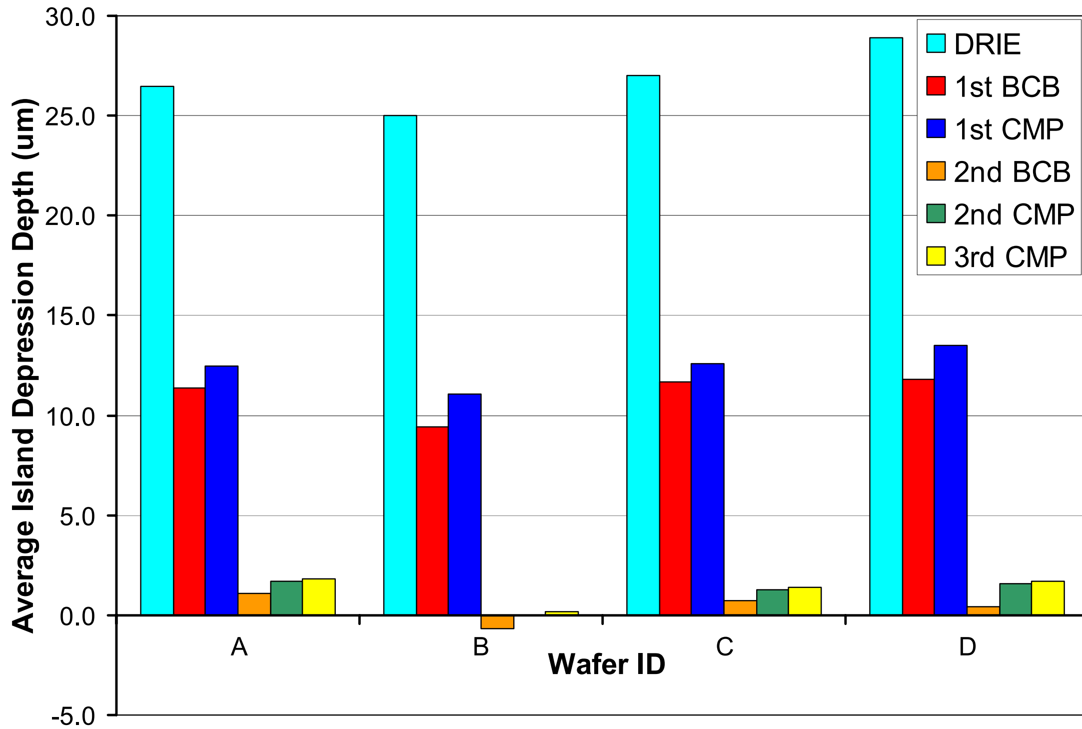

Figure 3.31. Average island depression in different steps of EBiS process for four test wafers.

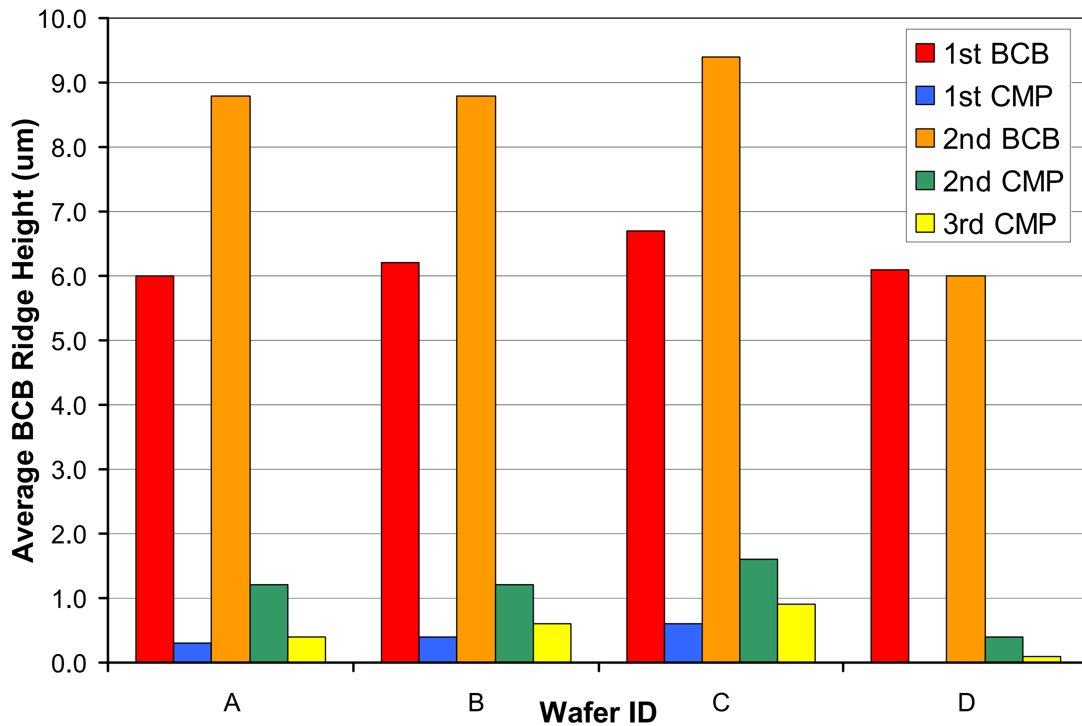

Figure 3.32. Average BCB ridge heights in different steps of EBiS process for four test wafers.

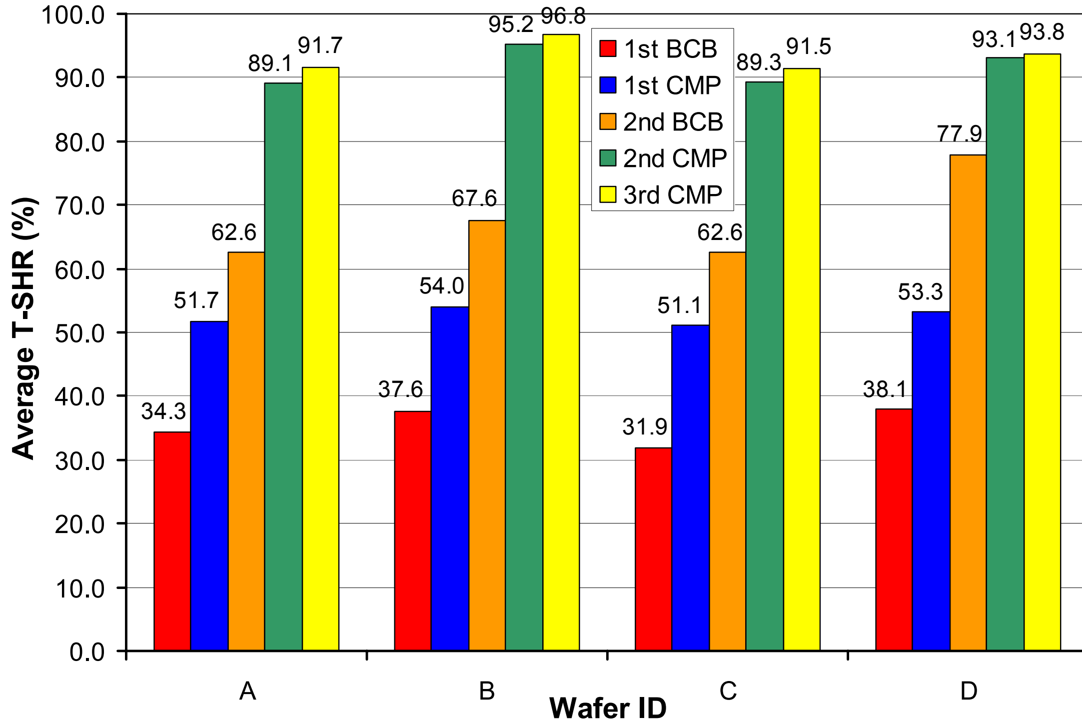

Figure 3.33. Average total step height reduction (SHR) in different steps of EBiS process for four test wafers.

where h_{ridge} is the average BCB ridge height, d_{dep} is the average island depression depth, and d_{island} is the average initial island depth. The ideal T-SHR is 100 %, which represents perfectly planarized EBiS islands. As shown in Figure 3.33, a T-SHR of above 91 % was achieved for all wafers. The T-SHR of wafer B is even above 96 %. Considering the increase in T-SHR from second to third CMP, a T-SHR of close to 100 % could be accomplished with longer CMP at the end.

3.5. Fabrication of Microball Bearings

As discussed in Chapter 2 and shown in Figure 2.14, there are three basic designs for microball bearings. From the design point of view, the v-groove design, shown in Figure 2.14(a), provides the most stable support for the slider, while the isotropically-etched trench design, shown in Figure 2.14(c), provides the least stable

support. However, depending on the type of the bearings (linear or rotary), the fabrication of each design involves specific challenges, which affects the choice of the design.

3.5.1. Fabrication of Linear Microball Bearings

Fabrication of linear microball bearings based on the v-groove design, shown in Figure 2.14(a), can be achieved using silicon anisotropic wet etching in solutions such as potassium hydroxide (KOH), tetramethyl ammonium hydroxide (TMAH), ethylenediamine pyrocatechol (EDP), hydrazine, and ammonium gallate [135]. KOH and TMAH are safer than the others and KOH generally produces less surface roughness. If (100) silicon wafer is used, this method results in v-grooves with fixed sidewall angle, equal to the angle between (100) and (111) crystallographic planes in silicon (54.735°). Figure 3.34 shows a v-groove etched in hot KOH solution using low-stress silicon nitride etch mask. The challenge in fabrication of linear microball bearings with anisotropic wet etching is precision of fabrication, accuracy of alignment to crystallographic planes, selectivity of etch between (100) and (111) planes, and smoothness of sidewalls. These challenges can be overcome by careful photomask design and characterization of etching process. However, integration of KOH-etched silicon v-grooves and BCB polymer films thicker that 1 μm has proven to be extremely challenging [132].

One way to decrease the friction of the microball bearings is to reduce the angle between the sidewall and the bottom surface of the v-groove that is fixed in a KOH-etched silicon v-groove. Fabrication of v-grooves with arbitrary sidewall angles can be achieved by gray-scale technology [136, 137]. Different angles can be

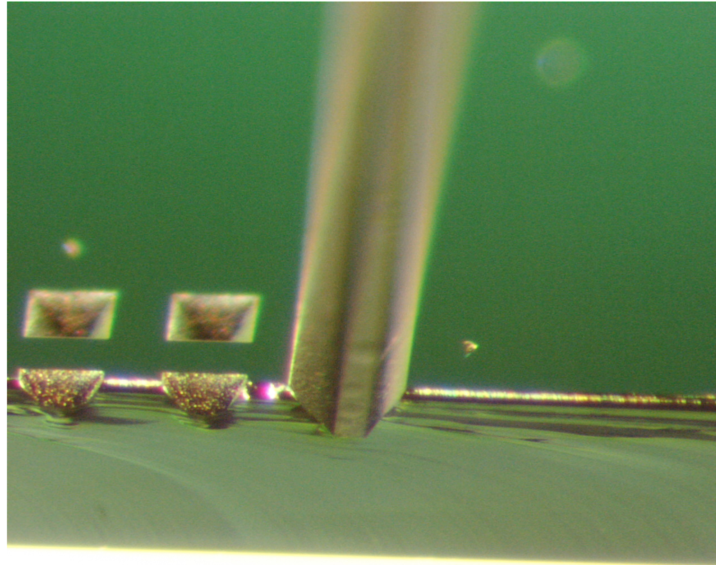

Figure 3.34. Optical micrograph of a silicon v-groove etched in 45 wt% KOH solution at 82 °C for 3 hours. The etch rate of (100) plane was 0.8 μm/min and the etch rate of (111) plane was 1.0 μm/hr. The v-groove has a width of 287μm and a depth of 146 μm.

achieved by tuning the etch selectivity [138]. The main challenge in using gray-scale technology for microball bearings is the sidewall surface roughness. The roughness can be reduced by either a short isotropic wet etching (e.g. in HNA, a mixture of hydrofluoric acid, nitric acid, and acetic acid) or a short low-power, high pressure SF6 plasma etching. Growing a layer of wet silicon dioxide and stripping the oxide in hydrofluoric acid can reduce roughness even further.

The anisotropically-etched trench design, shown in Figure 2.14(b), can be fabricated using deep reactive ion etching (DRIE). Considering the structure of the slider in the B-LVCM, this method has the advantage of fabricating the microball bearing housing and the electrically-active area (slider poles) with one photomask and in one run of DRIE. Figure 3.35 shows an anisotropically-etched trench. The precision of fabrication to achieve the desired air gap, smoothness of the bottom of the trench, and the uniformity of etch across a large area are challenging issues in

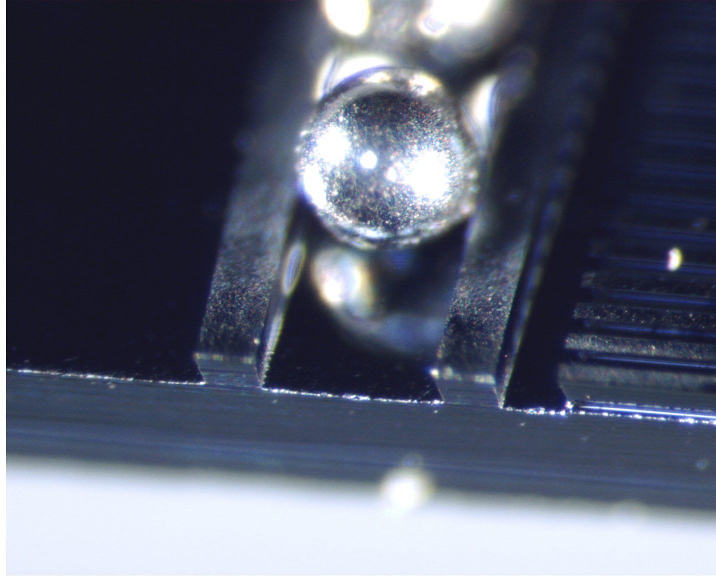

Figure 3.35. Optical micrograph of a DRIE-fabricated trench and a microball. The width of the trench is 290 μm and its depth is 130 μm.

development of this structure and can be addressed by characterization of the etch process.

The isotropically-etched trench design, shown in Figure 2.14(c), can be fabricated using silicon isotropic wet etching with HNA or using silicon isotropic dry etching with xenon difluoride (XeF_2). This process, however, is not well controlled and it is difficult to achieve the desired depth accurately.

In fabrication of the B-LVCM, the anisotropically-etched trench was used as a trade-off between stability of the slider and ease of integration with BCB polymer films.

3.5.2. Fabrication of Rotary Microball Bearings

Except the v-groove design, the fabrication of the rotary microball bearings is similar to that of the linear microball bearings. Unlike the linear v-grooves, the fabrication of rotary v-grooves is not possible with anisotropic wet etching. It is,

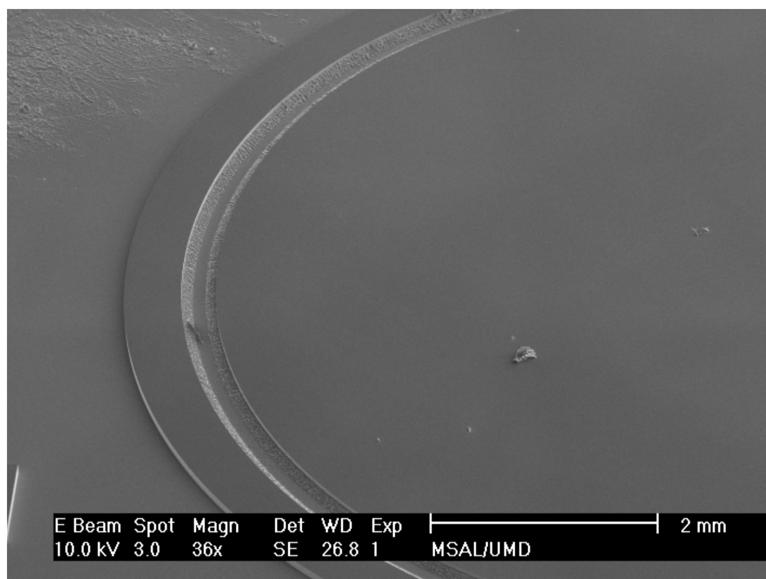

Figure 3.36. Scanning electron micrograph (SEM) of a gray-scale-fabricated rotary v-groove with a sidewall angle of about 35°.

however, possible using the gray-scale technology, where arbitrary-angle v-grooves can be fabricated by controlling the selectivity of silicon etching. The sidewall roughness is the main drawback of this method. Figure 3.36 shows an SEM of a gray-scale-fabricated rotary v-groove with a sidewall angle of about 35°.

3.6. Stator Fabrication

Fabrication of the stator consists of 43 process steps, including seven photolithography steps (see Tables 3.7 and 3.8) and can be summarized in three stages: (1) development of EBiS islands, (2) fabrication of a two-level metal interconnection/electrode structure, and (3) fabrication of the microball housings. All BCB depositions were performed using spin-on photosensitive BCB according to an in-house-developed photosensitive BCB process (modified from the manufacturer's recommended process). Figure 3.37 shows some of the major steps in fabrication of the stator after the development of the EBiS islands is complete.

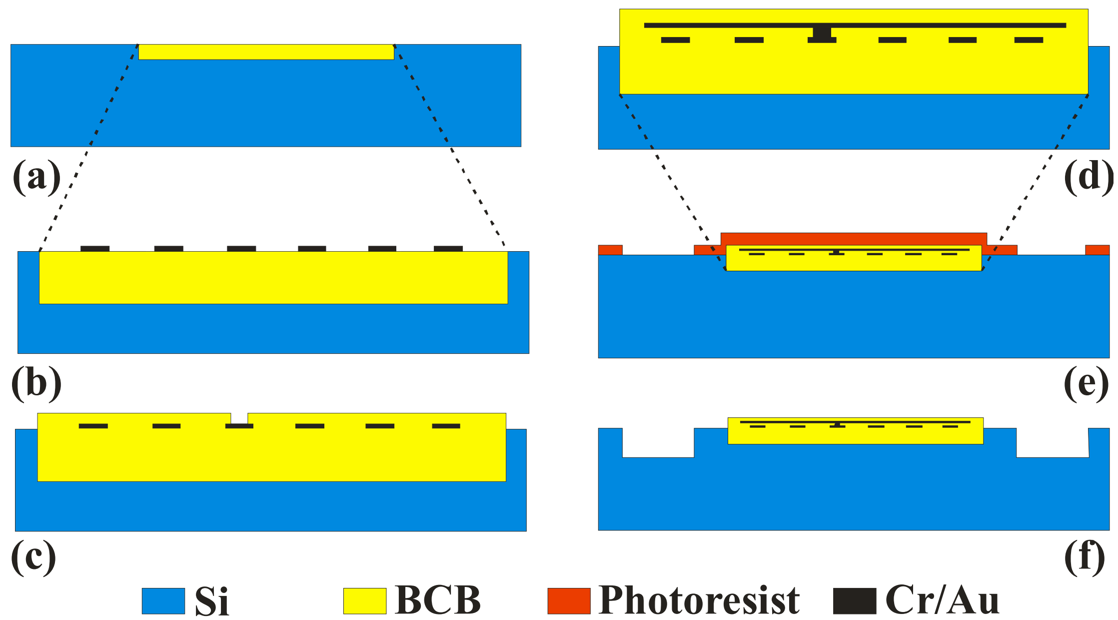

Figure 3.37. Major steps in fabrication of the stator after the completion of the EBiS process: (a) silicon wafer with EBiS islands (first BCB layer), (b) the interconnects and pads (first metal layer), (c) ILD and vias (second BCB layer), (d) the electrodes (second metal layer) and passivation (third BCB layer), (e) photoresist pattern of microball housings (trenches), (f) etched trenches.

Starting with a bare 4” silicon wafer, 25-µm deep EBiS islands are fabricated using photolithography, deep reactive ion etching (DRIE), and chemical mechanical planarization (CMP), similar to the process shown in Figure 3.27. This is the starting point in Figure 3.37(a).

Next, as shown in Figure 3.37(b), the first metal layer is fabricated on top of the EBiS islands using image reversal photolithography, sputtering, and lift-off. The first metal layer forms six interconnects and pads and consists of 20 nm of chromium (Cr) and 200 nm of gold (Au). Figure 3.38 shows pictures of the stator after the lift-off.

A BCB ILD layer is then fabricated to isolate the first and second metal layers. As shown in Figure 3.37(c), the ILD layer incorporates vias that are used to

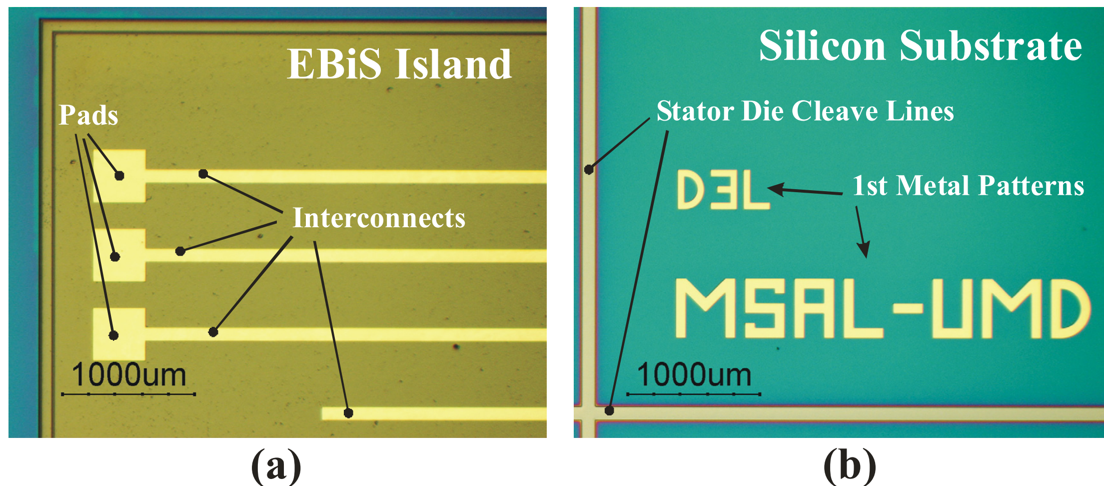

Figure 3.38. Optical micrographs of the stator after lift-off of the first metal layer: (a) interconnects and pads on top of the EBiS island and (b) metal pattern on the silicon substrate.

connect the two metal layers wherever required. The thickness of the ILD layer plays an important role in creating a void free film. Figure 3.39(a) shows part of the stator after spin-casting and developing 2 μm to 3 μm of the BCB ILD (before the cure step). Since the BCB film is too thin, several voids were created around the edge of the first metal layer. By increasing the thickness of the BCB film to 4 μm to 5 μm (before the cure step), we were able to eliminate the voids, as seen in Figure 3.39(b). It should be noted that if the BCB ILD layer is too thick, there will be problems filling the vias when depositing the second metal layer, leading to high resistive connection between the interconnects and the electrodes.

Next, as shown in Figure 37(d), the second metal layer is fabricated with the same process steps used for the first metal layer. The second metal layer forms the stator electrodes and has the same thickness of Cr and Au as the first metal layer. Another BCB layer (passivation) is fabricated that covers the electrodes. At this point, the fabrication of the stator active area is complete. Figure 3.40 shows pictures

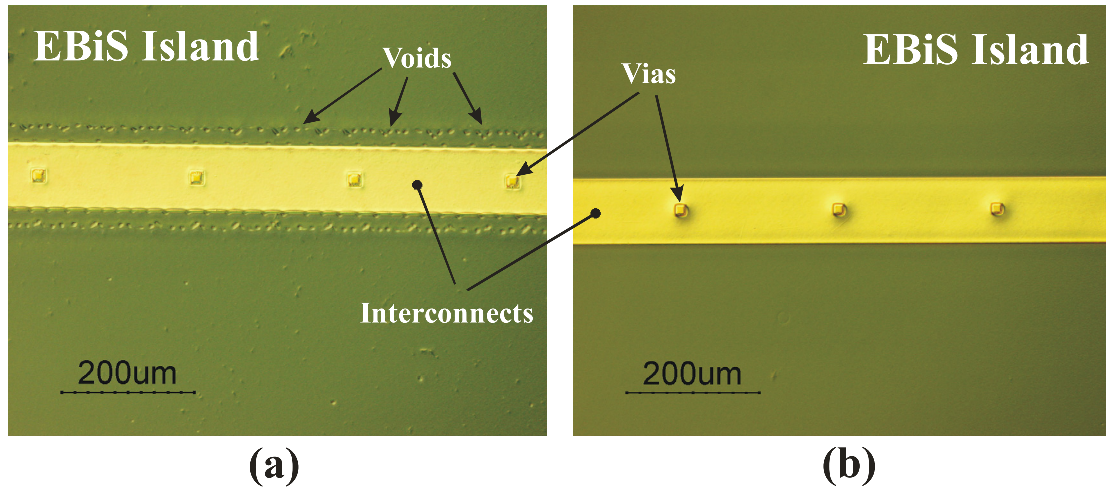

Figure 3.39. Optical micrographs of the stator after spin-casting and developing the BCB ILD layer before the cure step: (a) with a thickness of 2 μm to 3 μm, voids form in the BCB film at the edge of metal structure and (b) with a thickness of 4 μm to 5 μm, voids disappear.

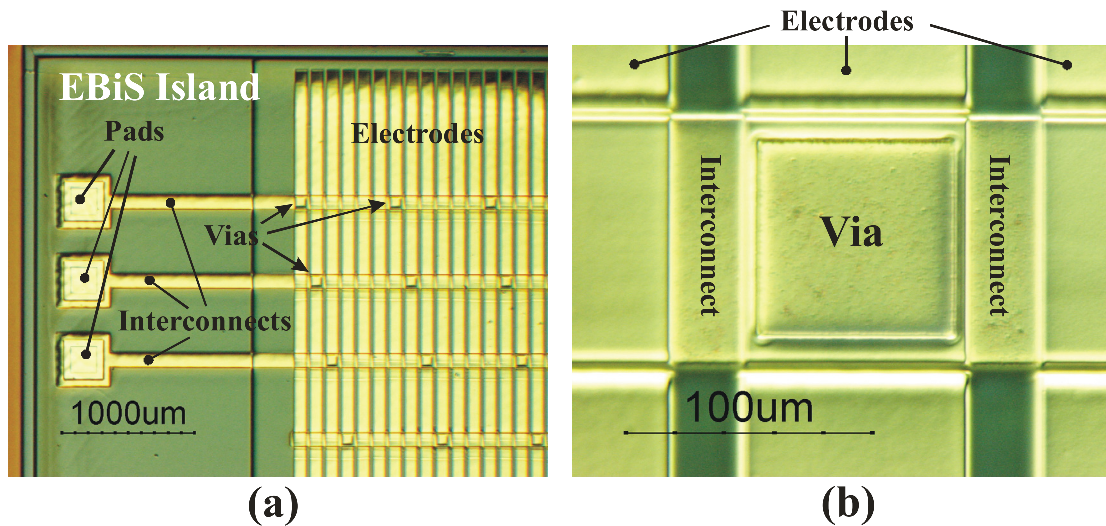

Figure 3.40. Optical micrographs of the stator active area, which consists of three BCB layers and two metal layers: (a) interconnects connect every other six electrodes with each other through vias and (b) an 80 μm × 80 μm via.

of a completed active area and Figure 3.41 shows a cross section of the active area across the electrodes.

Finally, the microball housings are patterned and etched in the stator using DRIE, as shown in Figures 3.37(e) and 3.37(f). Figure 3.42 shows a schematic 3D view of a complete stator. On our fabricated samples, the average etch depth of the

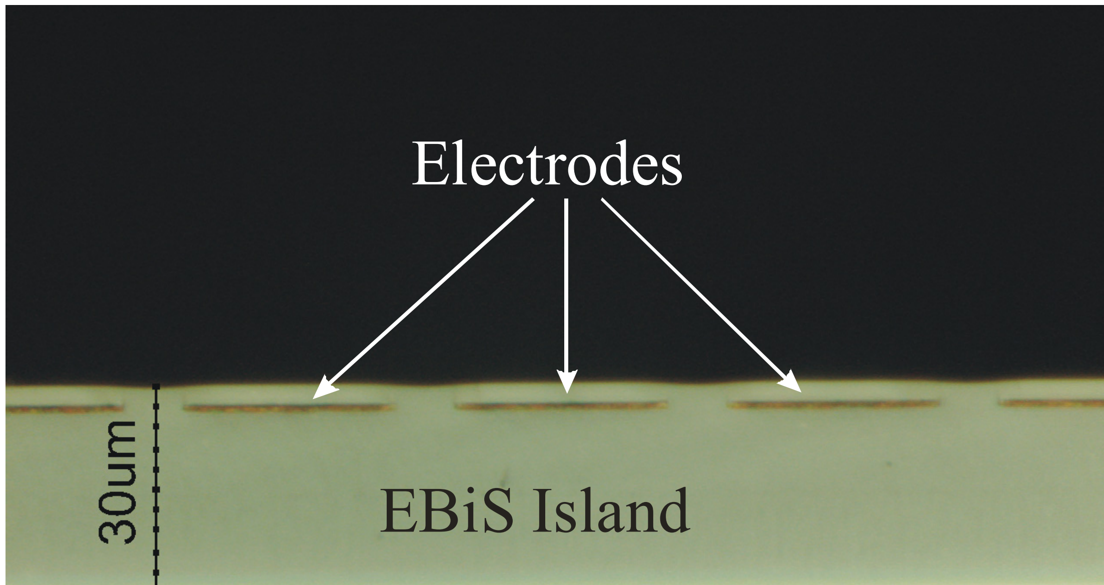

Figure 3.41. An optical micrograph of the cross section of the stator active area across the electrodes.

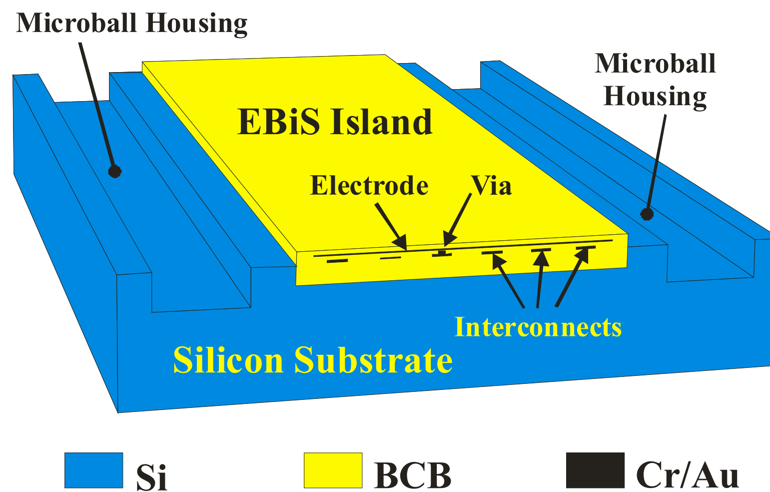

Figure 3.42. A schematic 3D view of a completed stator.

trenches across the stator wafer was measured to be 125.2 μm with a standard deviation of 0.2 %, which indicates a good uniformity of the microball housing depth on the stator wafer. Figure 3.43 shows complete fabricated stator of three devices $D1_{SHORT}$, $D2_{SHORT}$, and $D3_{SHORT}$ with one microball placed in each trench. The fabrication yield of the stator of $D2_{SHORT}$ and $D2_{LONG}$ was better than other devices; therefore, all tests were performed on these devices.

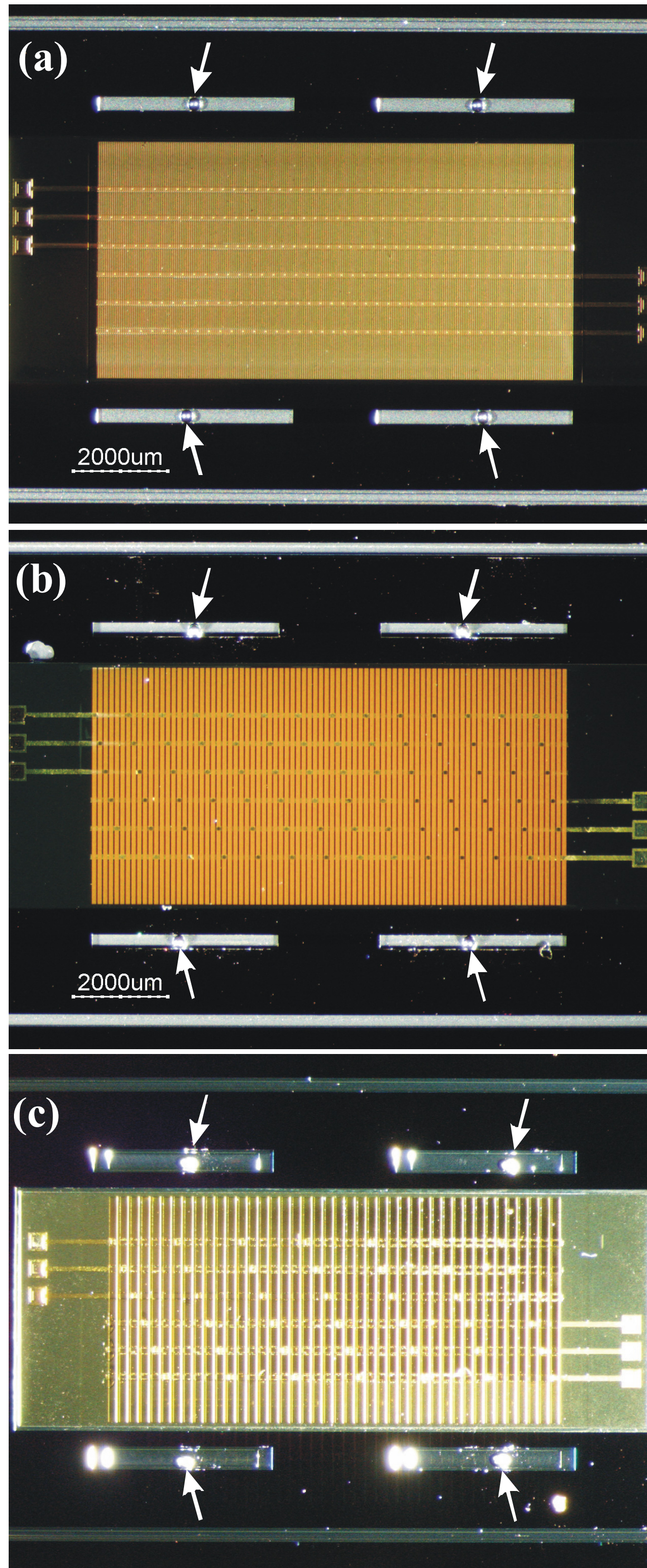

Figure 3.43. Optical micrographs of the completed stators. The microballs are marked by arrows. (a) D_{1SHORT}, (b) D_{2SHORT}, and (c) D_{3SHORT}.

3.7. Slider Fabrication

Fabrication of the slider consists of five process steps, including one photolithography step. The microball housings and the slider poles are etched to the same approximate depth together in one DRIE step. The height of the slider poles is trivial as long as it is much larger than the air gap and the electrode/pole width. However, the accuracy of the depth of the housings is important because it directly affects the air gap. Another consideration in fabrication of the slider is that in order to minimize the effect of the bulk of the slider on the electric field in the gap, most of the slider surface facing the stator active area except the poles are etched. This can lead to an increased loading during the DRIE steps and a non-uniform etched depth across the wafer. One way to get around this problem is to minimize the number of slider die and place them far from each other in the wafer.

Figure 3.44 shows a complete fabricated slider with one microball placed in each trench. Note that what is shown in figure 4 is the bottom of the slider that faces the stator active area in an assembled B-LVCM. The average etch depth of the trenches across the slider wafer was measured to be 142.6 μm with a standard deviation of 3.3%, which is significantly higher compared to that of the stator trenches. This is believed to be caused by the high loading of the slider wafer during DRIE since a large portion of silicon was exposed to the plasma. For the experiments on device $D2_{SHORT}$, we diced the wafer into pieces and picked a slider die with an average etch depth of 144.6 μm and standard deviation of 1.3% across the die. This defines an air gap with an average of 15.2 μm and a standard deviation of 12.6%,

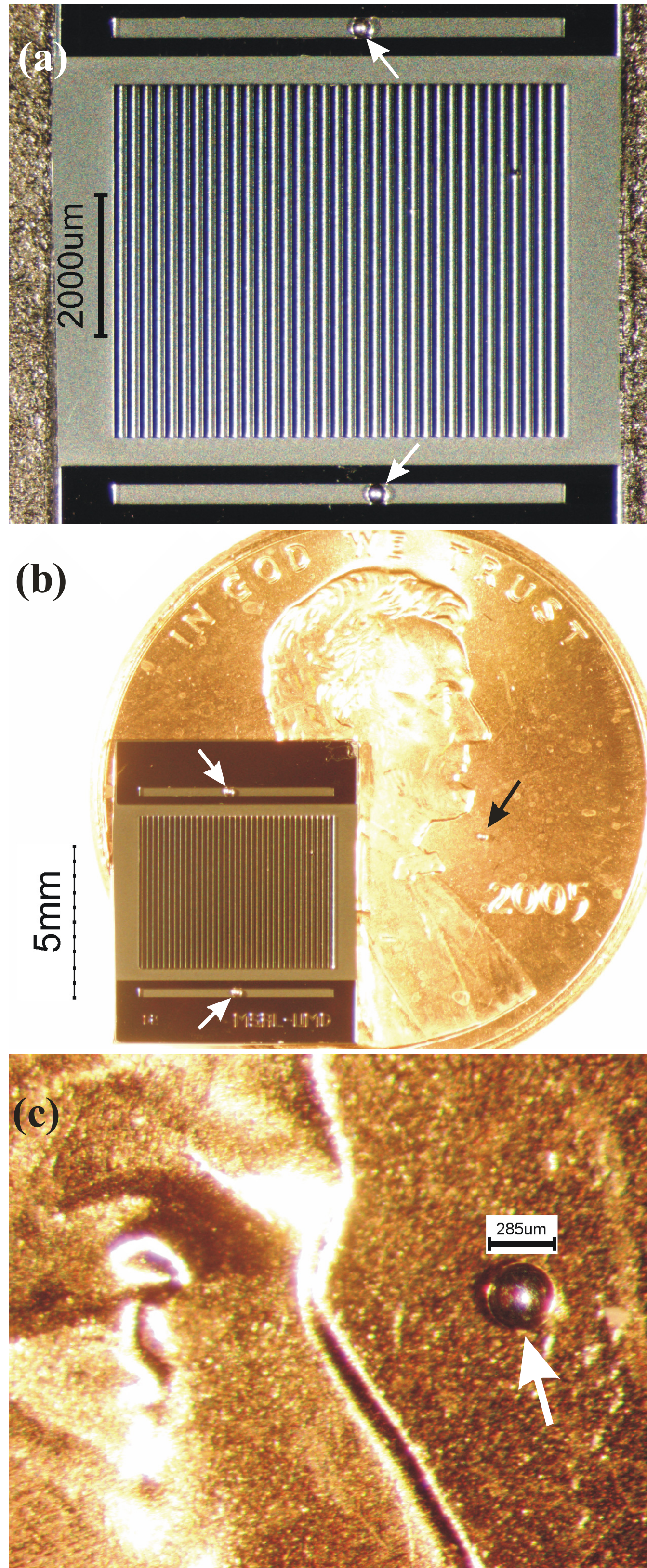

Figure 3.44. Optical micrographs of a completed slider of device D_{2SHORT}. The microballs are marked by arrows: (a) Active area and trenches of in the slider die, (b) size of the slider die compared to a penny, and (c) a microball.

which corresponds to a variation of 1.9 μm across the device. Similarly, for experiments on device $D2_{LONG}$ an average air gap of 19.2 μm was used.

Chapter 4: Device Test and Characterization

The objective of this chapter is to provide the details on how we tested the operation of the fabricated B-LVCM. In addition, we will describe the experimental methods and tools utilized for measurement of the electromechanical characteristics of the B-LVCM. The primary output parameters that can be used to characterize the behavior of the B-LVCM in steady-state operation are the instantaneous aligning force and the slider speed. These characteristics are indirectly measured using the directly measured data of the variable capacitance and the slider position during operation, respectively. The direct measurement of the speed and force requires the incorporation of special sensors in the device. This makes the design and fabrication of the device complicated and is left as a topic for future research activities. It should be noted that it is easier to measure the capacitance when the device is not in operation; therefore, it is a static measurement while the measurement of the slider position is a dynamic measurement because it is performed when the device is in operation.

As discussed in Chapter 2, the aligning force is proportional to the spatial gradient of the capacitance; therefore, by measuring the capacitance of the B-LVCM versus the slider position, the aligning force can be extracted as a function of the slider position. Similarly, since the speed is the time derivative of the position, by measuring the position of the slider, we can obtain the speed of the slider as a

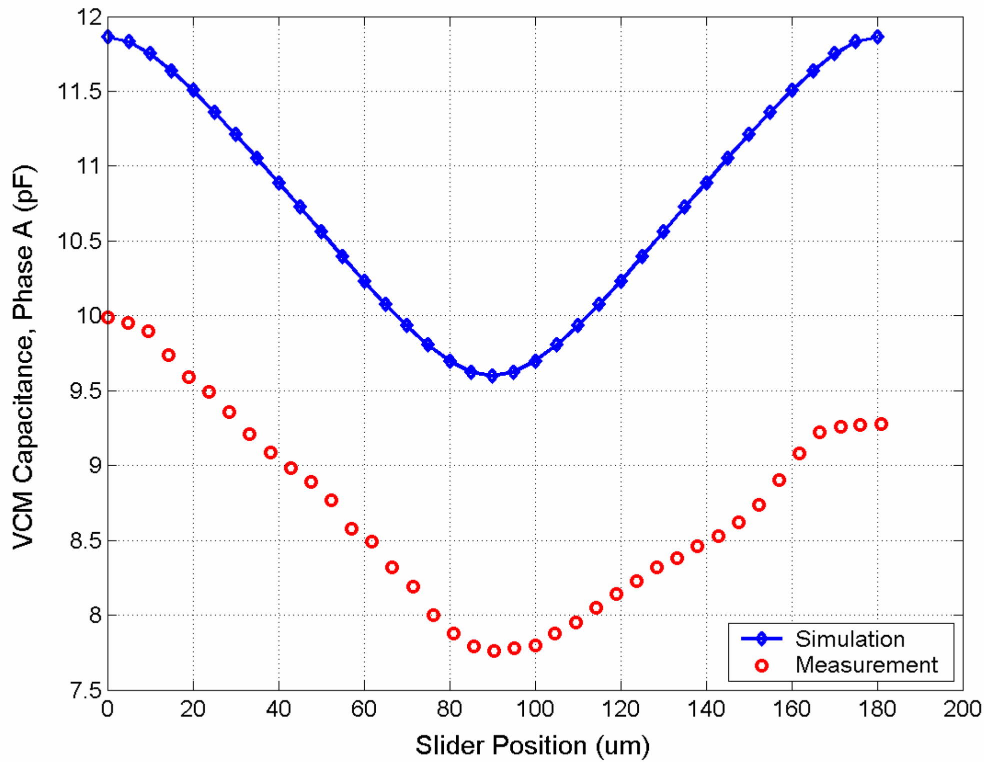

Figure 4.1. Simulated and measured B-LVCM capacitance (one phase) for device $D2_{SHORT}$. The simulated profile is curve-fitted to a sine-squared function very well.

function of time (or slider position). A comparison with the numerical simulation and model predictions is also included in this chapter.

4.1. Static Measurements: Capacitance and Force

Figure 4.1 shows the simulated and measured capacitance profile of the B-LVCM phase A as a function of the slider position for device $D2_{SHORT}$. Since the profile is periodic with the position, only one period is shown. The reference point (zero) of the slider position is arbitrary and in this case is chosen to be the maximum capacitance position, where phase A electrodes are fully aligned to the corresponding slider poles. The simulated profile was numerically calculated using FEMLAB™ software with the slider shifted in 5-µm steps. The measured profile was obtained by

manually moving the slider in 5-μm steps using a probe needle of a micropositioner and measuring the capacitance between the slider and phase A using a capacitance meter. The position of the slider was measured using a microscope. There is a good agreement between the general trends of the two profiles; however, the 20 % difference between the absolute values of the measured and simulated capacitances can be explained in terms of tolerances in fabrication of the trenches, electrodes, poles, the non-uniformity of etch across the device, and fabrication defects. In addition, during the simulation all non-active phases were connected to ground, while during the measurement, all non-active phases were floated, therefore, there is a difference in the parasitic capacitance. Despite the difference in the absolute value of the capacitance, in extraction of the force from capacitance only the slope of the graph is important and the absolute values do not contribute to the outcome.

Using Equation (2.56) and assuming a 100-V DC excitation voltage, the aligning force as a function of the slider position was extracted from the simulated and measured capacitance data after a sine-squared curve fit. The air gap is assumed to be 15.2 μm, which is the average air gap of the device under test. The result is shown in Figure 4.2. There is good agreement between the aligning force profiles extracted from simulated and measured data. The maximum aligning force for both profiles is 0.17 mN, close to the estimated value of 0.20 mN from Table 2.4.

Figure 4.3 shows similar profiles for all six phases of device $D2_{LONG}$ with an average air gap of 19.2 μm. The total aligning force profiles calculated from the capacitance profiles (after a sine-squared curve fit and assuming a 6-phase configuration with 100-V P-P square-wave excitation voltage) are shown in Figure

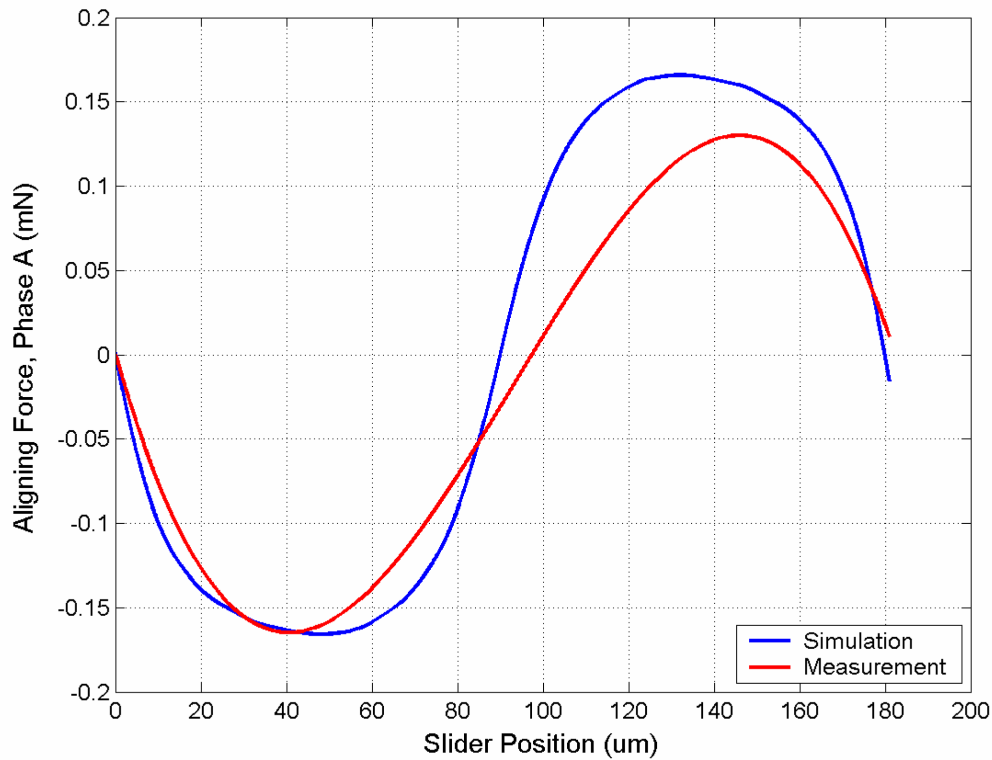

Figure 4.2. Simulated and extracted (from capacitance data) B-LVCM aligning force for device $D2_{SHORT}$ when excited with a 100-V DC voltage. The force was calculated from sine-squared curve fits to the simulated and measured capacitance data of Figure 4.1.

4.4. There is a good agreement between the simulation and measurement average force (0.24 mN vs. 0.27 mN). The maximum simulated aligning force is 0.25 mN, while the maximum measured aligning force is 0.41 mN. The discrepancy between these data and Table 2.4 is due to the difference between designed and fabricated air gap. Furthermore, the effect of fringing electric field was neglected in calculating the data in Table 2.4.

Although the above method is an indirect measurement of the aligning force, equation (2.56) can predict the aligning force of a 6-phase micromotor fairly accurately and the only major limitation is the relative error in the measurement of the capacitance. Direct measurement of the applied force to a moving slider in an

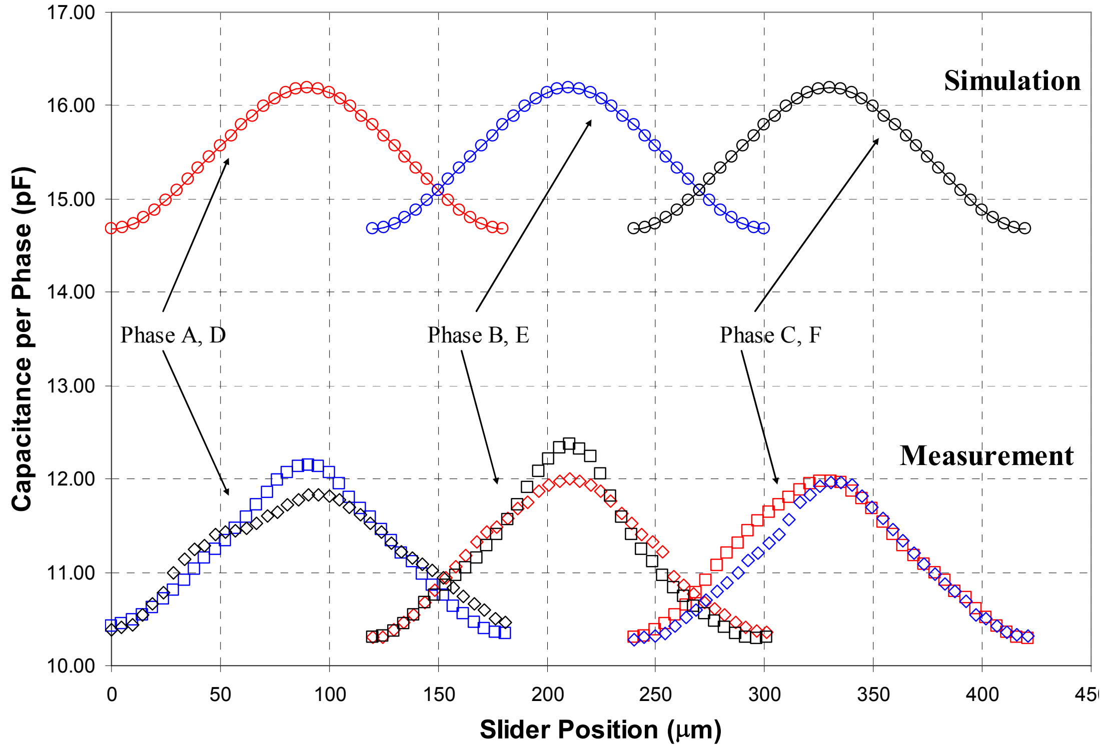

Figure 4.3. Simulated and measured capacitance of all B-LVCM six phases for device $D2_{LONG}$.

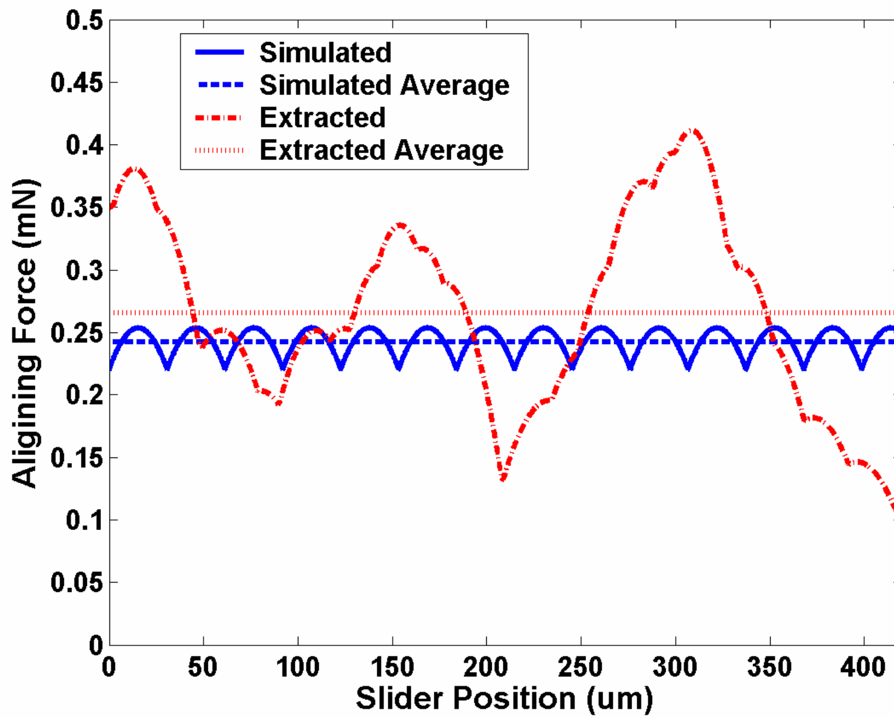

Figure 4.4. Simulated and extracted total aligning force and their average values for device $D2_{LONG}$ when excited with a 100-V P-P voltage. The force is calculated from curve fits to the simulated and measured capacitance data of Figure 4.3.

operational micromotor without disturbing the motion of the slider is practically impossible. One approach to directly measure the force is to redesign the motor to incorporate tethers and force sensors in the slider, which ultimately leads to a more complicated fabrication process.

4.2. Dynamic Measurements: Position and Speed

The block diagram of the experimental setup used for dynamic measurements is shown in Figure 4.5. The setup was designed and built to drive the B-LVCM with AC excitation voltages in multiphase configuration and characterize the motion of the slider. This system generates six high voltage (up to 300 V P-P) square waves controlled by a LabVIEW program (designed as part of an undergraduate Summer research project by Alex Frey). The amplitude, frequency, duty cycle, and phase of the output waveforms can be entered using the LabVIEW control panel by the user. In addition, the program can switch two pairs of the waveforms with a user defined switching frequency. Switching the waveforms is used to change the direction of the slider motion, creating an oscillating motion. This will compensate for the limited range of the slider motion (a few millimeter) and allow us to collect the position data for an extended period of time. The motion of the slider is captured by a commercial camcorder (Sony DCR-TRV22) at 30 frames per second. IMAQ Vision Builder software controls the camera and retrieves the captured frames. IMAQ is also used to post-process the captured images of the slider and track a mark placed on the slider to extract the position of the slider as a function of time. This is similar to the method we previously used to characterize the dynamic friction of microball bearings [103]. Figure 4.6 shows pictures of the actual test setup.

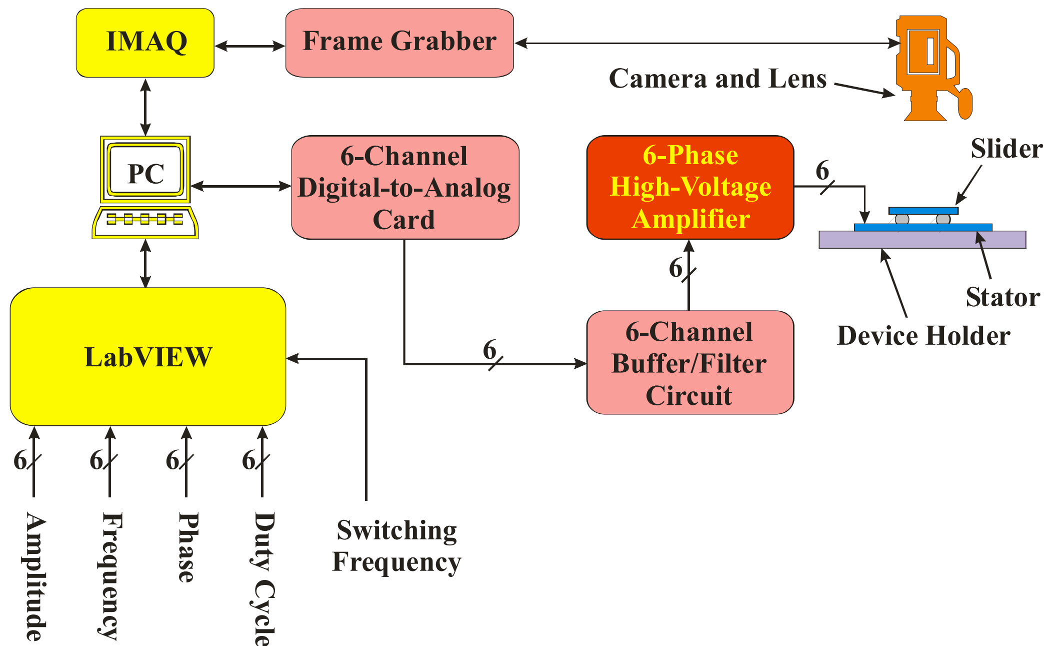

Figure 4.5. Block diagram of the experimental setup for driving the B-LVCM and characterization of the slider motion.

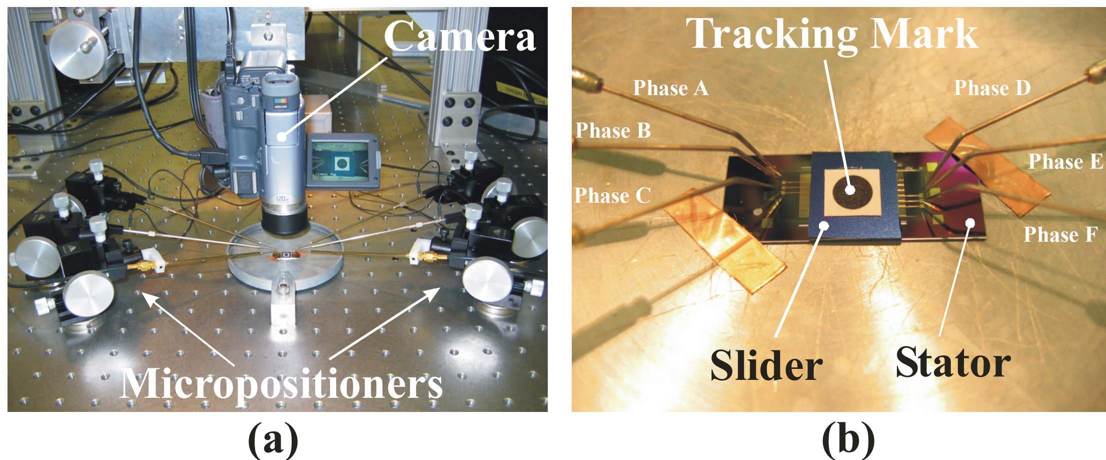

Figure 4.6. The experimental test setup for driving the B-LVCM and characterization of the slider motion: (a) The camera looking at a B-LVCM under test and (b) the device under test is held down on the device holder with copper tapes. The probe needles apply the six phases of the voltage.

The initial AC tests of the B-LVCM were performed on device $D2_{SHORT}$ with a 3-phase configuration, where only three phases A, B, and C were excited with square-wave voltages, and phases D, E, and F were float. The phase difference

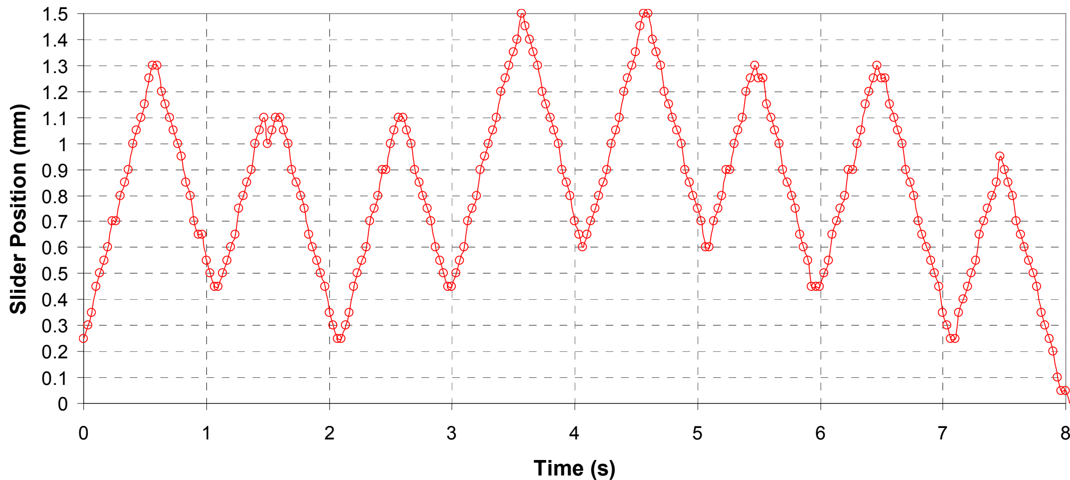

Figure 4.7. Measured slider position vs. time for device $D2_{SHORT}$ when excited with a 3-phase, 10 Hz, 100-V P-P, square-wave voltage (direction was changed at 2 Hz).

between A, B, and C was 120°, similar to the 6-phase configuration. Figure 4.7 shows the position of the slider as a function of time when device $D2_{SHORT}$ was driven at 10 Hz and 100 V P-P. The direction of the motion was switched at 2 Hz to obtain a periodic motion. A drift in the center position is observed that is believed to be due to the random surface defects in the microball housings caused by dust, humidity, and wear debris. The growth of the native oxide on the silicon surface is a major contribution to wear debris and it is exacerbated with humidity. These defects lead to a non-uniform rolling friction of the microball bearings and result in an erratic motion in the absence of a closed-loop control system. The average speed calculated over the slopes of the graph in Figure 4.7 is 1.82 mm/s, within 1.1 % of the theoretical value (1.80 mm/s from Table 2.4). Figure 4.8 shows the test with the same conditions in Figure 4.7 right after dipping the slider in BOE to remove the native oxide and cleaning the stator and the slider with general solvents. An appreciable improvement in the stability of the slider motion is observed. The average speed in this case is 1.92 mm/s.

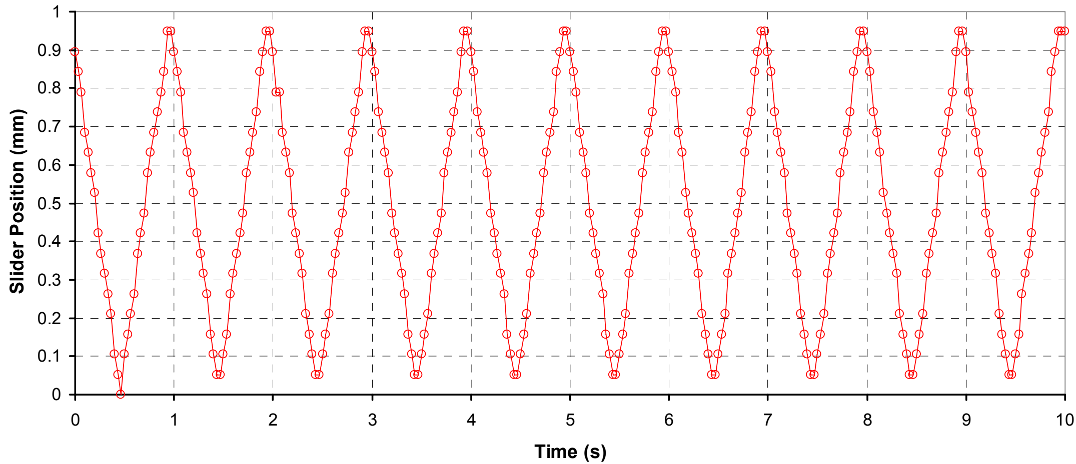

Figure 4.8. Measured slider position vs. time for device $D2_{SHORT}$ when excited with a 3-phase, 10 Hz, 100-V P-P, square-wave voltage (direction was changed at 2 Hz) after cleaning the stator and the slider. A more stable motion is observed.

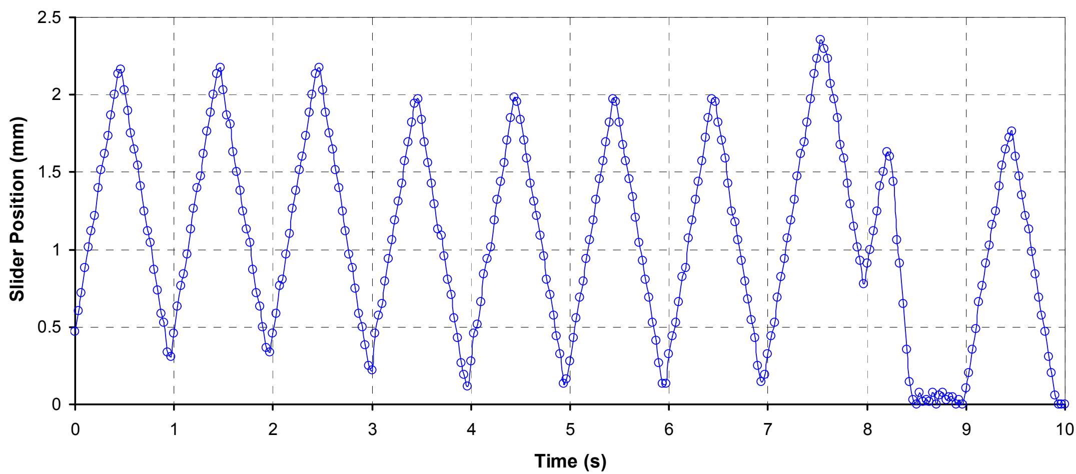

Figure 4.9. Measured slider position vs. time for device $D2_{SHORT}$ when excited with a 3-phase, 20 Hz, 100-V P-P, square-wave voltage (direction was changed at 2 Hz).

The AC tests were also performed with excitation frequencies higher than 10 Hz. In Figures 4.9 and 4.10 the stator was excited at 20 Hz and 30 Hz with an average speed of 3.68 mm/s (compare to 3.60 mm/s from Table 2.4) and 5.35 mm/s (compare to 5.4 mm/s from Table 2.4), respectively. The rest of the test conditions were the same as in Figure 4.7. A Similar experiment at 20 Hz with a switching frequency of 4 Hz resulted in an average speed of 3.56 mm/s.

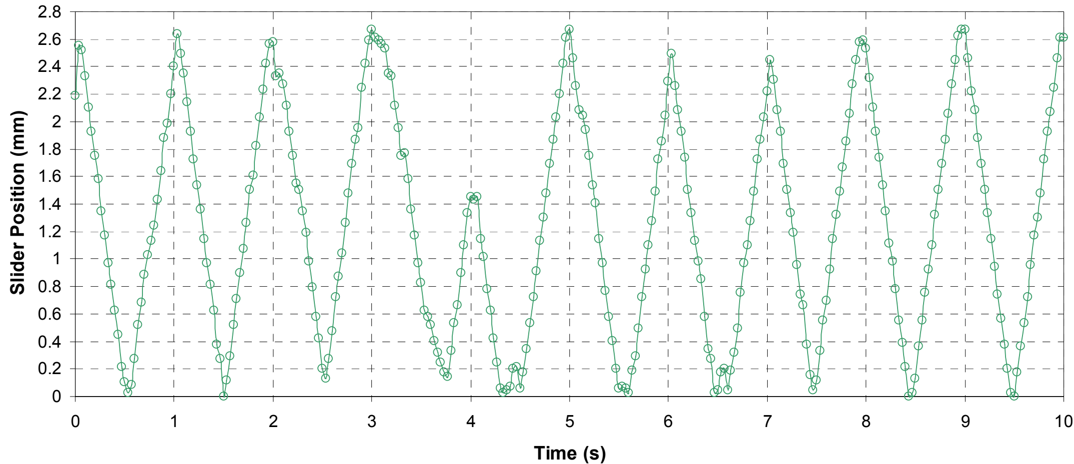

Figure 4.10. Measured slider position vs. time for device $D2_{SHORT}$ when excited with a 3-phase, 30 Hz, 100-V P-P, square-wave voltage (direction was changed at 2 Hz).

As seen in Figures 4.7 to 4.10, the motion of the slider in each ramp is not smooth and exhibits some irregularities, i.e. the data points are not equally distant on the position axis. This means that the instantaneous slider speed undergoes sudden changes at times. It is expected that a smoother slider motion is achievable if a 6-phase configuration is used. In order to verify this, the AC test with a 6-phase configuration was performed on device $D2_{SHORT}$. Figure 4.11 shows the position of the slider as a function of time for the device driven at 20 Hz and 120 V P-P with a switching frequency of 1.5 Hz. The average speed is 3.98 mm/s. Figure 4.11 shows a smoother slider motion in each ramp compared to Figures 4.7 to 4.10. A similar experiment with the 6-phase configuration at 10 Hz resulted in an average speed of 1.94 mm/s.

Table 4.1 shows the estimated (from Table 2.4) and measured average speeds at different excitation frequencies for 3-phase and 6-phase configurations. Note that the motor is not able to synchronize at higher frequencies, e.g. 80 Hz. This inability is

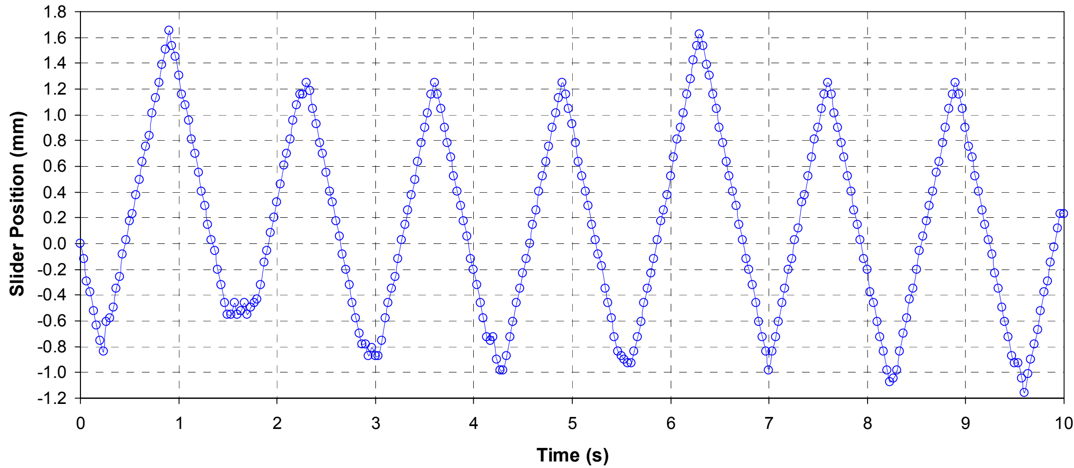

Figure 4.11. Measured slider position vs. time for device $D2_{SHORT}$ when excited with a 6-phase, 20 Hz, 120-V P-P, square-wave voltage (direction was changed at 1.5 Hz).

Table 4.1. Estimated and measured average speed for device $D2_{SHORT}$

Phase Configuration	Excitation Frequency	Estimated Average Speed	Measured Average Speed
3-Phase	10 Hz (Test 1)	1.80 mm/s	1.82 mm/s
3-Phase	10 Hz (Test 2)	1.80 mm/s	1.92 mm/s
3-Phase	20 Hz (Test 1)	3.60 mm/s	3.56 mm/s
3-Phase	20 Hz (Test 2)	3.60 mm/s	3.68 mm/s
3-Phase	30 Hz	5.40 mm/s	5.35 mm/s
6-Phase	10 Hz	1.80 mm/s	1.92 mm/s
6-Phase	20 Hz	3.60 mm/s	3.98 mm/s
6-Phase	40 Hz	7.20 mm/s	7.37 mm/s
6-Phase	80 Hz	14.40 mm/s	Not able to synchronize

a consequence of the open-loop control scheme used for operating the device. There is not an appreciable difference between 3-phase and 6-phase configuration as far as the average speed is concerned, although, as described before, a visual observation verifies that the 6-phase configuration provides a smoother motion as expected.

Chapter 5: Conclusion and Future Work

5.1. Summary of the Research Activities

In this dissertation, we presented the research activities on design, modeling, material characterization, process development, fabrication, and test of a bottom-drive, linear, variable-capacitance micromotor (B-LVCM). For the first time, microball bearings and benzocyclobutene (BCB) polymer insulating films were integrated in an electrostatic machine using microfabrication techniques. In the course of making the first prototype of this device, we developed technology templates that can be used to address the reliability and efficiency challenges of modern power microelectromechanical systems (MEMS).

In design and modeling, we developed an electromechanical model based on lumped-circuit elements to predict the dynamic behavior of the device. The BCB polymer is used as an electrical insulator in this device. Therefore, we have conducted a detailed study on the characterization of the electrical properties of BCB polymers and reliability implications of using these polymers in power MEMS. This included the measurement of the dielectric constant, I-V characteristics, and the effect of moisture absorption.

The B-LVCM was fabricated based on the embedded benzocyclobutene in silicon process (EBiS), a novel fabrication technique that reduces the mechanical stress and parasitic capacitances and enables the electrical isolation of active devices with minimal loss in efficiency. Several unit processes were developed, characterized,

and fine-tuned to fabricate the device. The chemical mechanical planarization (CMP) of BCB polymers is one of the key processes and was characterized to achieve more than 96 % planarization in the EBiS process.

The micromotor was successfully operated and characterized with 3-phase and 6-phase drive configurations at excitation frequencies up to 40 Hz and excitation voltages up to 120 V. A smoother slider motion was achieved using a 6-phase drive configuration. The capacitance, aligning force, and slider speed were numerically calculated and experimentally measured. A comparison of the theoretical and experimental results showed that the micromotor operates as predicted with a deviation mainly attributed to fabrication imperfections. The B-LVCM can operate as a long-range, high-speed micropositioner.

5.2. Contributions

Although most of the major contributions of this dissertation are to the field of power MEMS, there are aspects that can benefit other fields such as characterization and processing of low-k dielectric materials, microtribology, and test and measurement. The major contributions of this dissertation can be summarized as follows:

- Development of the first microball-bearing-supported micromotor
- Development of a high-range, high speed micropositioner with ~2 mm range of travel and over 7 mm/s travel speed
- BCB-based MEMS technology: Application of a low-k dielectric material (BCB polymer) in a microelectromechanical device for electrical insulation, interlevel dielectric (ILD), and passivation

- Development of embedded BCB in silicon (EBiS) process, a novel fabrication technique to integrate BCB polymers and microfabricated structures
- Characterization of CMP of BCB polymers and modification of the process to achieve high removal rate and low defect density

5.3. Future Work

This research provides several opportunities for improvement of previous work and initiation of new research activities in different areas. Some of these opportunities have to be left for future work because of the need for special equipment for specific experiments. In some other cases, a new approach or idea is needed to overcome the remaining challenges. These opportunities can be summarized as follows:

- New Devices, Systems, and Applications
    - Microball-bearing-supported bottom-drive rotary VCM with EBiS process as motor and generator
    - Micropump for fuel delivery
    - EBiS process for thermal isolation
- Design and Modeling
    - Estimation of machine efficiency and loss
- Material Characterization
    - Mechanical characterization of BCB polymers and effect of moisture absorption on stress and wafer bow
    - Characterization of microball bearings with silicon carbide coated trenches

- Test and Characterization
    - Characterization of the B-LVCM transient motion using high-speed camera
    - Characterization of microball bearing performance during machine operation
    - Systematic reliability tests (electrical and mechanical)
    - Direct measurement of force and mechanical power during machine operation
    - Measurement of the machine efficiency and effect of BCB polymer on energy loss

Bibliography

[1] A. H. Epstein, "Millimeter-scale, micro-electro-mechanical systems gas turbine engines," *Transactions of the ASME: Journal of Engineering for Gas Turbines and Power*, vol. 126, pp. 205-226, 2004.

[2] A. H. Epstein, S. D. Senturia, G. Anathasuresh, A. A. Ayon, K. Breuer, K.-S. Chen, F. E. Ehrich, G. Gauba, R. Ghodssi, C. Groshenry, S. A. Jacobson, J. H. Lang, C.-C. Lin, A. Mehra, J. O. Mur-Miranda, S. F. Nagle, D. J. Orr, E. Piekos, M. A. Schmidt, G. Shirley, S. M. Spearing, C. S. Tan, Y.-S. Tzeng, and I. A. Waitz, "Power MEMS and microengines," in *Proc. 9th International Conference on Solid-State Sensors and Actuators (Transducers'97)*, Chicago, IL, USA, pp. 753-756, 1997.

[3] F. Bohorquez and D. J. Pines, "Design and development of a biomimetic device for micro air vehicles," in *Proc. 9th Annual SPIE Smart Materials and Structures Symposium*, San Diego, CA, USA, pp. 503-517, 2002.

[4] T. N. Pornsin-Sirirak, S. W. Lee, H. Nassef, J. Grasmeyer, Y.-C. Tai, C.-M. Ho, and M. Keennon, "MEMS wing technology for a battery-powered ornithopter," in *Proc. IEEE 13th International Conference on Micro Electro Mechanical Systems (MEMS'00)*, Miyazaki, Japan, pp. 799-804, 2000.

[5] H. Wu, D. Sun, and Z. Zhou, "Micro air vehicles: Configuration, analysis, fabrication, and test," *IEEE/ASME Transactions on Mechatronics*, vol. 9, pp. 108-117, 2004.

[6] P. Dario, M. C. Carrozza, C. Stefanini, and S. D'Attanasio, "A mobile microrobot actuated by a new electromagnetic wobble micromotor," *IEEE/ASME Transactions on Mechatronics*, vol. 3, pp. 9-16, 1998.

[7] S. Matsumoto, O. Oshiro, K. Chihara, A. Iida, K. Kawabe, T. Shimura, M. Asao, and T. Furukawa, "Intravascular ultrasonic imaging with a micromotor," *Japanese Journal of Applied Physics, Part 1 (Regular Papers & Short Notes)*, vol. 34, pp. 2865-2868, 1995.

[8] L. M. Gao, Y. Chen, L. M. Lin, and G. Z. Yan, "Micro motor based new type of endoscope," in *Proc. 20th Annual International Conference of the IEEE Engineering in Medicine and Biology Society*, Hong Kong, China, pp. 1822-1825, 1998.

[9] W. Xinli, C. Shumei, and C. Shukang, "Advantages of electrostatic micromotor and its application to medical instruments," in *Proc. IEEE Industry Applications Conference, 37th IAS Annual Meeting (IAS'02)*, Pittsburgh, PA, USA, pp. 2466-2468, 2002.

[10] C. H. Ahn and M. G. Allen, "Fluid micropumps based on rotary magnetic actuators," in *Proc. IEEE Micro Electro Mechanical Systems (MEMS'95)*, Amsterdam, Netherlands, pp. 408-412, 1995.

[11] S.-T. Lam, "Field emission information storage technology," in *Proc. 14th International Vacuum Microelectronics Conference*, Davis, CA, USA, pp. 135-136, 2001.

[12] M. J. Daneman, N. C. Tien, O. Solgaard, A. P. Pisano, K. Y. Lau, and R. S. Muller, "Linear microvibromotor for positioning optical components," *Journal of Microelectromechanical Systems*, vol. 5, pp. 159-165, 1996.

[13] R. Moser, L. Sache, A. Cassat, H. Bleuler, and T. Higuchi, "Advances in precise positioning using the electrostatic glass motor," in *Proc. IEEE Industry Applications Conference, 38th IAS Annual Meeting (IAS'03)*, Salt Lake City, UT, USA, pp. 1684-1688, 2003.

[14] T. Niino, T. Ban, A. Yamamoto, and T. Higuchi, "X-Y positioner driven by electrostatic motor," in *Proc. IEEE Industry Applications Conference, 31st IAS Annual Meeting (IAS'96)*, San Diego, CA, USA, pp. 1974-1979, 1996.

[15] A. A. Yasseen, J. N. Mitchell, J. F. Klemic, D. A. Smith, and M. Mehregany, "A rotary electrostatic micromotor 1x8 optical switch," *IEEE Journal on Selected Topics in Quantum Electronics*, vol. 5, pp. 26-32, 1999.

[16] A. A. Yasseen, S. W. Smith, F. L. Merat, and M. Mehregany, "Diffraction grating scanners using polysilicon micromotors," *IEEE Journal on Selected Topics in Quantum Electronics*, vol. 5, pp. 75-82, 1999.

[17] L.-S. Fan, Y.-C. Tai, and R. S. Muller, "Integrated movable micromechanical structures for sensors and actuators," *IEEE Transactions on Electron Devices*, vol. 35, pp. 724-730, 1988.

[18] M. Mehregany, K. J. Gabriel, and W. S. N. Trimmer, "Integrated fabrication of polysilicon mechanisms," *IEEE Transactions on Electron Devices*, vol. 35, pp. 719-723, 1988.

[19] L. G. Frechette, S. A. Jacobson, K. S. Breuer, F. E. Ehrich, R. Ghodssi, R. Khanna, C. W. Wong, X. Zhang, M. A. Schmidt, and A. H. Epstein, "Demonstration of a microfabricated high-speed turbine supported on gas bearing," in *Proc. Solid-State Sensor and Actuator Workshop*, Hilton Head Island, SC, pp. 43-47, 2000.

[20] H. H. Woodson and J. R. Melcher, "Chapter 8: Field Description of Magnetic and Electric Forces," in *Electromechanical dynamics, Part II: Fields, Forces, and Motion*, New York, NY, USA: John Wiley and Sons, Inc., 1968.

[21] D. K. Cheng, *Field and Wave Electromagnetics*, 2nd ed., Reading, MA, USA: Addison-Wesley Publishing Co., 1989, p. 280.

[22] A. E. Fitzgerald, C. Kingsley, and S. D. Umans, *Electric Machinery*, 6th ed., Boston, MA, USA: McGraw Hill, 2003, p. 21.

[23] P. L. Chapman and P. T. Krein, "Micromotor technology: electric drive designer's perspective," in *Proc. IEEE Industry Applications Society 36th Annual Meeting (IAS'01)*, Chicago, IL, USA, pp. 1978-1983, 2001.

[24] R. Gomer, *Field Emission and Field Ionization*, New York, NY, USA: American Institute of Physics, 1993, p. 9.

[25] J. D. Cobine, *Gaseous Conductors*, New York, NY, USA: Dover Publication, Inc., 1958, p. 163.

[26] A. Aguero, R. Moyano, and R. Cacace, "Application of rare earth magnets in a micromotor," in *Proc. IEEE International Electric Machines and Drives Conference*, Milwaukee, WI, USA, pp. MB2/7.1-MB2/7.3, 1997.

[27] C. H. Ahn, Y. J. Kim, and M. G. Allen, "A planar variable reluctance magnetic micromotor with fully integrated stator and coils," *Journal of Microelectromechanical Systems*, vol. 2, pp. 165-173, 1993.

[28] P.-A. Gilles, J. Delamare, O. Cugat, and J.-L. Schanen, "Design of a permanent magnet planar synchronous micromotor," in *Proc. IEEE Industry Applications Conference, 35th IAS Annual Meeting and World Conference on Industrial Applications of Electrical Energy*, Rome, Italy, pp. 223-227, 2000.

[29] H. Guckel, T. R. Christenson, K. J. Skrobis, T. S. Jung, J. Klein, K. V. Hartojo, and I. Widjaja, "A first functional current excited planar rotational magnetic micromotor," in *Proc. IEEE Micro Electro Mechanical Systems (MEMS'93)*, Fort Lauderdale, FL, pp. 7-11, 1993.

[30] K. Komori and T. Yamane, "Magnetically levitated micro PM motors by two types of active magnetic bearings," *IEEE/ASME Transactions on Mechatronics*, vol. 6, pp. 43-49, 2001.

[31] L. K. Lagorce and M. G. Allen, "Micromachined polymer magnets," in *Proc. IEEE 9th Annual International Workshop on Micro Electro Mechanical Systems (MEMS'96): An Investigation of Micro Structures, Sensors, Actuators, Machines and Systems*, San Diego, CA, USA, pp. 85-90, 1996.

[32] L. K. Lagorce, O. Brand, and M. G. Allen, "Magnetic microactuators based on polymer magnets," *Journal of Microelectromechanical Systems*, vol. 8, pp. 2-9, 1999.

[33] J.-W. Park, F. Cros, and M. G. Allen, "A sacrificial layer approach to highly laminated magnetic cores," in *Proc. IEEE 15th International Conference on Micro Electro Mechanical Systems (MEMS'02)*, Las Vegas, NV, USA, pp. 380-383, 2002.

[34] B. Wagner, M. Kreutzer, and W. Benecke, "Linear and rotational magnetic micromotors fabricated using silicon technology," in *Proc. IEEE Micro Electro Mechanical Systems (MEMS'92): An Investigation of Micro Structures, Sensors, Actuators, Machines and Robot*, Travemunde, Germany, pp. 183-189, 1992.

[35] W. S. N. Trimmer and K. J. Gabriel, "Design considerations for a practical electrostatic micro-motor," *Sensors and Actuators*, vol. 11, pp. 189-206, 1987.

[36] B. Bollee, "Electrostatic motors," *Philips Technical Review*, vol. 6/7, pp. 178-194, 1969.

[37] O. D. Jefimenko, "Chapter 7: Electrostatic Motors," in *Electrostatics and its Applications*, A. D. Moore, Ed., New York, NY, USA: John Wiley and Sons, 1973.

[38] M. J. Mulcahy and W. R. Bell, "Chapter 8: Electrostatic Generators," in *Electrostatics and its Applications*, A. D. Moore, Ed., New York: John Wiley & Sons, 1973.

[39] J. G. Trump, "Electrostatic sources of electric power," *Electrical Engineering*, vol. 66, pp. 525-534, 1947.

[40] S. F. Bart, *Modeling and Design of Electrostatic Actuators*, Ph.D. Dissertation Thesis, Department of Electrical Engineering and Computer Science, Massachusetts Institute of Technology, Cambridge, MA, USA, 1990.

[41] M. W. Layland, "Generalised electrostatic-machine theory," *Proceedings of the IEE*, vol. 116, pp. 403-405, 1969.

[42] M. Bexell and S. Johansson, "Fabrication and evaluation of a piezoelectric miniature motor," *Sensors and Actuators A (Physical)*, vol. A75, pp. 8-16, 1999.

[43] A. M. Flynn, L. S. Tavrow, S. F. Bart, R. A. Brooks, D. J. Ehrlich, K. R. Udayakumar, and L. E. Cross, "Piezoelectric micromotors for microrobots," *Journal of Microelectromechanical Systems*, vol. 1, pp. 44-51, 1992.

[44] P. Robert, J. S. Danel, and P. Villard, "The electrostatic ultrasonic micromotor," *Journal of Micromechanics and Microengineering*, vol. 7, pp. 170-172, 1997.

[45] B. Makin and B. J. Coles, "Novel electrostatic micromotors," in *Proc. 6th International Conference on Electrical Machines and Drives*, Oxford, UK, pp. 1-3, 1993.

[46] T. Genda, S. Tanaka, and M. Esashi, "High power electrostatic motor and generator using electrets," in *Proc. 12th International Conference on Solid State Sensors, Actuators and Microsystems (Transducers '03)*, Boston, MA, USA, pp. 492-495, 2003.

[47] J. F. Charpentier, Y. Lefevre, E. Sarraute, and B. Trannoy, "Synthesis and modelling of an electrostatic induction motor," *IEEE Transactions on Magnetics*, vol. 31, pp. 1404-1407, 1995.

[48] S. D. Choi and D. A. Dunn, "A surface-charge induction motor," *Proceedings of the IEEE*, vol. 59, pp. 737-748, 1971.

[49] E. R. Mognaschi and J. H. Calderwood, "Asynchronous dielectric induction motor," *Science, Measurement and Technology, IEE Proceedings A*, vol. 137, pp. 331-338, 1990.

[50] C. Livermore, A. Forte, T. Lyszczara, S. D. Umans, and J. H. Lang, "A high-power MEMS electric induction motor," in *Proc. Solid-State Sensor, Actuator and Microsystems Workshop*, Hilton Head Island, SC, USA, pp. 251-254, 2002.

[51] S. F. Nagle, C. Livermore, L. G. Frechette, R. Ghodssi, and J. H. Lang, "An electric induction micromotor," *Journal of Microelectromechanical Systems*, vol. 14, pp. 1127-1143, 2005.

[52] S. F. Bart and J. H. Lang, "Electroquasistatic induction micromotors," in *Proc. IEEE Micro Electro Mechanical Systems: An Investigation of Micro Structures, Sensors, Actuators, Machines and Robots*, Salt Lake City, UT, USA, pp. 7-12, 1989.

[53] E. R. Mognaschi and J. H. Calderwood, "The significance of conductivity and polarization in materials for electrostatic motors," in *Proc. 9th International Symposium on Electrets (ISE 9)*, Shanghai, China, pp. 1050-1054, 1996.

[54] S. F. Bart, T. A. Lober, R. T. Howe, J. H. Lang, and M. F. Schlecht, "Design considerations for micromachined electric actuators," *Sensors and Actuators*, vol. 14, pp. 269-292, 1988.

[55] J. H. Lang and S. F. Bart, "Toward the design of successful electric micromotors," in *Proc. Solid-State Sensor and Actuator Workshop*, Hilton Head Island, SC, USA, pp. 127-130, 1988.

[56] J. H. Lang, M. F. Schlecht, and R. T. Howe, "Electric micromotors: Electromechanical characteristics," in *Proc. IEEE Micro Robots and*

Teleoperators Workshop: An Investigation of Micromechanical Structures, Actuators and Sensors, Hyannis, MA, USA, pp. 13/1-8, 1987.

[57] T. A. Lober and R. T. Howe, "Surface-micromachining processes for electrostatic microactuator fabrication," in *Proc. IEEE Solid-State Sensor and Actuator Workshop*, Hilton Head Island, SC, pp. 59-62, 1988.

[58] M. Megregany, P. Nagarkar, S. D. Senturia, and J. H. Lang, "Operation of microfabricated harmonic and ordinary side-drive motors," in *Proc. IEEE Micro Electro Mechanical Systems: An Investigation of Micro Structures, Sensors, Actuators, Machines and Robots*, Napa Valley, CA, pp. 1-8, 1990.

[59] L.-S. Fan, Y.-C. Tai, and R. S. Muller, "IC-processed electrostatic micro-motors," in *Proc. the IEEE International Electronic Devices Meeting (IEDM'88)*, San Francisco, CA, USA, pp. 666-669, 1988.

[60] M. Mehregany, S. F. Bart, L. S. Tavrow, J. H. Lang, S. D. Senturia, and M. F. Schlecht, "A study of three microfabricated variable-capacitance motors," in *Proc. the 5th International Conference on Solid-State Sensors and Actuators (Transducers'89) and Eurosensor III*, Montreux, Switzerland, pp. 173-179, 1990.

[61] S. F. Bart, *Modeling and Design of Electrostatic Actuators*, Ph.D. Dissertation Thesis, Department of Electrical Engineering and Computer Science, Massachusetts Institute of Technology, Cambridge, MA, 1990.

[62] M. Mehregany, *Microfabricated silicon electric mechanisms*, Ph.D. Dissertation Thesis, Department of Electrical Engineering and Computer Science, Massachusetts Institute of Technology, Cambridge, MA, 1990.

[63] M. Mehregany, S. F. Bart, L. S. Tavrow, J. H. Lang, and S. D. Senturia, "Principles in design and microfabrication of variable-capacitance side-drive motors," *Journal of Vacuum Science and Technology A*, vol. 8, pp. 3614-3624, 1990.

[64] S. F. Bart, M. Mehregany, L. S. Tavrow, J. H. Lang, and S. D. Senturia, "Electric micromotor dynamics," *IEEE Transactions on Electron Devices*, vol. 39, pp. 566-575, 1992.

[65] L.-S. Fan, Y.-C. Tai, and R. S. Muller, "IC-processed electrostatic micro-motors," in *Proc. IEEE International Electronic Devices Meeting (IEDM'88)*, San Francisco, CA, USA, pp. 666-669, 1988.

[66] R. S. Muller, "Microdynamics," *Sensors and Actuators*, vol. A21-A23, pp. 1-8, 1990.

[67] Y.-C. Tai, L.-S. Fan, and R. S. Muller, "IC-processed micro-motors: Design, technology, and testing," in *Proc. IEEE Micro Electro Mechanical Systems:*

An Investigation of Micro Structures, Sensors, Actuators, Machines and Robots, Salt Lake City, UT, pp. 1-6, 1989.

[68] K.-S. Chen, J.-Y. Chen, and S.-Y. Lin, "Fracture analysis of thick plasma-enhanced chemical vapor deposited oxide films for improving the structural integrity of power MEMS," *Journal of Micromechanics and Microengineering*, vol. 12, pp. 714-722, 2002.

[69] R. Ghodssi, L. G. Frechette, S. F. Nagle, X. Zhang, A. A. Ayon, S. D. Senturia, and M. A. Schmidt, "Thick buried oxide in silicon (TBOS): An integrated fabrication technology for multi-stack wafer-bonded MEMS processes," in *Proc. 10th International Conference on Solid-State Sensors and Actuators (Tansducers'99)*, Sendai, Japan, pp. 1456-1459, 1999.

[70] X. Zhang, K.-S. Chen, R. Ghodssi, A. A. Ayon, and S. M. Spearing, "Residual stress and fracture in thick tetraethylorthosilicate (TEOS) and silane-based PECVD oxide films," *Sensors and Actuators A*, vol. 91, pp. 373-380, 2001.

[71] X. Zhang, K.-S. Chen, and S. M. Spearing, "Thermo-mechanical behavior of thick PECVD oxide films for power MEMS applications," *Sensors and Actuators A*, vol. 103, pp. 263-270, 2003.

[72] X. Zhang, R. Ghodssi, K.-S. Chen, A. A. Ayon, and S. M. Spearing, "Residual stress characterization of thick PECVD TEOS film for power MEMS applications," in *Proc. Solid-State Sensor and Actuator Workshop*, Hilton Head Island, SC, pp. 316-319, 2000.

[73] S. F. Nagle and J. H. Lang, "A micro-scale electric-induction machine for a micro gas turbine generator," in *Proc. 27th Annual Meeting of the Electrostatic Society of America*, Boston, MA, pp., 1999.

[74] M. F. Farona, "Benzocyclobutenes in polymer chemistry," *Progress in Polymer Science*, vol. 21, pp. 505-555, 1996.

[75] R. A. Kirchhoff and K. J. Bruza, "Benzocyclobutenes in polymer synthesis," *Progress in Polymer Science*, vol. 18, pp. 85-185, 1993.

[76] H. Hendricks, "Low dielectric constant materials for IC intermetal dielectric applications: A status report on the leading candidates," in *Proc. Materials Research Society Symposium: Low-Dielectric Constant Materials II*, Boston, MA, USA, pp. 3-14, 1997.

[77] M. E. Mills, P. Townsend, D. Castillo, S. Martin, and A. Achen, "Benzocyclobutene (DVS-BCB) polymer as an interlayer dielectric (ILD) material," *Microelectronic Engineering*, vol. 33, pp. 327-334, 1997.

[78] M. J. Berry, T. G. Tessier, I. Turlik, G. M. Adema, D. C. Burdeaux, J. N. Carr, and P. Garrou, "Benzocyclobutene as a dielectric for multichip module

fabrication," in *Proc. 40th Electronic Components and Technology Conference*, Las Vegas, NV, USA, pp. 746-750, 1990.

[79] D. C. Burdeaux, P. H. Townsend, J. N. Carr, and P. Garrou, "Benzocyclobutene (BCB) dielectrics for the fabrication of high density, thin film multichip modules," *Journal of Electronic Materials*, vol. 19, pp. 1357-1366, 1990.

[80] R. W. Johnson, T. L. Phillips, W. K. Weidner, S. F. Hahn, D. C. Burdeaux, and P. H. Townsend, "Benzocyclobutene interlayer dielectrics for thin film multichip modules," *IEEE Transactions on Components, Hybrid, and Manufacturing Technology*, vol. 13, pp. 347-352, 1990.

[81] A. J. G. Strandjord, R. H. Heistand, P. Garrou, and T. G. Tessier, "A photosensitive-BCB on laminate technology (MCM-LD)," in *Proc. 44th Electronic Components and Technology Conference*, Washington, DC, USA, pp. 374-386, 1994.

[82] D. T. Price, R. J. Gutmann, and S. P. Murarka, "Damascene copper interconnects with polymer ILDs," *Thin Solid Films*, vol. 308-309, pp. 523-528, 1997.

[83] Y. Ida, P. E. Garrou, A. J. G. Strandjord, S. L. Cummings, W. B. Rogers, M. J. Berry, and S. R. Kisting, "Processing, transfer solder bumping, chip attachment and testing of a thin film Cu/photo-BCB MCM-D," in *Proc. 8th IEEE/CPMT International Electronic Manufacturing Technology (IEMT) Symposium*, Omiya, Japan, pp. 441-444, 1995.

[84] L. A. Keser, R. Bajaj, and T. Fang, "Redistribution and bumping of a high I/O device for flip chip assembly," *IEEE Transactions on Advanced Packaging*, vol. 23, pp. 3-8, 2000.

[85] C. F. Kane and R. R. Krchnavek, "Benzocyclobutene optical waveguides," *IEEE Photonics Technology Letters*, vol. 7, pp. 535-537, 1995.

[86] S. Wolff, A. R. Giehl, M. Renno, and H. Fouckhardt, "Metallic waveguide mirrors in polymer film waveguides," *Applied Physics B: Laser and Optics*, vol. 73, pp. 623-627, 2001.

[87] S. Wolff, A. Grosse, H.-J. Schimper, A. R. Giehl, M. Kuhnke, and R. Grote, "Technology and realization of metallic curved waveguide mirrors in polymer film waveguides based on anisotropic plasma etching," *Journal of Vacuum Science and Technology A*, vol. 19, pp. 87-89, 2001.

[88] X. Huo, K. J. Chen, and P. C. H. Chan, "Silicon-based high-Q inductors incorporating electroplated copper and low-k BCB dielectric," *IEEE Electron Device Letters*, vol. 23, pp. 520-522, 2002.

[89] A. Okubora, T. Ogawa, T. Hirabayashi, T. Kosemura, T. Ogino, H. Nakayama, Y. Oya, Y. Nishitani, and Y. Asami, "A novel integrated passive substrate fabricated directly on an organic laminate for RF applications," in *Proc. 52nd Electronic Components and Technology Conference*, San Diego, CA, pp. 672-675, 2002.

[90] A. J. G. Strandjord, W. B. Rogers, Y. Ida, R. R. De Vellis, S. Shiau, E. S. Moyer, D. M. Scheck, and P. E. Garrou, "Photosensitive benzocyclobutene for stress-buffer and passivation applications (one mask manufacturing process)," in *Proc. 47th Electronic Components and Technology Conference*, San Jose, CA, pp. 1260-1268, 1997.

[91] C. Laville and C. Pellet, "Interdigitated humidity sensors for a portable clinical microsystem," *Biomedical Engineering, IEEE Transactions on*, vol. 49, pp. 1162-1167, 2002.

[92] T.-K. A. Chou and K. Najafi, "3D MEMS fabrication using low-temperature wafer bonding with benzocyclobutene (BCB)," in *Proc. 11th International Conference on Solid-State Sensors and Actuators (Transducers'01)*, Munich, Germany, pp. 1570-1573, 2001.

[93] T.-K. A. Chou, K. Najafi, M. O. Muller, L. P. Bernal, and P. D. Washabaugh, "High-density micromachined acoustic ejector array for micro propulsion," in *Proc. 11th International Conference on Solid-State Sensors and Actuators (Transducers'01)*, Munich, Germany, pp. 890-893, 2001.

[94] F. Niklaus, P. Enoksson, E. Kalvesten, and G. Stemme, "Void-free full wafer adhesive bonding," in *Proc. IEEE 13th International Conference on Micro Electro Mechanical Systems*, Miyazaki, Japan, pp. 247-252, 2000.

[95] F. Niklaus, P. Enoksson, E. Kalvesten, and G. Stemme, "Low-temperature full wafer adhesive bonding," *Journal of Micromechanics and Microengineering*, vol. 11, pp. 100-1-7, 2001.

[96] S. Guo, "Cyclotene(R) diaphragm for MEMS-based IR detectors," in *Proc. SPIE Micromachining and Microfabrication Process Technology VII Conference*, San Jose, CA, pp. 422-429, 2003.

[97] S.-H. Lee and B. C. Kim, "Curled micro-cantilevers using benzocyclobutene polymer and Mo for wafer level probing," *Sensors and Actuators A*, vol. 121, pp. 472-479, 2005.

[98] U. Beerschwinger, R. L. Reuben, and S. J. Yang, "Frictional study of micromotor bearings," *Sensors and Actuators A (Physical)*, vol. A63, pp. 229-241, 1997.

[99] M. Mehregany, S. D. Senturia, and J. H. Lang, "Friction and wear in microfabricated harmonic side-drive motors," in *Proc. Solid-State Sensor and Actuator Workshop*, Hilton Head Island, SC, pp. 17-22, 1990.

[100] S. C. Jacobsen, R. H. Price, J. E. Wood, T. H. Rytting, and M. Rafaelof, "The wobble motor: an electrostatic, planetary-armature, microactuator," in *Proc. IEEE Micro Electro Mechanical Systems: An Investigation of Micro Structures, Sensors, Actuators, Machines and Robots*, Salt Lake City, UT, pp. 17-24, 1989.

[101] H. Fujita, A. Omokada, M. Sakata, and Y. Hatazawa, "Variable gap electrostatic actuators," in *Proc. 8th Sensor Symposium*, Tokyo, Japan, pp. 145-148, 1989.

[102] R. Ghodssi, D. D. Denton, A. A. Seireg, and B. Howland, "Rolling friction in a linear microactuator," *Journal of Vacuum Science and Technology A*, vol. 11, pp. 803-807, 1993.

[103] T. W. Lin, A. Modafe, B. Shapiro, and R. Ghodssi, "Characterization of dynamic friction in MEMS-based microball bearings," *IEEE Transactions on Instrumentation and Measurement*, vol. 53, pp. 839-846, 2004.

[104] A. D. Feinerman and S. R. Thodati, "Millimeter-scale actuator with fiber-optic roller bearings," *Journal of Microelectromechanical Systems*, vol. 4, pp. 28-33, 1995.

[105] S. Kumar, D. Cho, and W. Carr, "A proposal for electrically levitating micromotors," *Sensors and Actuators A (Physical)*, vol. 24, pp. 141-149, 1990.

[106] L. G. Frechette, S. F. Nagle, R. Ghodssi, S. D. Umans, M. A. Schmidt, and J. H. Lang, "An electrostatic induction micromotor supported on gas-lubricated bearings," in *Proc. IEEE 14th International Conference on Micro Electro Mechanical Systems (MEMS'01)*, Interlaken, Switzerland, pp. 290-293, 2001.

[107] H. H. Woodson and J. R. Melcher, "Chapter 4: Rotating Machines," in *Electromechanical dynamics, Part II: Fields, Forces, and Motion*, New York, NY, USA: John Wiley and Sons, Inc., 1968, pp. 148.

[108] S. Meninger, J. O. Mur-Miranda, R. Amirtharajah, A. P. Chandrakasan, and J. H. Lang, "Vibration-to-electric energy conversion," *IEEE Transactions on Very Large Scale Integration (VLSI) Sysems*, vol. 9, pp. 64-76, 2001.

[109] X. Tan, A. Modafe, and R. Ghodssi, "Measurement and modeling of dynamic rolling friction in linear microball bearings," *Journal of Dynamic Systems, Measurement, and Control*, vol. 128, pp. 891-898, 2006.

[110] M. Mehregany, S. F. Bart, L. S. Tavrow, J. H. Lang, S. D. Senturia, and M. F. Schlecht, "A study of three microfabricated variable-capacitance motors," in *Proc. 5th International Conference on Solid-State Sensors and Actuators (Transducers'89)*, Montreux, Switzerland, pp. 173-179, 1990.

[111] F. Niklaus, P. Enoksson, P. Griss, E. Kalvesten, and G. Stemme, "Low-temperature wafer-level transfer bonding," *Journal of Microelectromechanical Systems*, vol. 10, pp. 525-531, 2001.

[112] S. Sivoththaman, R. Jeyakumar, L. Ren, and A. Nathan, "Characterization of low permittivity (low-k) polymeric dielectric films for low temperature device integration," *Journal of Vacuum Science and Technology A*, vol. 20, pp. 1149-1153, 2002.

[113] H. Pranjoto and D. D. Denton, "Moisture uptake of bisbenzocyclobutene (BCB) films for electronic packaging applications," in *Proc. MRS Fall Meeting: Electronic Packaging Materials Science V, v. 203*, Boston, MA, pp. 295-302, 1990.

[114] A. Modafe, N. Ghalichechian, B. Kleber, and R. Ghodssi, "Electrical characterization of benzocyclobutene polymers for electric micromachines," *IEEE Transactions on Device and Material Reliability*, vol. 4, pp. 495-508, 2004.

[115] Agilent Technologies, *4279A 1 MHz C-V Meter Operation Manual*, 3rd ed.: Agilent Technologies, 2000.

[116] Agilent Technologies, *Agilent Technologies Impedance Measurement Handbook*, 2nd ed.: Agilent Technologies, 2001.

[117] L. A. Dissado and P. J. J. Sweeney, "Physical model for breakdown structures in solid dielectrics," *Physical Review B*, vol. 48, pp. 16261-16268, 1993.

[118] S. Whitebead, *Dielectric Phenomena: III. Breakdown of Solid Dielectrics*, New York, NY, USA, 1932.

[119] J. M. Steigerwald, S. P. Muraka, and R. J. Gutmann, *Chemical Mechanical Planarization of Microelectronic Materials*, New York, NY, USA: John Wiley & Sons, 1997.

[120] C. L. Borst, W. N. Gill, and R. J. Gutmann, *Chemical-Mechanical Polishing of Low Dielectric Constant Polymers and Organosilicate Glasses*, Boston, MA, USA: Kluwer Academic Publishers, 2002, p. 48.

[121] J. M. Steigerwald, S. P. Muraka, and R. J. Gutmann, *Chemical Mechanical Planarization of Microelectronic Materials*, New York, NY, USA: John Wiley & Sons, 1997, p. 49.

[122] N. J. Brown, P. C. Baker, and R. T. Maney, "Optical polishing of metals," in *Proc. Proc. SPIE: Contemporary Methods of Optical Fabrication*, pp. 42-57, 1981.

[123] F. G. Shi and B. Zhao, "Modeling of chemical-mechanical polishing with soft pads," *Applied Physics A*, vol. 67, pp. 249-252, 1998.

[124] T. K. Doy, K. Seshimo, K. Suzuki, A. Philipossian, and M. Kinoshita, "Impact of Novel Pad Groove Designs on Removal Rate and Uniformity of Dielectric and Copper CMP," *Journal of The Electrochemical Society*, vol. 151, pp. G196-G199, 2004.

[125] Y.-R. Jeng and P.-Y. Huang, "Impact of Abrasive Particles on the Material Removal Rate in CMP," *Electrochemical and Solid-State Letters*, vol. 7, pp. G40-G43, 2004.

[126] Q. Luo, S. Ramarajan, and S. V. Babu, "Modification of the Preston equation for the chemical-mechanical polishing of copper," *Thin Solid Films*, vol. 335, pp. 160-167, 1998.

[127] E. Paul, "A Model of Chemical Mechanical Polishing," *Journal of the Electrochemical Society*, vol. 148, pp. G355-G358, 2001.

[128] E. Paul, "A Model of Chemical Mechanical Polishing," *Journal of the Electrochemical Society*, vol. 149, pp. G305-G308, 2002.

[129] E. Paul and R. Vacassy, "A Model of CMP," *Journal of the Electrochemical Society*, vol. 150, pp. G739-G743, 2003.

[130] S. Thagella, A. K. Sikder, and A. Kumar, "Tribological Issues and Modeling of Removal Rate of Low-k Films in CMP," *Journal of the Electrochemical Society*, vol. 151, pp. G205-G215, 2004.

[131] J. M. Neirynck, G.-R. Yang, S. P. Murarka, and R. J. Gutmann, "The addition of surfactant to slurry for polymer CMP: effects on polymer surface, removal rate and underlying Cu," in *Proc. 23rd International Conference on Metallurgical Coatings and Thin Films: Thin Solid Films*, San Diego, CA, USA, pp. 447-452, 1996.

[132] N. Ghalichechian, A. Modafe, R. Ghodssi, P. Lazzeri, V. Micheli, and M. Anderle, "Integration of benzocyclobutene polymers and silicon micromachined structures using wet anisotropic etching," *Journal of Vacuum Science and Technology B*, vol. 22, pp. 2439-2447, 2004.

[133] A. Modafe, N. Ghalichechian, and R. Ghodssi, "Multilevel interconnection and isolation for electrostatic MEMS using embedded benzocyclobutene in silicon process (Invited paper)," in *Proc. 22nd International VLSI/ULSI*

Multilevel Interconnection Conference (2005 VMIC), Fremont, CA, USA, pp. 309-316, 2005.

[134] A. Modafe, N. Ghalichechian, M. Powers, M. Khbeis, and R. Ghodssi, "Embedded benzocyclobutene in silicon: An integrated fabrication process for electrical and thermal isolation in MEMS," *Microelectronic Engineering*, vol. 82, pp. 154-167, 2005.

[135] G. T. A. Kovacs, N. I. Maluf, and K. E. Petersen, "Bulk micromachining of silicon," *Proceedings of the IEEE*, vol. 86, pp. 1536-1551, 1998.

[136] C. M. Waits, A. Modafe, and R. Ghodssi, "Investigation of gray-scale technology for large area 3-D silicon MEMS structures," *Journal of Micromechanics and Microengineering*, vol. 13, pp. 170-177, 2003.

[137] C. M. Waits, B. Morgan, M. J. Kastantin, and R. Ghodssi, "Microfabrication of 3D Silicon MEMS Structures using Gray-scale Lithography and Deep Reactive Ion Etching," *Sensors and Actuators A (Physical)*, vol. 119, pp. 245-253, 2005.

[138] B. Morgan, C. M. Waits, J. Krizmanic, and R. Ghodssi, "Development of a Deep Silicon Phase Fresnel Lens Using Gray-Scale Lithography and Deep Reactive Ion Etching," *Journal of Microelectromechanical Systems*, vol. 13, pp. 113-120, 2004.